UNIVERSITY OF LIVERPOOL

Particles dynamics at the nanoscale

Thesis submitted in accordance with the requirements of the University of Liverpool for the degree of Doctor of Philosophy

By

Francesco Giorgi

October 2021

ABSTRACT

Nanoparticles are one of the most promising materials supporting the current technological revolution, particularly for medical and pharmaceutical applications. However, a clear characterisation of the dynamics of particles at the nanoscopic scale has becoming crucial to fully support the development and translation to real-life scenarios of such applications and to understand their potential as well as limitations. In this thesis, the dynamics of a range of particles and biological organisms at the micro-nano scale was observed in a conventional inverted optical microscope in real-time without any requirement for fluorescent labeling, using an imaging technique based on the optical phenomenon of caustics. Gold nanoparticles were monitored to quantify the influence of inter-particle forces on their diffusion behaviour in solutions with different ionic content. Most of the cell culture media contain a high concentration of salts in solution, and this ionic content can potentially influence the diffusion dynamics of nanoparticles and critical parameters like cellular uptake and toxicity. The results demonstrated the dependence of the diffusion coefficient on the ionic content of the solution and demonstrated that electrostatic forces, Van der Waals forces and the nanoparticle-ion interactions should be accounted for when considering the diffusion dynamics of nanoparticles in solution with a non-negligible ionic content. Experimental observations on gold nanoparticles were also carried out to characterise the three-dimensional settling dynamics in simple and biological solutions, to provide quantitative information on the concentration of nanoparticles delivered at the surface level during in-vitro experiments. Typically, investigations involving cells and nanoparticles are conducted in-vitro using a 2D adherent monolayers of cultured cells. Hence, a clear understanding of the nanoparticles delivered to the cellular and surface level is needed to develop accurate dose-response assessments. The sedimentation times and the concentration profiles obtained demonstrated the inaccuracy of the current standard theoretical models for predicting the settling dynamics of particles at low

concentration and confirmed the dependence of the diffusion coefficient on the local concentration of nanoparticles in solution, already suggested in a number of previous studies. Moreover, the optical setup used in this study has been proven to be able to monitor and quantify the 3D motion and transport of nanoparticles in solution, providing a potential tool to characterise nanoparticles approach to cell and the preliminary interactions.

The experimental evidence about the dependence of the dynamics of nanoparticles on the local concentration in solution was extended to investigate the accuracy of sizing techniques based on the evaluation of their diffusion behaviour. The analysis conducted on the asymmetric flow field-flow fractionation coupled with online dynamic light scattering technique showed a reduced accuracy of the sizing ability of the system when injected with solutions at low concentration of particles, providing a further confirmation and a direct implication of the experimental observation about the relation between dynamics and concentration of particles in solution.

The tracking potential of the caustics optical technique was further explored in the final stage of this research project by imaging human and bacteria cells. The combination of the optical technique based on caustics with digital image correlation allowed for the characterisation of the dynamics of intracellular organelles, paving the way for further future real-time non-invasive investigations of cellular activity. Concerning bacterial cells, the enhanced resolving power of the optical set-up based on caustics allowed for the monitoring and characterization of the dynamics of *Escherichia coli* bacteria and their interaction with surfaces, providing evidence for the relationship between bacterial dynamics and viability, as well as the ability to start a biofilm. This difference in dynamics allowed the early detection of a potential biofilm formation and offers the possibility to quantify the efficiency of antimicrobial surfaces and coatings.

ACKNOWLEDGEMENTS

I would like to apologise to the reader for the personal nature of this section, however, I believe that the acknowledgements should be made by the person who exists behind the professional persona. As I write these words I am currently flying away from Liverpool, and it is the beginning of the next chapter of my professional as well as personal life. I guess this is the most appropriate moment to write this section.

I would like to start by thanking my supervisory board, without them nothing would have been achieved in terms of this thesis. They have helped keep me on track, and without them I would be a less competent researcher. First, I want to acknowledge Prof. Eann Patterson; not only for having been a knowledgeable and present supervisor, but also for being a mentor, and a role model to follow. I really wish and aspire to be as professional as he is. He has been my North Star since day 1, since the first email exchange.

Secondly, I would like to acknowledge my secondary supervisor, Dr. Jude Curran. She has probably contributed more than anyone else, to my professional and personal development in the last few years of my life. I definitely made one of the best choices of my life when I chose her project for my Master's. I have learned a lot from her, and I strongly believe that there needs to be more people like her in academia. She has perfected the balance between professionalism, expertise and empathy in her role.

To conclude the supervisory board, my great appreciation goes to Dr. Maurice Whelan. After working with him, I really understand why he is so successful in his field. Despite being the head of one of the most important departments in the EU commission, he has always been keen to exchange ideas and was always open to discussion, even with a "simple" PhD student. Another good example of "how the research environment should be".

Now to my fellow colleagues/acquaintances, now friends, that have shared a piece of life with me. There is not enough space to name you all, but I am sure you guys will be able to notice I am talking about you if reading these lines. I have been so lucky to meet you. You helped me navigate through this hard journey and to achieve all the results described in this thesis. I shared a consistent piece of life with you, and all the memories and feelings will always be with me. Forever. Every time one of you left, I was heartbroken, and now that I am leaving, I am breathless. If I could, I would like to have you all in my everyday life moving forward.

I would also like to acknowledge the units F3 and F2 of the JRC. Being surrounded by such great researchers and professionals has been truly inspiring. They welcomed me like a colleague, and since the very first day, they created the right environment for my personal improvement. EU policymakers are in safe hands if they rely on these wonderful researchers. I also want to thank the trainee community who were there during my stay. It is unbelievable how deep of an imprint they left in my mind, despite only having the chance to spend a few months together

A special mention to my partner, C. The impact she has always had in my life is indescribable, and something she may not be aware of. I think she might not realize that when she looks at me, she is actually looking at a part of herself as well. She has shown me the strongest emotions a person can experience in the entire life. Not merely "love". I wish and hope I will be able to make her happy, always.

Then there is my family. They are the people who have always supported me, believed in me, motivated me to do my best, trusted in me and guided me. Mamma, Papà, Lella, vi voglio bene.

A great mention to the city of Liverpool and the University of Liverpool, for this amazing opportunity in life and for having always being my safe port, to which I could navigate when my life was a storm. I have been welcomed not as a foreigner, but as a peer. There used to be

a billboard in the city center, outside the central station, that states "a place that you will call home and you will never want to leave".

Well, I have to say, no marketing campaign has been more honest.

Last but not least I would like to acknowledge myself. For the perseverance, the intuition, the creativity and the attitude. For being able to accept failures in order to achieve "success".

OUTPUT OF THE THESIS

Type	Title	Status	doi
Journal publication	The influence of inter-particle forces on diffusion at the nanoscale	Published	10.1038/s41598-019-48754-5
Journal publication	Limitations of Nanoparticles Size Characterization by Asymmetric-flow field-flow fractionation with Online Dynamic Light Scattering	Published	10.1007/s10337-020-03997-7
Journal publication	Settling dynamics of nanoparticles in simple and biological media	Published	10.1098/rsos.210068
Journal publication	Real-time monitoring of dynamics and interactions of bacteria and the early-stage formation of biofilms	In progress	/
Journal publication	The influence of fluorescent dyes on the growth rate and division process in *Escherichia coli*	In progress	/

ABBREVIATIONS

hMSCs: human mesenchymal stem cells

AF4: asymmetric flow field-flow fractionation

DLS: dynamic light scattering

NTA: nanosight

MSD: mean Square Displacement

BSA: bovine serum albumin

NaCl: sodium chloride

DMEM: dulbecco's modified eagle medium

UV-Vis: Ultraviolet-visible spectroscopy

CLS: Centrifugal Liquid Sedimentation

LB: Luria-Bertani broth

PBS: Phosphate buffered saline

BKC: Benzalkonium chloride

FBS: Fetal bovine serum

DIC: Digital image correlation

EPS: Extracellular polymeric substances

TABLE OF CONTENTS

CHAPTER 1

1. Introduction

Among other materials at the nanoscale, nanoparticles have attracted a growing attention in the scientific community due to their unique properties and versatility. The ability to manufacture functionalised nanoparticles with a well-defined geometry and controlled optical properties paved the way for a number of potential applications, supported by an even greater number of scientific studies. For instance, considering only the medical and pharmaceutical field, nanoparticles have been identified as a potential revolutionary material in a range of applications such as biosensing, photocatalysis, drug delivery, photothermal therapy and imaging [1]. The widespread usage of nanoparticles and their presence in a significant number of healthcare related products, required a rigorous definition to be provided for environmental, health and safety regulations. The European Commission officially defined as a nanoparticle any material with one or more external dimensions in the size range of 1 nm – 100 nm [2]. However, the physical properties of a nanoparticles (such as size and shape) are not the only factors to consider to fully characterise their behaviour and any potential effect on the external organism they interact with. Once in solution, the dynamics of nanoparticles is a function of intrinsic (properties of the nanoparticles) as well as extrinsic properties (properties of the solution). Such dynamics has been reported to have a non-negligible impact on the interaction with the surrounding organisms, with direct implications on cellular uptake, excretion, toxicity, etc. For instance, by exposing cells to suspensions of nanoparticles, Cho et al. demonstrated that cellular uptake of gold nanoparticles depends on the sedimentation and diffusion velocities of the nanoparticles and does not depend on their size, shape and density [3]. The dynamics of nanoparticles directly affects also the concentration of particles delivered at the cellular level. Knowing the exact concentration of nanoparticles local to the cell is essential to develop an

accurate dose-response analysis [4]. Moreover, it is worth considering that a number of techniques used to characterise nanoparticles based on evaluating their dynamics (e.g. NanoSight), have been reported to fail to provide an accurate size distribution of the nanoparticles in solution under certain circumstances. The sizing failure can be directly related to the unexpected diffusion dynamics exhibited by the nanoparticles in solution [5, 6].

Despite the empirical evidence and potential implications, the dynamics of nanoparticles is still mainly described by theoretical models that are not directly transferrable to more complex scenarios and has been poorly investigated experimentally with real-time, direct observations.

The experimental research proposed in this thesis is concerned with the direct observation and empirical characterisation of the motion and transport of a range of particles in a variety of solutions, providing an analysis of the factors affecting their dynamics and the implications of such dynamics on nanoparticles applications. The observations have been conducted exploiting the optical phenomenon of caustics, monitoring the dynamics of nanoparticles in real-time without any requirement for fluorescent labelling. The successful application of the caustics optical technique to visualise protein nanoparticles has extended this research to investigate the possibility of monitoring the internal dynamics of cellular components, namely intracellular organelles. The monitoring over time of the intracellular organelles of human mesenchymal stem cells (hMSCs) allowed us to relate intracellular dynamics with cellular viability, making the analysis of intracellular dynamics a promising early signal as detector of cellular functioning and paving the way for a number of future toxicological and pharmaceutical investigations. The enhanced resolving power of the optical set-up based on caustics allowed also for the monitoring of bacterial cells dynamics and their interactions with surface to evaluate and characterise the effectiveness of anti-microbial coatings, in an effort to support the fight against the so-called antibiotic-resistant bacteria (also known as ‘superbugs’).

Chapter 2 presents the theoretical foundation of the dynamics of particles at the nanoscale. The state of the art of the two main processes regulating the motion and transport of nanoparticles, the diffusion and sedimentation processes, is discussed along with the mathematical laws developed by Einstein and Stokes to describe dynamics at the micrometre scale. The diffusion process (also known as Brownian motion) was first observed and characterised by Robert Brown in 1827 and then formalised mathematically by Einstein in 1905, adapting the previous work of Stokes. The latter played an important role on the history of the investigation of particle dynamics, providing also the first mathematical description of the sedimentation process with the Stokes's velocity law, the mathematical formulation for the terminal sedimentation velocity of small spherical particles in a fluid medium. The diffusion and sedimentation processes regulate the motion and transport of particles in the solution until the sedimentation and diffusion forces come into a dynamic equilibrium. The sedimentation – diffusion equilibrium was mathematically described by Mason and Weaver in 1924, and that model is still applied when predicting the concentration profile of particles in solution. All of the theoretical models presented have been developed for particles at the micrometre scale, but they are usually directly translated to characterise the dynamics of nanoparticles, without considering the non-negligible presence of other dominant forces at the nanoscale (e.g. electrostatic and Van der Waals forces).

Chapter 2 also presents the state of the art about the current understanding of interactions between bacteria and surfaces. It is well-known that once a bacterium approaches a surface it can potentially form a biofilm combining with other surrounding bacteria. However, the preliminary interaction between a bacterium and a surface and the early stage of the biofilm formation lack a detailed and empirical characterisation. This chapter also presents a brief introduction to the potential relationship between intracellular organelles dynamics and

interactions and cell physiology, identifying the need for a real-time, non-invasive imaging technique able to detect and quantify the changes of the dynamics.

Chapter 3 is the materials and methods section. A detailed overview of all the relevant materials and experimental/mathematical methods used in this research is presented. Particular care is taken to describe the optical tracking technique used to detect label-free particles and cells in real-time. The technique is based on generating caustic signatures of the particles in solution. The optical signature generated is orders of magnitude bigger than the real particle under test, allowing its detection in a common optical inverted microscope.

The results and the related discussion are presented in Chapter 4. The choice of merging the two sections is related to the progressive nature of this experimental research and reflects the research path followed during the years of investigation. The empirical and theoretical findings of each experimental research carried out laid the foundation for the subsequent one, paving the way for a new investigation. First, the ability of the optical technique for visualising either metallic or organic nanoparticles was assessed, to understand the potential as well as the limitation of the optical set-up based on caustics. Subsequently, the dynamics of gold nanoparticles dispersed in solutions with different ionic contents was characterised to evaluate the influence of inter-particles forces on two-dimensional diffusion dynamics. The results obtained demonstrated the role of Van der Waals and electrostatic forces in regulating the dynamics of nanoparticles as well as confirming the failure of the classical Stokes-Einstein equation to predict the two-dimensional diffusion dynamics of nanoparticles below a critical size and concentration, suggesting the dependence of the diffusion process on the concentration of particles in solution. The analysis was then translated to the three-dimensional domain, characterising the sedimentation-diffusion equilibrium of nanoparticles in simple and biological media to investigate the factors affecting the settling dynamics of nanoparticles and the predictive ability of the theoretical Mason – Weaver model. The empirical observations

recognised size, colloidal stability and solution temperature as the main factors affecting the settling dynamics and the failure of the classical Mason – Weaver model in describing the concentration profile of nanoparticles over time. On the other hand, the modified version of the classical Mason – Weaver model, developed following speculation about the relation between the concentration of nanoparticles and their dynamics, has been proven to be more accurate in predicting the settling dynamics of nanoparticles. The next section of this chapter presents one of the practical implications of these findings, showing the limitation of the combined asymmetric flow field-flow fractionation (AF4) and dynamic light scattering (DLS) on sizing solutions with low concentrations of particles. The subsequent two sections of this chapter describe the characterisation of the dynamics of biological organisms at the micro/nano scale. The efficiency of antimicrobial surfaces has been evaluated by observing the interaction of *Escherichia coli* bacteria with untreated glass control surfaces and surfaces treated with benzalkonium chloride. The analysis of the dynamics of the bacteria and the interaction with the surfaces allowed the early label-free assessment of bacteria viability as well as the ability to start a biofilm. In addition, the monitoring of the motion of intracellular organelles in human mesenchymal stem cells in real – time allowed basic cell functioning to be resolved, paving the way for a range of future applications. Chapter 4 is concluded with a general discussion section followed by a future work section. These two sections are aimed to provide an overall discussion of the experimental results obtained, highlighting the connections between separate investigations along with the current and future implications.

The main findings and conclusions of the thesis are summarized in Chapter 5.

1.1. Aim and objectives

Aim:

Investigate the dynamics of a range of particles and organisms at the micro and nano scale in real-time exploiting the optical phenomenon of caustics.

Objectives:

- Determine the capability of the optical set-up based on caustics to generate detectable caustic signatures from particles (metallic/organic) and organisms (bacteria/intracellular organelles).
- Quantify the influence of interparticle forces on the diffusion dynamics of nanoparticles by dispersing gold nanoparticles in solutions with a different ionic content.
- Characterise the settling dynamics of gold nanoparticles in deionised water and cell culture media at different temperature.
- Investigate the relationship between the dynamics exhibited by bacteria when interacting with a surface and their ability to start a biofilm by characterising the mechanism of attachment of *Escherichia coli* bacteria to control and antimicrobial surfaces.
- Investigate the potential of the optical set-up based on caustics coupled with digital image correlation to characterise the dynamics internal to the cytoplasm.

CHAPTER 2

2. Theoretical background

2.1. The dynamics of inorganic nanoparticles in solution

2.1.1. The diffusion and sedimentation processes

Nanoparticles dispersed in solution tend to diffuse, sediment, and aggregate as a function of intrinsic properties (size, mass, surface charge, etc.) and as a function of systemic properties (viscosity, temperature, etc.). The diffusion process is caused by the continuous collision between particles and the molecules of the medium, resulting in a three-dimensional random motion of the particles in solution (Fig. 1).

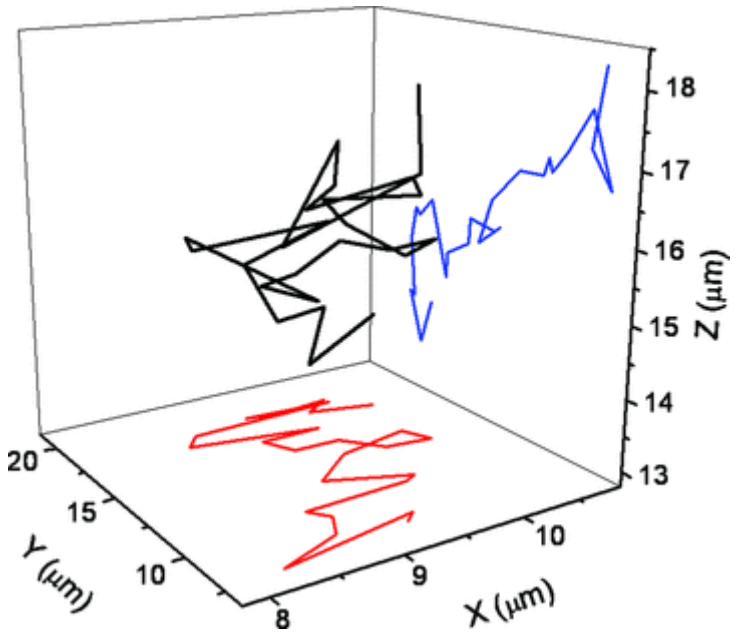

Figure 1: A typical trajectory (in black) of a nanoparticle experiencing Brownian motion along with the projections of the 3D trajectory onto the xy (in red) and yz (in blue) planes [7].

This type of random diffusion, also called Brownian motion, reported for both inorganic particles and biological entities (such as non-motile bacteria, intracellular organelles and viruses) [7-10], was first observed by the botanist Robert Brown in 1827, investigating the random motion of pollen grains in water [11]. After approximately 80 years, Albert Einstein provided a physical explanation of this phenomenon and laid the foundation for a rigorous

mathematics model linking the microscopic with the macroscopic world, providing the mathematical formulation for the diffusion constant D [12]:

$$D = \frac{K_b T}{6\pi\eta r} \qquad Stokes - Einstein\ equation \tag{1}$$

Where K_b is the Boltzmann constant, T and η are the temperature and the viscosity of the medium respectively and r is the radius of the particle.

Equation 1 is widely accepted and used to predict the diffusion of particles even at the nanoscale and it is the basis of popular particle sizing techniques like Nanosight (NTA) and Dynamic Light Scattering (DLS).

However, a recent study disputed the reliability of equation 1 in describing the diffusion coefficient of nanoparticles and evaluated experimentally the diffusion coefficient from the Mean Square Displacement (MSD), a measure of the deviation of the position of a particle with respect to a reference position over time [13]:

$$MSD = \frac{1}{N-n}\sum_{i=1}^{N-n}(\vec{r}_{i+n} - \vec{r}_i)^2 \qquad n = 1, \dots\dots, N-1 \tag{2}$$

Equation 2 describes the average particle square displacement for all possible time lags in a particle trajectory. *N* is the total number of frames for that trajectory, r is the position of the particle and *n* is the number of time intervals. By measuring MSD, it is possible to determine the nature of the motion of the particles. For Brownian motion, in the absence of a directed or restricted diffusion, the relation between the MSD and the diffusion coefficient is linear and given by:

$$MSD = 2dDt \tag{3}$$

Where *d* is the number of dimensions in which the diffusion occurs, *D* is the diffusion coefficient and *t* is the time. In the case of directed diffusion, or diffusion with flow, the relation

between the MSD and the diffusion coefficient is quadratic with respect to time (*t*) and average velocity of the flow (*V*) [14]:

$$MSD = 2dDt + V^2t^2 \quad (4)$$

Exploiting equation (3), several studies demonstrated that the classical Stoke-Einstein equation is not reliable in predicting the diffusion of nanoparticles in simple fluids and proposed a fractional version of equation (1), where the diffusion exhibits a fractional dependence on viscosity [15, 16]:

$$D \propto \eta^{-t} \quad (5)$$

Where η is the viscosity of the medium and t is a constant with a value between 0 and 1, found by experiment.

Also relevant is the study conducted by Coglitore et al., who demonstrated not only the unreliability of equation 1 to predict the diffusion coefficient in simple fluids for nanoparticles below 150 nm in diameter and at a concentration below 10^9 particles ml^{-1}, but also that diffusion is independent on the density and size of nanoparticles [5].

The other process regulating the motion of nanoparticles through liquid solutions is the sedimentation process. Gravitational sedimentation becomes relevant for dense particles (such as metallic particles) with a diameter larger than 10 nm, causing the particles to sediment down and settle [17]. The sedimentation process was first mathematically described by Stokes, who related the sedimentation velocity of nanoparticles to the properties of the nanomaterial and solution in use [18]:

$$V_s = \frac{g(\rho_{NM} - \rho_M)d^2}{18\eta} \qquad Stokes'\ Law \quad (6)$$

Where g is the acceleration of gravity, ρ_{NM} and ρ_M are the mass densities of the particle and of the solution respectively, d is the diameter of the particle and η is the viscosity of the solution.

It should be noticed that equations 1 and 6 do not take into account the influence on the dynamics of nanoparticles of inter-particles forces dominant at the nanoscale, such as Van der Waals and electrostatic interactions, and the majority of the studies in the literature take into account only the physical parameters identified by the equation 1 and 6, ignoring the potential influence of any electrochemical interaction. However, inter-particle forces have been already reported to directly influence a range of phenomena including surface adhesion, friction, and colloid stability [19, 20]. The empirical characterisation of the diffusion dynamics of gold nanoparticles in NaCl solutions proposed in this thesis aimed to investigate the role that interaction forces play at the nanoscale, where their effect is stronger due to the high surface area to volume ratio of the particles and can potentially lead to deviations from the expected behaviour. A clear understanding of the influence of interaction forces on the dynamics of nanoparticles is particularly relevant for characterising the dynamics of nanoparticles in complex media containing a non-negligible ionic content in their formulation, such as cell culture media, with potential direct implications in toxicological and pharmaceutical investigations involving nanoparticles interacting with cells.

2.1.2. The sedimentation – diffusion equilibrium

The diffusion and sedimentation processes act concurrently to regulate the motion and transport of particles dispersed in solution. Because of diffusion, particles tend to move from zone of high concentration of particles to a zone of low concentration of particles, randomly but uniformly distributing over the entire available volume of the fluid. At the same time, gravitational sedimentation promotes a flux of particles towards the bottom of the solution. In a confined solution, the influence of both forces results in a concentration gradient of particles

from the bottom to the top of the solution. The concentration gradient promotes an overall upwards diffusion flux for particles in a zone of high concentration of particles (i.e. close to the bottom of the solution), opposite to their sedimentation flux. When the diffusion flux equals the sedimentation flux, a so-called sedimentation–diffusion equilibrium is achieved (Fig. 2).

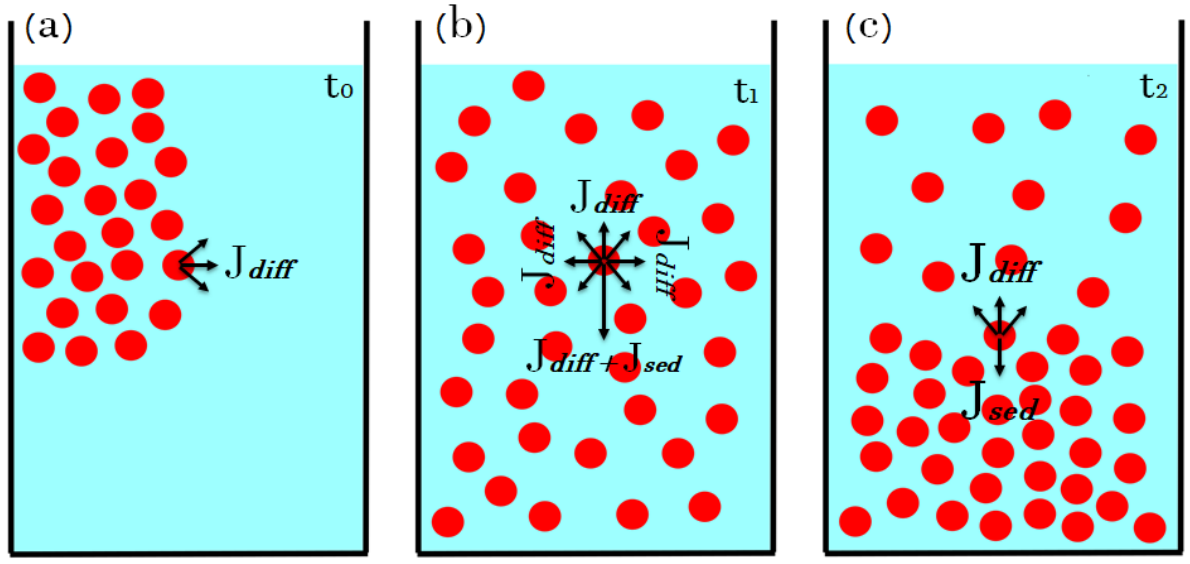

Figure 2: Schematics of the three phases of sedimentation-diffusion equilibrium for nanoparticles in solution: (a) once injected in solution nanoparticle dynamics is mainly regulated by diffusion forces. Nanoparticles are dispersed over the entire available volume; (b) nanoparticles are randomly but homogeneously dispersed in solution. Gravity tends to direct particles to the bottom of the solution; (c) sedimentation–diffusion equilibrium is attained. The rate of transport of nanoparticles in any one direction due to sedimentation equals the rate of transport in the opposite direction due to diffusion.

The most common theoretical model used to describe the concentration profile of nanoparticles in solution is the well-known Mason–Weaver equation, which combines the sedimentation and diffusion processes to predict the concentration of a solute at a certain depth in a solution [21]:

$$\frac{\partial n(z,t)}{\partial t} = D\frac{\partial^2 n(z,t)}{\partial z^2} - V\frac{\partial n(z,t)}{\partial z} \qquad Mason\text{–}Weaver\ equation \qquad (7)$$

where $n\ (z,\ t)$ is the normalized concentration of nanoparticles, D is the diffusion coefficient evaluated with equation (1) and V is the sedimentation velocity evaluated with equation (6). Being based on the Stokes-Einstein and on the Stokes equations, the Mason-Weaver model is subject to the same limitations as its constitutive equations, assuming the absence of interactions between nanoparticles and that their motion is only governed by random Brownian

forces and a directional gravitational force [22]. Hence, this thesis aimed to evaluate the settling dynamics exhibited by nanoparticles in solution and the potential deviations from the current standard theoretical models in simple and biological media. This finding has direct implications in all the investigations where the precise amount of material delivered to a surface is needed to develop a dose-response assessment [23]. For instance, the standard experimental practice to investigate the interaction between nanoparticles and cells consists of culturing a 2D adherent monolayer of cells and evaluating the response of the cell when exposed to a certain concentration of nanoparticles. However, investigators use the initial administered concentration of nanoparticles in the cell medium as a basis to determine dose-response relationships without taking into account that the concentration at the cellular level could differ from the initial administered one [24, 25].

2.2. The DLVO theory

The DLVO theory (named after Boris Derjaguin and Lev Landau, Evert Verwey and Theodoor Overbeek) describes particle interactions by combining electrostatic potential due to repulsive electrostatic double layer, and attractive Van der Waals interactions [26]. van der Waals force promotes coagulation, while the electrostatic double-layer force stabilizes the suspension. The DLVO curve has a non-monotonic behaviour and interaction between two particles can be described by a weak attraction at large distances, an electrostatic repulsion at intermediate distances, and a strong attraction at short distances. As the distance between two particles increases, the interaction energy (potential) approaches zero (Fig. 3). On the other hand, as the particles start to approach each other, the attractive forces increase, and the total interaction energy becomes attractive. The interaction between particles at the secondary minimum (large distances) is weak, and adhesion is reversible. When particles approach closer proximity, the potential energy barrier prevents irreversible adhesion, thus leading to stabilization due to electrostatic force. Hence, the primary maximum acts as an activation barrier that must be

exceeded for irreversible aggregation to occur. As two particles come closer, they must collide with sufficient energy to overcome the energy barrier. The height of the barrier defines the stability of a given colloidal system and depends mostly on the electrostatic repulsion energy acting between particles [27].

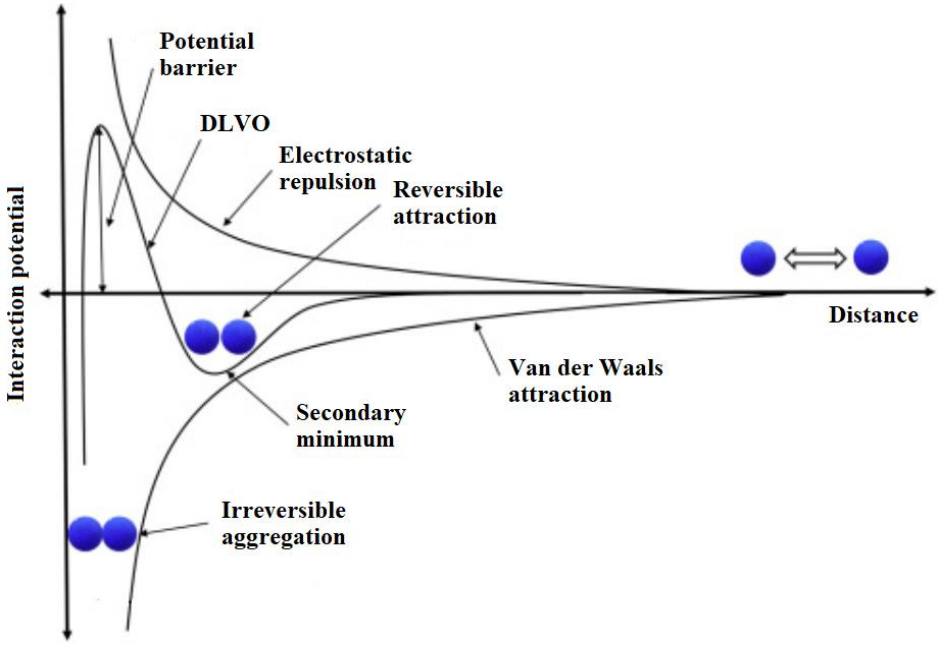

Figure 3: Interaction potential acting between two particles as a function of the distance according to the DLVO theory.

2.3. Single particles tracking methods

Single-particle tracking techniques have become fundamental to locate particles and track their trajectory over time, providing quantitative and empirical information about their dynamics, allowing challenging theoretical models and evaluating potential deviations from expected behaviours. Single-particle tracking methods are extensively used in a range of applications such as physics, engineering, material science, and biology. In a typical single-particle tracking measurement, the object of interest is imaged over time and its motion is recorded in a time series to generate a trajectory. From the analysis of the trajectory produced, it is possible to extract quantitative information about the diffusion and sedimentation processes of the object, adsorption−desorption dynamics, interactions with the environment, etc. [28]. Given the small size of the particles and molecules of interest, fluorescence microscopy is the most commonly

used single-particle tracking technique, thanks to its high resolving power and ability to increase the signal generated by particles and molecules at the nanoscale. In fluorescence microscopy imaging, non-intrinsically fluorescent particles and organisms are conjugated to an organic fluorescent label. The fluorescent label can be a fluorescent protein, a fluorescent dye, or a quantum dot and considerations of which type of label to use are influenced by a number of factors, particularly the delivery of the label to the target protein/particle, and the photophysical properties of the probe [29]. Once labelled, particles are then imaged in a fluorescence microscope and their position is recorded by a camera over time [30]. However, the exposure to the excitation light can alter the molecular structure of the fluorescent label, causing the destruction of the fluorescent label and the loss of the optical signal (photobleaching), limiting the imaging capability of this technique to short periods of time [31]. Moreover, the destruction or alteration of the fluorescent label can lead to the release of toxic substances in the surrounding medium (phototoxicity) [32]. Fluorescent tagging has been also reported to interfere with native protein behaviour and, or function [33]. Finally, little is known about the influence of the fluorescent label on the dynamics of the particles labelled. Hence, there is a need for imaging techniques with high spatiotemporal resolution yet low propensity for photobleaching and phototoxicity to non-invasively characterise the dynamics of target particles and organisms.

Several optical techniques have been developed in recent years to overcome the limitations of fluorescence microscopy for the real-time investigation of the dynamics of nano and micro particles and organisms in solutions. Amongst others, digital holographic microscopy has been proven to be able to track gold nanoparticles as small as 100 nm in diameter [34]. In a typical in-line digital holographic microscope, a collimated laser illuminates the sample, and an objective collects the scattered and transmitted light that is focussed by a tube lens into a digital camera which records the resulting interference pattern, or hologram [35]. The recorded

hologram is then analysed over-time to extract quantitative information about the motion of the particle. Digital holographic microscopy has been used to visualise and track the dynamics of a variety of metallic particles and organisms but both the maximum resolution achievable (100 nm in diameter) and the light source used limit the applications of the technique.

2.4. Real time optical tracking of label free nanoparticles with caustics

The use of a coherent source of light to generate an optical signature from a particle at the nanoscale in solution was pursued also by Patterson and Whelan exploiting the optical phenomenon of caustics [36]. Caustic curves are generated by the refraction or reflection of light at curved surfaces. This phenomenon was first observed by Hamilton in the early XIX century, who described the formation of caustic curves when light rays are reflected from curved surfaces [37]. The same phenomenon is seen in transmission of light rays through objects that have curved surfaces. The effect of the curvature is to cause the reflected/refracted envelope of light rays to concentrate in some regions in space and to be absent from others. These optical features are formed in three dimensions and can be observed as bright lines when imaged on a plane perpendicular to the incident light [36]. Caustics can be observed in everyday situation, such as when light is reflected by the curved surface at the bottom of a cup of tea or when light is refracted by the surface waves of a body of water (Fig. 4).

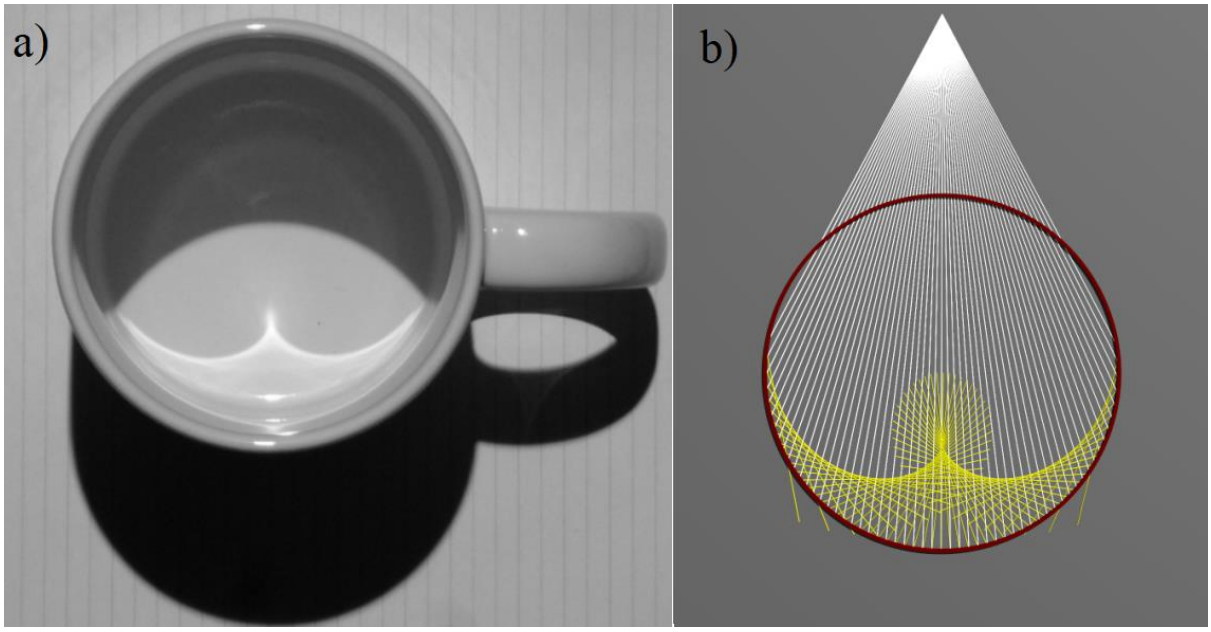

Figure 4: a) Caustics generated by the reflection of the light by the curved surface of a cup of tea and b) schematics of the caustic curves generation when an incident light is reflected by a circular surface.

Caustics have been used in engineering both in reflection and transmission mode [38 - 39] to evaluate the stress distributions associated with the tips of propagating cracks, contact between components and other stress raisers. Stresses alter the optical properties of a solid both through the effects of compression/expansion and through changes in the refractive index. When a flat surface is illuminated by a parallel incident light beam, the stressed areas induce deflections of the incident light beams, causing the light distribution to be no longer uniform because of the generation of caustic signatures [39]. The caustic curves generated are larger than the real local deformation of the material caused by the stresses of interest, allowing for the recognition of the shape of the localized deformation of the object and to evaluate the stress singularity causing the deformation. It has been shown that the formation of sharp caustics is enhanced by the use of a coherent illuminating light [40]. The source of light used by Patterson and Whelan to generate caustic curves of nanoparticles was a common halogen lamp and the coherence of the illuminating light was increased by closing down the condenser aperture to its minimum (1 mm in diameter) and by putting a green interference filter in the light path. The microscope

was also adjusted for Köhler illumination, to provide the sample with homogeneous illumination and to generate images at the highest obtainable resolution [36]. Using this optical set-up they were able to generate caustics curves from the particles in solution and to visualise spherical metallic nanoparticles as small as 10 nm in diameter in a common optical microscope [41]. The caustic signature generated by a particle consists of a central bright spot surrounded by concentric and much fainter diffraction rings (Fig. 5).

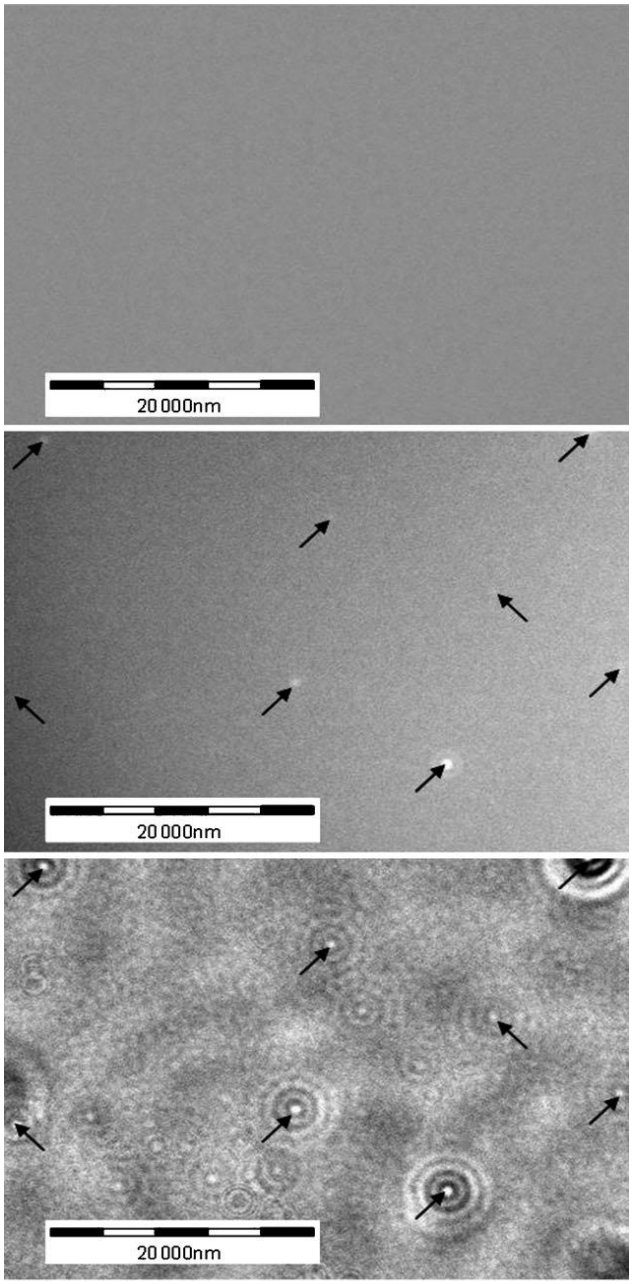

Figure 5: Nominally 20-nm-diameter gold particles and 50-nm-diameter fluorescent particles viewed in the microscope with the aperture diaphragm open (top); under fluorescent conditions with the gray level extended (middle); and with the aperture-diaphragm closed to its minimum with the gray level extended (bottom). The arrows show the position of 50-nm-diameter particles identified using the fluorescent image [41].

The caustic optical signatures are several orders of magnitude larger than the particles under test, allowing for the imaging and tracking of the particles over time and the discrimination between single particles and clusters. Coglitore et al by tracking the caustics optical signature of gold and polystyrene spherical gold nanoparticles in simple fluids, demonstrated that below a critical concentration of 10^9 particles ml^{-1} and a critical diameter of 150 nm the diffusion

coefficient of particles in simple fluids falls orders of magnitude below the Stokes-Einstein prediction and it is better represented by the fractional Stokes-Einstein relation. In these experimental conditions, the diffusion coefficient was found to be constant with particle size and independent of the material, but dependent on fluid viscosity [5].

In this study, the imaging capability of the optical method based on caustics has been enhanced to monitor the dynamics and interactions of a range of nanoparticles and biological organisms. The results obtained demonstrate that the caustic signatures allow real-time and non-invasive quantification of the dynamics of particles, bacteria and intracellular organelles at the micro/nano scale over an extended timescale, representing a powerful alternative to more traditional imaging techniques in a variety of investigations such as: nanotoxicology; drug delivery; intracellular motility/trafficking; antimicrobial efficacy, etc.

2.5. Bacteria dynamics and interaction with surfaces

Bacteria are prokaryote, single-cell organisms with an average size between 0.2 μm and 5 μm in diameter, depending on their structure and shape. The main internal components found in all bacterial cells are the nucleoid and the ribosomes. The nucleoid is a nucleus-like structure without a nuclear membrane where the bacterial genomic DNA is condensed and functionally organised. The ribosomes are made from complexes of RNAs and proteins and serve as the site for protein synthesis in the cell. The ribosome reads the sequence of the messenger RNA (mRNA) and, using the genetic code, translates the sequence of RNA bases into a sequence of amino acids. The nucleoid and ribosomes are located in the cytoplasm, a gel-like substance made up of water, proteins, lipids, nucleic acids, and inorganic salts, enclosed within the cell membrane. The membrane of Gram – negative bacteria (as the *Escherichia coli* subject of this study) consists of three layers: the cytoplasmic membrane, the peptidoglycan cell wall, and the outer membrane [42]. During bacteria growth and at the start of the division process, the genetic material is split into consecutive compartments divided by the so-called Z-ring, which serves

as a scaffold to recruit the FtsZ division proteins, and possibly generates force to constrict the cell (Fig. 6) [43].

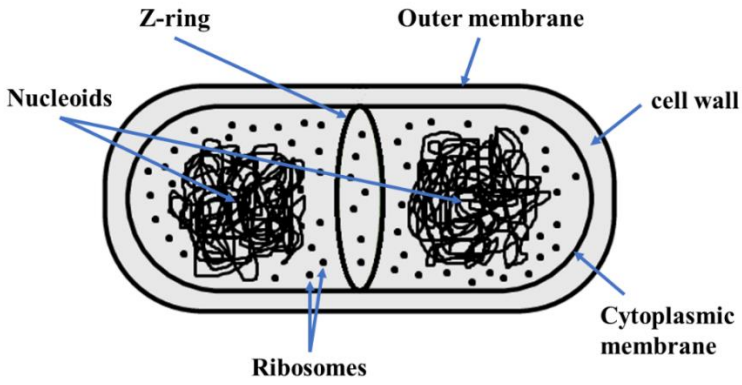

Figure 6: Schematics of a typical Escherichia coli bacterial cell at the start of the division process.

When dispersed in a solution, bacterial cells are transported to the underlying solid surface either by physical forces or by an intrinsic locomotion ability. Motile bacteria use structures, such as flagella, to approach the surface, guided by chemotactic, aerotactic, or phototactic responses. Motility promotes both initial interactions with the surface and movement along it. On the other hand, non-motile bacterial cells, are delivered to the surface by diffusion - sedimentation processes and by gravitational forces or by the flow of the fluid in which they are suspended [44]. Once a bacterium has approached the surface, the initial attachment is regulated by: attractive and repulsive forces, mainly Van der Waals and electrostatic interactions; the properties of the surface such as texture, roughness, and hydrophobicity; and, the properties of the solution such as pH and temperature [45]. However, attached bacteria can detach from the surface and re-join the planktonic state in a process called reversible adhesion, as a result of hydrodynamic forces, repulsive forces, or in response to nutrient availability [46]. If the environmental conditions are favourable, a bacterium attaches permanently to the surface and starts to secret extracellular polymeric substances (EPS), establishing a permanent bond with the surface (known as irreversible adhesion) and favouring the attachment of additional

bacteria to start a biofilm [47]. The transition from the individual planktonic state (single bacteria cell floating in solution) to a biofilm enhances the tolerability of bacteria to antibiotics and their growth, even in adverse conditions [48]. Bacterial biofilms can easily form on medical devices and human tissues, leading to chronic and life-threatening infections and account for up to 80% of nosocomial infections in the US [49]. Moreover, antibiotic resistance is widely considered to be a potential trigger for the next global pandemic [50]. For these reasons, strategies have been developed over the last decades to prevent bacterial biofilm formation on surfaces, with the development of a range of so-called antimicrobial surfaces and coatings. These surfaces are designed to either kill bacteria on contact or close proximity (biocidal surfaces) or to prevent irreversible attachment (adhesion resistance surfaces). However, the preliminary bacteria–surface interaction and the subsequent early-stage biofilm formation processes have not yet been clearly characterised, and a detailed understanding of the mechanism regulating these processes is needed to develop effective antimicrobial strategies and to support their translation to in-vivo and real-life scenarios. The investigation performed in this thesis aimed to characterise the mechanism of attachment of bacteria to surfaces and the ability to form biofilms to support the investigation and development of antimicrobial surfaces and coatings.

2.6. Intracellular organelles dynamics

A cell consists of two major regions, the cytoplasm and the nucleus. The nucleus is surrounded by a nuclear envelope and contains DNA in the form of chromosomes. The cytoplasm is a fluid matrix surrounding the nucleus and bound to the outer membrane of the cell. Organelles are structures ranging from approximately 100 nm to 1 μm in size within the cytoplasm, carrying out functions necessary to maintain homeostasis in the cell. They are involved in many processes, such as energy production, building proteins and secretions, and destroying toxins. Organelles identifiable in human cells in the cytoplasm surrounding the nucleus are [51]:

- Ribosomes: consisting of two subunits made of RNA and protein, these organelles are responsible to synthesize a variety of proteins that are essential to the survival of the cell. They can be found floating freely in the cell's cytoplasm or embedded within the endoplasmic reticulum.
- Endoplasmic reticulum: a membranous organelle that shares part of its membrane with that of the nucleus. Some portions of the endoplasmic reticulum, known as the rough endoplasmic reticulum, are studded with ribosomes and are involved with protein manufacture. The rest of the organelle is referred to as the smooth endoplasmic reticulum and serves to produce vital lipids.
- Mitochondria: oval-shaped organelles found in most eukaryotic cells. They are the site of cellular respiration and serve to transform molecules such as glucose into an energy molecule known as ATP (adenosine triphosphate). ATP fuels cellular processes by breaking its high-energy chemical bonds.
- Peroxisomes: membrane-bound organelles containing oxidative enzymes. They are mainly responsible in the lipid metabolism process and in the conversion of reactive oxygen species (as hydrogen peroxide).

- Endosomes: heterogeneous collection of organelles that function in the sorting and delivery of internalized material from the cell surface and the transport of materials from the Golgi to the lysosome.
- Lysosomes: spherical membrane-bound organelle containing hydrolytic enzymes to break down / hydrolyse macromolecules, old cell parts, and microorganisms.
- Golgi apparatus: composed of folded membranes, it is responsible for transporting, modifying, and packaging proteins and lipids.

The interaction between different organelles and their specific dynamics have been also reported to be pivotal to the regulation of several cellular processes. For instance, the interaction between lipid droplets and lysosomes is critical for the metabolism of cellular energy with dysfunction being correlated with various metabolic and lysosomal storage diseases [52]. Lysosomes have also been reported to interact with mitochondria to regulate mitochondrial calcium dynamics [53] and their spatial distribution is influenced by the availability of nutrients [54]. Peroxisomes have been reported to interact actively with mitochondria to regulate the fission (one mitochondria divide or segregate into two separate mitochondrial organelles) and fusion (two separate mitochondria fuse together to form a large one) processes [55]. The endoplasmic reticulum (a vast organelle that has a central role in protein biogenesis, and lipid and ion homeostasis) performs its functions by forming physical contacts with all other membranous organelles through membrane contact sites [56]. Moreover, Guo et al. hypothesised that the random fluctuation exhibited by intracellular organelles in the cytoplasmatic fluid contributes to the spatial distribution of key cellular components, such as ribosomes and proteasomes, to facilitate the efficient translation and degradation of proteins and the removal of enzyme products from their site of synthesis in metabolic reactions (avoiding local concentration effects) [57].

Hence, it is reasonable to assume that the activity internal to the cytoplasm consists of a complex system of interdependent interactions regulating cellular functions, and that a clear understanding of the forces and mechanisms influencing those interactions is needed to relate intracellular processes to cell physiology in healthy and diseased states. The investigation performed in this thesis aimed to establish the ability of the optical set-up based on caustics coupled with digital image correlation analysis to characterise the motion internal to the cytoplasm, in an effort to provide a non-invasive imaging tool to support future investigations exploring the relationship between the dynamics of intracellular organelles and cellular processes.

CHAPTER 3

3. Materials and Methods

3.1. Materials

3.1.1. Gold nanoparticles

Spherical, negatively charged, citrate-capped gold nanoparticles (solution pH 7.7) were purchased from BBI Solutions (Crumlin, UK), with a nominal diameter of 20 nm, 40 nm, 50 nm, 60 nm, 80 nm, 100 nm and 150 nm. Spherical, positively charged, branched polyethylenimine-capped gold nanoparticles (solution pH 7) were purchased from nanoComposix (San Diego, US), with a nominal diameter of 100 nm. Depending on the experimental requirements, the as-supplied concentrations were reduced by adding the concentrate to ultrapure-deionised 0.2 µm membrane filtered water to obtain constant working concentrations ranging from 10^8 to 10^{11} particles ml^{-1}.

3.1.2. Bovine Serum Albumin nanoparticles

Bovine serum albumin (BSA, purity > 96%) was commercially supplied by Sigma Aldrich (Saint Louis, USA). BSA nanoparticles were synthesised following a modified desolvation process [58]. Briefly 100 mg of BSA was dissolved in 10 ml of ultrapure water. Then, 8.0 ml of ethanol was added dropwise into the BSA solution while magnetically stirring (600 rpm) at room temperature. Subsequently, the as-prepared BSA nanoparticles were cross-linked with 5% glutaraldehyde for 24 h. The particles were centrifuged at 8,000 rpm for 10 mins at 25 °C and washed with ultrapure water. The dynamic light scattering measurements confirmed the presence of monodispersed BSA nanoparticles in solution with a diameter of 45 nm ± 1.5 nm.

3.1.3. Organisms

Bacterial imaging was performed with *Escherichia coli* ATCC 10536 strain, a non-motile bacterial strain used for antimicrobial investigations.

Intracellular dynamics were investigated using human mesenchymal stem cells purchased from Lonza systems (CH).

3.1.4. Base media

Ultrapure-deionised 0.2 µm membrane filtered water was provided by a purifier system (Purelab Option-Q, Elga Veolia) at 12MΩ/cm.

Salt solutions with ionic strengths ranging from 0 to 50 mM were realised by mixing Sodium Chloride (NaCl, Sigma Aldrich, US) to ultrapure-deionised water as appropriate.

Phosphate buffered saline (1X PBS, PH 7.4) and Luria-Bertani (LB) broth solutions were commercially supplied by Sigma Aldrich (US).

Cell culture media used in this thesis consisted of DMEM with low concentration of glucose (1 g L^{-1}) commercially supplied by Sigma Aldrich (US), supplemented with 10% FBS (Gibco, US), 2% penicillin-streptomycin (AppliChem, US), 1% L-glutamine (200 mM solution, Gibco, US).

3.2. Methods

3.2.1. Optical Setup

Caustic signatures of the particles, bacteria, and intracellular organelles investigated in this work were generated in a standard inverted optical microscope (Axio Observer.Z1 m, Carl Zeiss, DE) used in transmission mode and mounted on antivibration feet (VIBe, Newport, US) to isolate the sample from the environment. Some simple adjustments were made to the original setup of the microscope to increase the coherence of the illuminating light following the methods described by Patterson and Whelan [36]. In brief, the microscope was adjusted for Köhler illumination and equipped with a 100W halogen lamp, a condenser lens-assembly, and a green interference filter (Olympus, JP, centred on 550 nm, 45 nm bandwidth). The condenser aperture was closed down to its minimum (1 mm in diameter) so that the sample was

illuminated by a coherent and focused ray of light. Images and videos were acquired using a CCD monochrome camera (AxioCam ICm1, Carl Zeiss, DE) coupled to the camera port on the microscope. A stage-top incubation system (Incubator PM S1, Heating Insert P S1, Temp and CO_2 module S1, Carl Zeiss, DE) was used to control the temperature during the experiments.

3.2.2. The influence of interparticle forces on the diffusion dynamics

To evaluate the influence of interparticle force on the diffusion dynamics, gold nanoparticles were dispersed in solutions with ionic strengths ranging from 0 to 50 mM as appropriate to obtain particle concentrations of approximately 10^8 particles ml^{-1}. A mixer (Vortex-Genie 2 G560E, Scientific Industries Inc., US) was employed to obtain a uniform particle distribution. Four independent solutions were prepared for each NaCl molarity and 60 µl of solution of nanoparticles was used in a deep cavity (250 ± 10 µm in depth) in sterile microscopy slides (Eisco Labs, US). For each salt solution at least six particles were tracked so that the diffusion data presented are average values with standard deviations. The temperature of the solution of nanoparticles was kept constant during the microscopy analysis at a value of 23 °C. The X-Y spatial coordinates of the nanoparticles at each time step were evaluated using the imageJ plugin Trackmate. Amongst the various particle-linking algorithms available, Trackmate allows for the tracking of particles using an algorithm based on the linear assignment problem mathematical framework. Given a set of detected particles throughout a time-lapse image sequence, the algorithm first links the detected particles between consecutive frames, and then links the track segments generated in the first step to simultaneously close gaps and capture particle merge and split events. The framework is independent of problem dimensionality (2D or 3D) as well as of the type of particle motion (Brownian motion and directed motion, among others). It is also independent of the physical nature of the particle (single molecule, molecular assembly, organelle and others) [59]. The experimental value for the diffusion coefficient of each particle was calculated from its Mean Square Displacement as described in equation 3.

3.2.3. Settling dynamics of nanoparticles

The settling dynamics of nanoparticles in solution was investigated by dispersing gold nanoparticles in ultrapure-deionised 0.2 μm membrane filtered water or sterile cell culture media to obtain a working concentration of approximately 10^8 particles ml^{-1}. The concentration profiles of the nanoparticles in solution were evaluated using 60 μl of nanoparticle solution in a 250 μm ± 10 μm deep cavity in a microscopy slide and acquiring z-stacks from the bottom to the top of the solution. The distance between consecutive images was set equal to 4 μm for a total acquisition length of 250 μm ± 10 μm. The value of 4 μm between consecutive acquisitions was chosen to avoid multiple counting of the same particles (caustic signatures extend for less than 1 μm in length along the z direction [41]). The number of particles in each image was counted using the software ImageJ and integrated from the mid-depth (125 μm ± 10 μm from the bottom) to the top (250 μm ± 10 μm from the bottom) of the solution to obtain the total number of nanoparticles not settled at each time step. The depth of 125 μm was chosen because experimental observations demonstrated that particles formed a sediment that extended over the bottom half of the solution. Nanoparticles in the bottom-half and in the top-half of the solution have been described, for the sake of simplicity, as settled and not-settled respectively, because the term “settle” is commonly used in the scientific community to identify particles forming a sediment. The full concentration profile is not provided because, as the concentration of the nanoparticles forming a sediment increases, the caustics in the bottom half of the solution overlap, making measurements in that section less precise and unreliable. Four solutions were prepared separately for each sedimentation test so that the results presented are average values with standard deviations. Each test was started 5 minutes after the injection of nanoparticles into the solution, to guarantee consistency between experiments and to allow nanoparticles to distribute throughout the medium uniformly but

randomly. The concentration of nanoparticles not settled has been normalised using the following min-max normalisation method so that the data presented are in the range 0 – 1:

$$z_i = \frac{x_i - \min(x)}{\max(x) - \min(x)} \quad (8)$$

Where z_i is the i^{th} normalised value in the dataset, x_i is the i^{th} original value in the dataset, min(x) is the minimum value in the dataset, and max(x) is the maximum value in the dataset.

The settling time of each nanoparticle solution was established by evaluating the time at which the gradient of concentration of nanoparticles not settled over time was less than 5%. The UltraViolet-Visible spectra shown in figures 22b and 23b were acquired in an ultraviolet-visible (UV-Vis) spectrophotometer (U-2900, Hitachi, JP) using 3 ml of the solution of nanoparticles in a 45 mm deep glass cuvette.

3.2.4. Asymmetric flow field-flow fractionation

Asymmetric flow field-flow fractionation (AF4) is a technique used to separate particles of different sizes in suspension by the application of a cross-flow perpendicular to the direction of a longitudinal suspension flow through a thin ribbon-like separation channel. The high-dimensional aspect ratio of the separation channel causes the longitudinal suspension flow to develop a parabolic profile, with a flow velocity that increases from a minimum value at the channel walls to a maximum value at the centre of the channel. The perpendicularly applied cross-flow forces a particle in suspension towards the bottom wall of the channel. A counteracting diffusive force arises due to the concentration gradient formed and drives the particles back towards the centre of the channel [60]. Once the equilibrium between the cross-flow force and the diffusion force is achieved, particles in suspension reside at a certain distance from the accumulation wall depending on their diffusion coefficient and size. Smaller particles equilibrate higher up in the channel and experience a faster longitudinal flow, causing them to elute, or be removed before larger ones, thus allowing separation [61]. The size-separated

suspension of particles can be then characterised and analysed by coupling AF4 to online sizing and concentration techniques, like dynamic light scattering (DLS) and ultraviolet-visible spectrophotometry (UV-Vis), allowing the evaluation of the size distribution of the particles in suspension according to their mass and concentration [62]. A typical fractogram generated by an AF4 coupled with online DLS and UV-Vis detectors for a single elution peak is presented in figure 7.

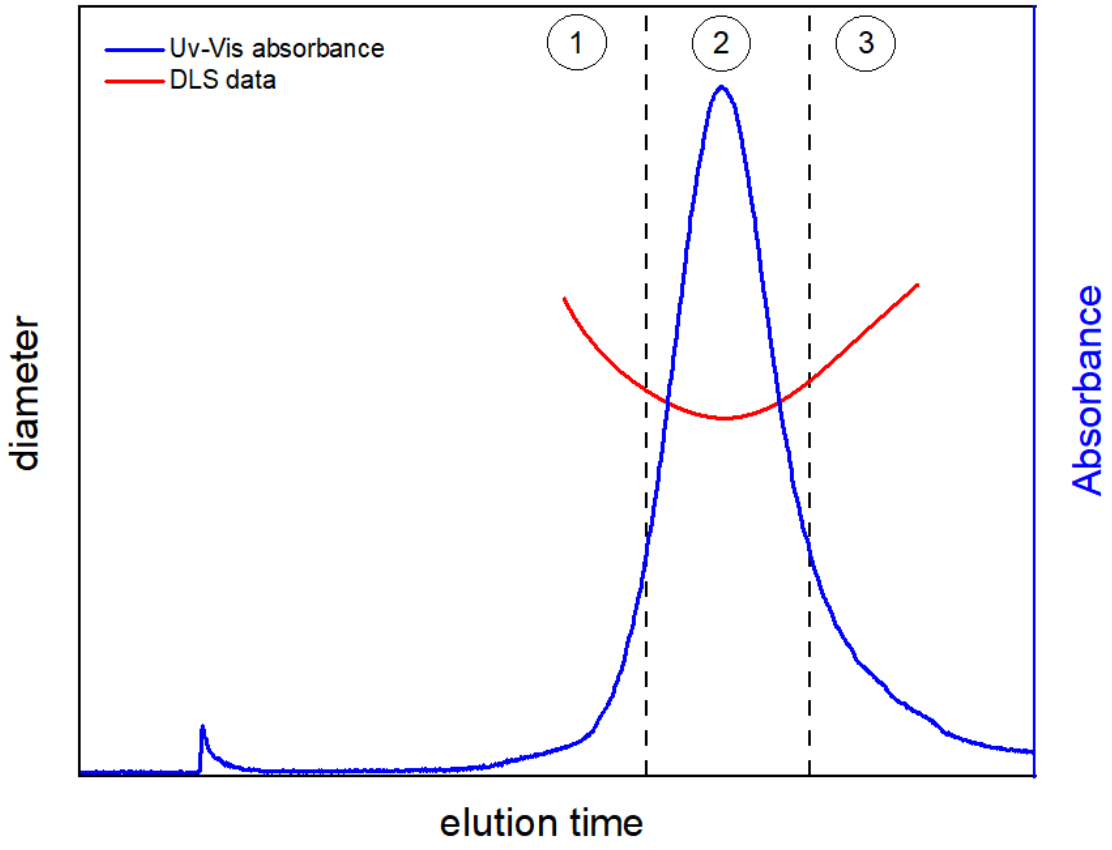

Figure 7: A schematic fractogram generated by an AF4-DLS-UV system for a single elution peak. The fractogram can be divided into three zones according to the absorbance exhibited by the suspension of particles during the elution process. Zones 1 and 3 are associated with low particle concentration while zone 2 is associated with high particle concentrations. It can be noted that in the zone associated with low concentration of particles the DLS data exhibit an apparent and progressive increase.

The fractogram contains quantitative information about the suspension eluted by the AF4, providing the hydrodynamic diameter of the particles recorded by DLS and the absorbance recorded by the UV-Vis spectrophotometer (directly linked to the concentration of particles in

suspension [63]) as a function of the elution time. The Gaussian distribution of the absorbance as a function of the elution time provides evidence that the concentration of particles in solution is lower at the beginning and at the end of the elution process (zone 1 and 3). It can be noted that for low concentrations of particles in suspension the DLS detected an apparent and progressive increase in the size of the particles in suspension, returning a U-shaped distribution for the diameters as a function of the elution time and of the concentration of particles in suspension. This phenomenon can be found in a significant number of studies in the literature describing the application of asymmetric flow field flow fractionation to separate and characterise particles of various sizes and materials [62, 64-68]. It is worth mentioning that the DLS evaluates the hydrodynamic diameter of the particles in solution by rearranging the Stokes-Einstein equation as:

$$d = \frac{K_b T}{3\pi\eta D} \tag{9}$$

Where D is the diffusion coefficient evaluated by quantifying the rate of variation of the light scattered by the suspension over time [69].

Asymmetric flow field flow fractionation analysis was performed to investigate the effect of the experimental slow diffusion regime exhibited by nanoparticles at low concentration on the sizing ability of techniques based on the Stokes-Einstein equation for diffusion. The experiments were performed by injecting gold nanoparticles in concentrations ranging from 10^9 to 10^{11} particles ml^{-1} into an AF2000 Multiflow FFF system (Postnova Analytics, DE) equipped with an on-line PN3212 spectrophotometer UV-Visible detector (Postnova Analytics, DE) and with a DLS detector (Malvern, UK). The AF4 channel had a 280 mm long separation channel, with a 350 μm spacer. A 10 kDa cut-off membrane of regenerated cellulose and a 100 μl injection loop was used. Phosphate buffer (1 mM, ph 7.4) was used as the carrier. The following elution protocol guaranteed the optimal separation and was applied to all suspensions tested: 0.5ml min-1 injection flow; 5 min at constant 1.3 ml min-1 focus flow; exponential

decrease of the cross flow from 1.5 ml min-1 to 0.1 ml min-1 over 35 minutes; 10 min at constant 0.1 ml min-1 cross flow. The UV-Vis spectrophotometer wavelength was set to 525 nm, corresponding to the maximum of the surface plasmon resonance band for 40 nm and 60 nm gold nanoparticles [70]. The suspensions of nanoparticles were injected into the separation chamber in ascending order of initial working concentration. Between each injection, the phosphate buffer was allowed to flow through the entire system for 10 minutes, to remove any residual from the previous suspension.

The reliability of the data provided by the AF4-DLS-UV system was analysed by dividing the fractogram into three regions and evaluating the coefficient of variation of the DLS measurements for each suspension tested. The three regions of the fractogram were identified according to the absorbance detected by the UV-Vis spectrophotometer over the elution time in the following manner:

- Zones 1 and 3: regions of the fractogram where the absorbance of the suspension is lower than 30% of the maximum; and,

- Zone 2: region of the fractogram where the absorbance of the suspension is higher than 30% of the maximum.

A disk centrifugal liquid sedimentation (disk-CLS) analysis was also performed on the same solutions of nanoparticles in a disk centrifuge DC24000UHR (CPS Instruments, US) using 8 wt% to 24 wt% sucrose density gradients with a disc speed of 22000 rpm. Each sample injection of 100 µl was preceded by a calibration step performed using certified PVC particles with a weighted mean size of 237 nm.

3.2.5. Bacterial cell culture

Overnight cultures of *Escherichia coli* were diluted to McFarland Standard 0.5 in Luria-Bertani (LB) broth or phosphate-buffered saline solution (PBS) as appropriate to obtain a working concentration of approximately 10^8 CFU/mL. Bacteria were diluted in pure PBS or in solution of 10% LB in PBS, to reduce the noise generated by the medium nutrients and to limit their growth and ability to proliferate, thus allowing for longer monitoring of the interaction between single bacterium and the target surface, and the subsequent formation of the biofilm. Solutions of bacteria were analysed using 60 µl of solution in a deep cavity (250 ± 10 µm in depth) in sterile microscopy slides. To validate the label-free caustic signature associated with bacteria in solution and adhered to the surface, fluorescence images were acquired with the same optical set-up using a fluorescent light source. *Escherichia coli* bacteria were stained with the fluorescent dyes SYTO9 and PI from the LIVE/DEAD BacLight kit (Invitrogen, US), a well-known fluorescence kit used to assess the viability of bacteria in solution [71]. The kit consists of two components:

- Component A: SYTO 9 dye, 1.67 mM / Propidium iodide, 1.67 mM, 300 µL solution in DMSO
- Component B: SYTO 9 dye, 1.67 mM / Propidium iodide, 18.3 mM, 300 µL solution in DMSO

Bacteria were stained to confirm the ability of the caustic technique to generate optical signatures for all of the bacteria present in the field of view. Bacteria were stained according to manufacturer protocols by combining the same volume of the two components and by adding 3µl of the components' mixture for each mL of the bacterial suspension. The stained solutions were then incubated at room temperature in the dark for 15 minutes. The efficiency of benzalkonium chloride (BKC) as antimicrobial agent and its effect on the bacterial-surface interaction was tested by spreading a 0.1% solution of BKC in ultrapure-deionised water on

same glass surfaces. Then solutions of bacteria were exposed to the surfaces treated with BKC after 3 h, to allow for the complete evaporation of the BKC solution and for the deposition of the BKC film.

The dynamics of the bacteria and their interactions with the surfaces were evaluated by analysing the imaging data acquired with the ImageJ plugin Trackmate [59].

3.2.6. Cell culture and intracellular organelles imaging

Human Mesenchymal Stem Cells (hMSC) were seeded on sterile 16-well culture plate (Grace Bio-Labs, US) at a concentration of approximately 16000 cells/well and left overnight in the incubator to allow full attachment and spreading. Cell cultures were maintained in 5% CO_2, 95% air, and at 37 °C in the cell incubator and then transferred to the microscope incubator during the microscopy analysis to maintain a constant temperature of 37 °C during the experiments. The dynamics of the optical pattern generated by intracellular organelles were investigated by imaging the zone surrounding the nucleus of human mesenchymal stem cells. Attention was focused on the zone surrounding the nucleus because intracellular organelles have been extensively reported to be located in this zone. As a further confirmation, images of 3T3 cells were acquired in caustic and fluorescent mode by switching from the caustic mode to the fluorescence mode and using a different light source. The 3T3 cell culture was provided ready to use by the Toxicology Unit of the Joint Research Centre (JRC) of the European Union. 3T3 cells were stained using the fluorescent dye LysoTracker deep red (Thermo Fisher Scientific, US), commonly used for labelling and tracking acidic organelles in live cells. Cells were stained according to manufacturer protocol by diluting Lysotracker dye stoke solution in the cell culture media to obtain the working concentration of 70 nM. When cells have reached the desired confluence, the original medium was replaced with the dye-containing medium. Then cell cultures were incubated for 1h at 5% CO_2, 95% air, and at 37 °C in the cell incubator

Finally, the dye-containing medium was replaced with fresh medium and the cells were monitored under the microscope.

Figure 8 confirms that intracellular organelles tend to accumulate in the zone surrounding the nucleus.

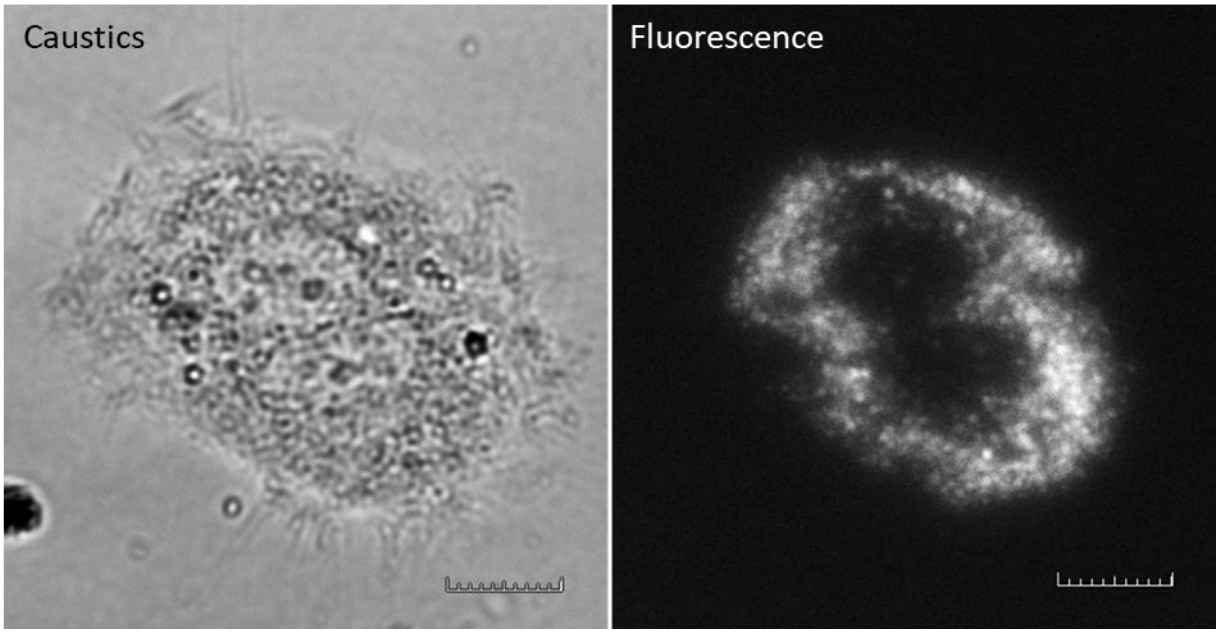

Figure 8: 3T3 cell imaged with an inverted optical microscope in caustics mode (left) and fluorescence mode (right). Scale bars are 10 µm.

Cells were monitored for approximately 5 min recording real-time video at 20 fps. During the imaging, cell cultures were maintained at a constant temperature of 37 °C in the microscope incubator.

External stress was induced in the cell by injecting Ethanol at time t = 150 s into the cell solution to achieve a total concentration of 1% in volume.

The digital image correlation (DIC) package Istra-4D (Dantec Dynamics GmbH, DK) was used to quantify the dynamical re-arrangement of the intracellular organelles pattern over time. The Istra-4D software overlays a grid of square facets on the reference image (Fig. 9). The user selects the facet size and the distance between the two adjacent facet centres depending on the pattern to be analysed. The software utilises a second-order shape function to map each

reference image facet to its displaced location in the next image and the coefficients of the shape function are determined by minimising the sum-squared difference between the intensity patterns of the two images [72]. In this study, the differences between the pattern exhibited by adjacent images of intracellular organelles were determined by defining the preceding image in the stack as the reference image whilst correlating each image.

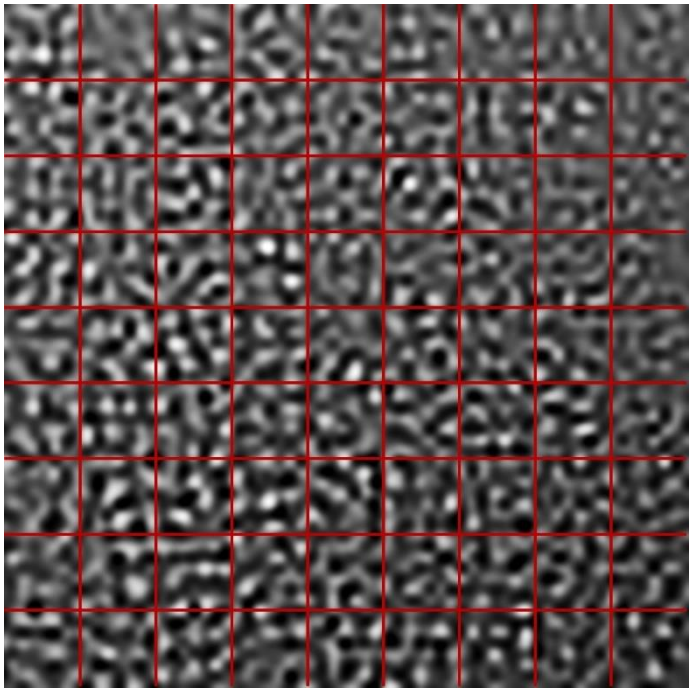

Figure 9: Typical photograph of the area (dimension 29.7 µm x 29.7 µm) outside the nucleus of a stem cell analysed in this study. A grid of squared facets (red lines) is superimposed to the original image by the software Istra-4D. Each facet consists of a region of the sample exhibiting a unique pattern and can be distinguished from the others facets and tracked over time. The DIC software performs the calculation of the displacement for the entire analysed surface analysing the changes in the location of facets in consecutive images.

CHAPTER 4

4. Results and discussions

4.1. Caustics optical signatures of nanoparticles, bacteria and intracellular organelles

Preliminary experiments were performed on gold and bovine serum albumin nanoparticles dispersed in ultrapure deionised water. The typical optical signatures generated by nanoparticles illuminated with the optical setup are shown in figure 10. The caustics signature consists of a central bright spot surrounded by concentric and much fainter diffraction rings and is of the order of magnitude of microns, allowing for direct observation even if the size of the particle is below the diffraction limit and for tracking of a motion of the nanoparticle in real-time without any requirement for fluorescent labelling.

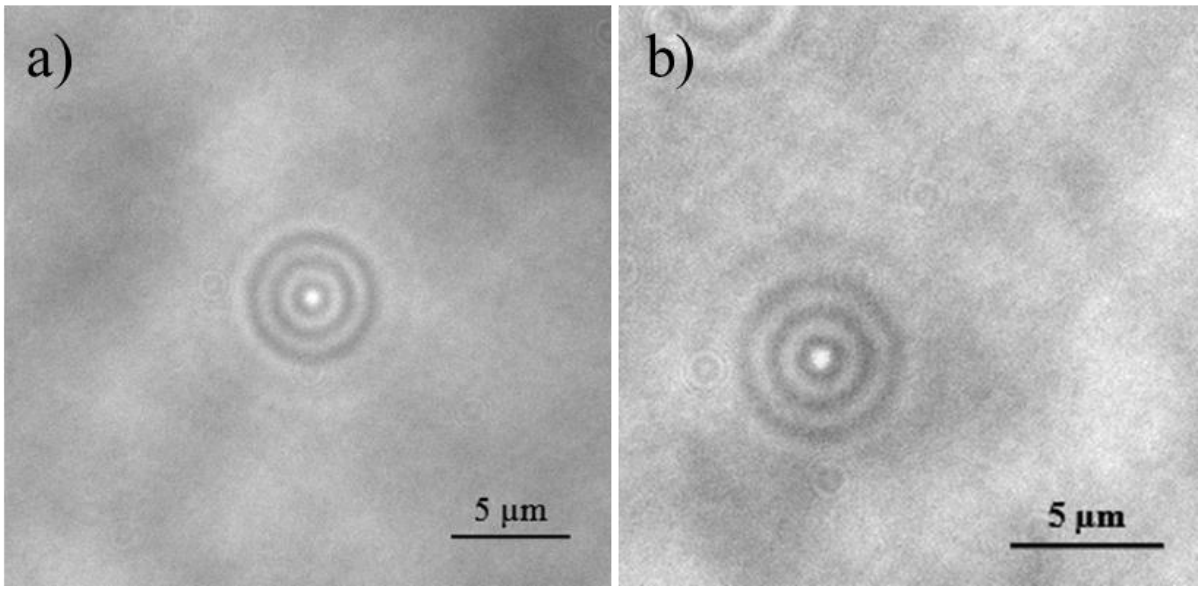

Figure 10: Photograph of a caustic in deionised water generated by: (a) 50 nm gold nanoparticle; (b) 45 nm BSA nanoparticle.

The imaging capability of the optical setup used in this study was also tested for *Escherichia coli* bacteria. Figure 11 shows a comparison between the typical optical signature generated using the caustics mode and the brightfield mode for an *Escherichia coli* bacteria adhered to the surface. Depending on the specific strain, the growth state and the availability of nutrients,

an *Escherichia coli* bacterium exhibits a variable length, approximately in the range of 1 µm – 10 µm [73], hence it is possible to visualize them even in brightfield mode. However, the caustic mode provides a better definition of the macroscale structure of the bacteria and allows the main structural components, namely the membrane, the nucleoids, and the Z-rings to be recognised more easily than in brightfield mode.

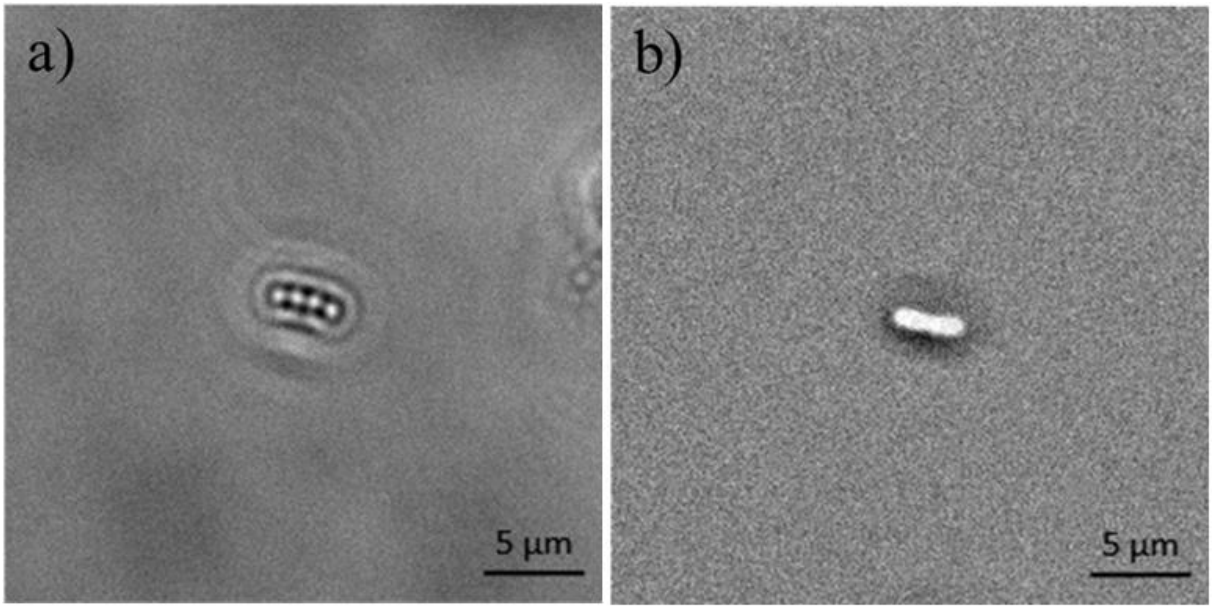

Figure 11: Photograph of the optical signature generated by an Escherichia coli bacteria taken with the optical inverted microscope used in this work set-up for: a) caustics mode; b) brightfield mode.

To confirm the ability of the caustic technique to generate optical signatures for all of the bacteria present in the field of view, consecutives images of the same region of the sample were collected by switching from the caustic mode to the fluorescence mode. Figure 12 shows no significant differences between the two imaging techniques for visualising the concentration of bacteria at a surface. However, the caustics mode allows for a greater depth of field, which permits bacteria to be visualised further from the surface of interest and to monitor how they approach the surface.

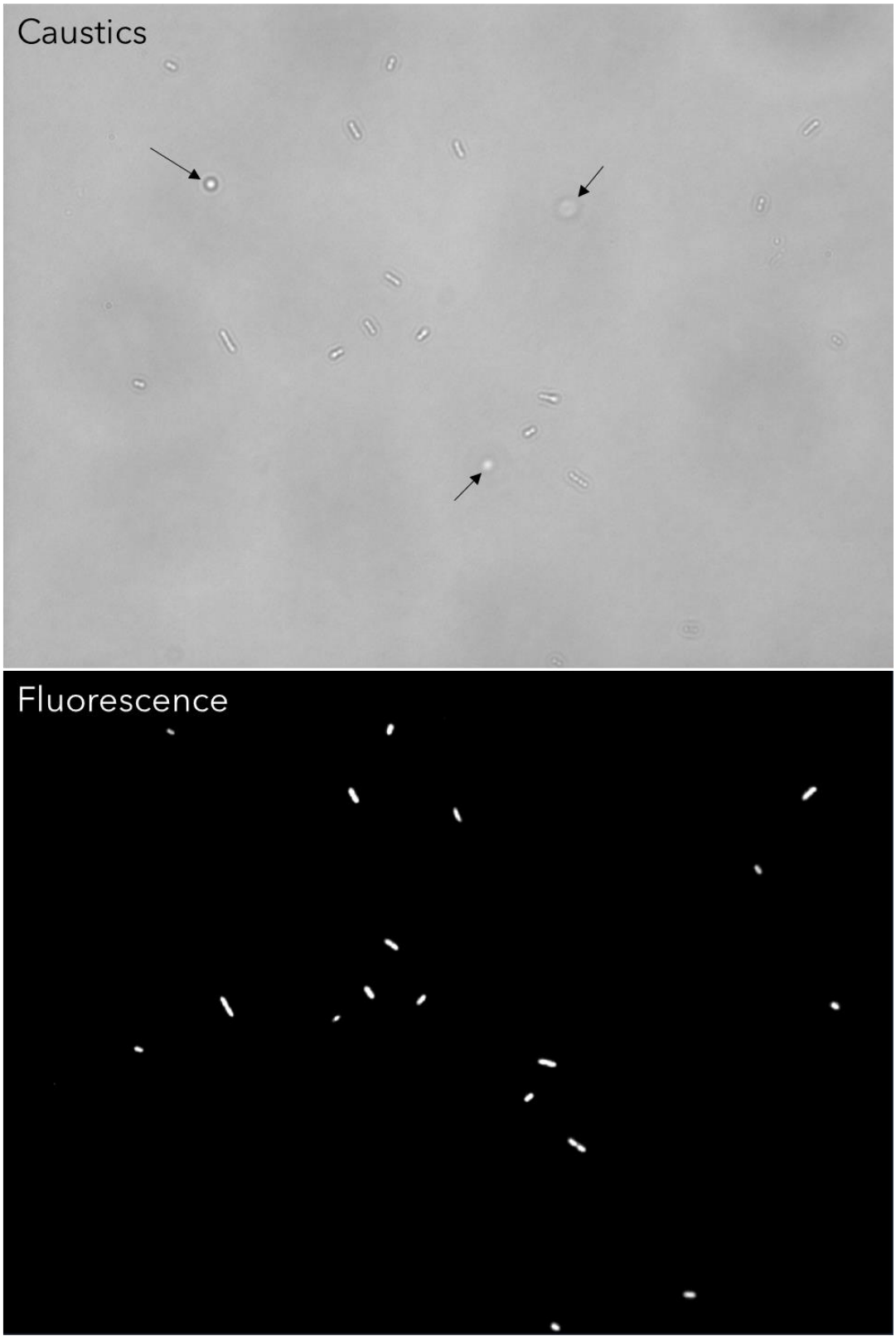

Figure 12: Comparison between the same bacteria population imaged with an inverted optical microscope in caustics mode (top) and fluorescence mode (bottom). There are no significant differences between the two imaging techniques. However, the caustics mode allows for a greater depth of field, which permits bacteria to be visualised further from the surface of interest (highlighted by the black arrows) and to monitor how they approach the surface. The three bacteria not at the surface have been captured when aligned perpendicularly to the surface during their random diffusion, resulting in an almost spherical optical signature.

The caustic optical setup was also demonstrated to be able to generate diffraction patterns from intracellular organelles in human mesenchymal stem cells (Fig. 13).

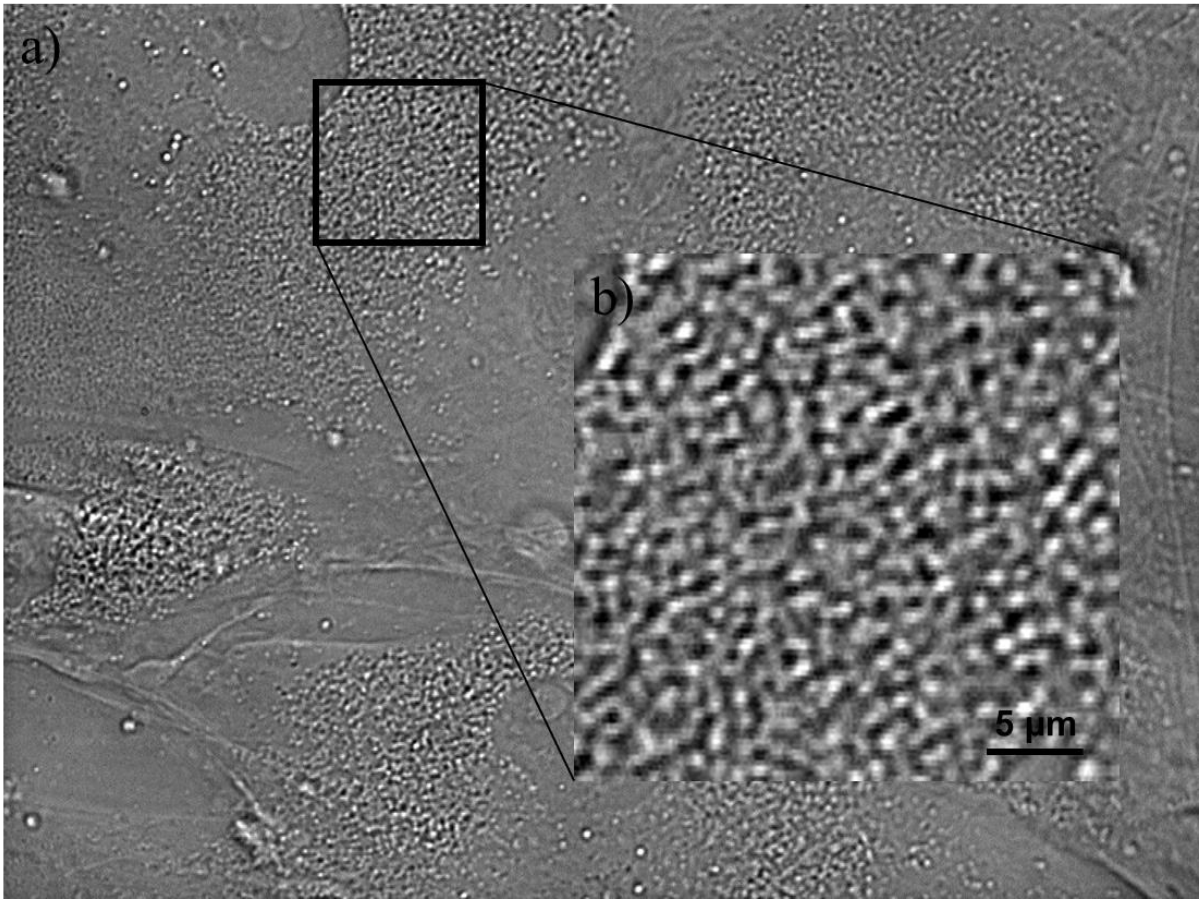

Figure 13: Typical photograph of a) optical signatures generated by a population of human mesenchymal stem cells imaged with the optical inverted microscope used in this work set-up for caustics mode and b) magnification of the area (dimension 29.7 µm x 29.7 µm) outside the nucleus analysed in this study.

The arrangement and variety of intracellular organelles in the cytoplasm does not allow for a single – particle tracking analysis. However, the optical signature generated by intracellular organelles resembles the optical signature produced by the cross-section of continuous fibre reinforced-composite materials, where digital image correlation has proven to be successful in characterising fibre dynamics, orientation as well as damage propagation [72, 74].

4.2. The influence of inter-particle forces on diffusion at the nanoscale

The influence of Van der Waals and electrostatic interaction was evaluated by investigating the diffusion coefficient exhibited by gold nanoparticles in presence of sodium chloride (NaCl) ions in solution. The maximum concentration of NaCl in solution was evaluated by testing the aggregation of the nanoparticles in solution by performing an ultraviolet and visible (UV-Vis) absorption spectroscopy analysis. High concentrations of NaCl are known to promote the aggregation kinetics of nanoparticles in solution because of the reduction of the electrostatic repulsion acting between particles [75]. However, the UV-Vis spectroscopy analysis confirmed that the majority of nanoparticles in solution were monodispersed for concentration of NaCl up to 50 mM, hence this value was chosen as the maximum salt concentration for the single nanoparticle tracking analysis (Fig. 14).

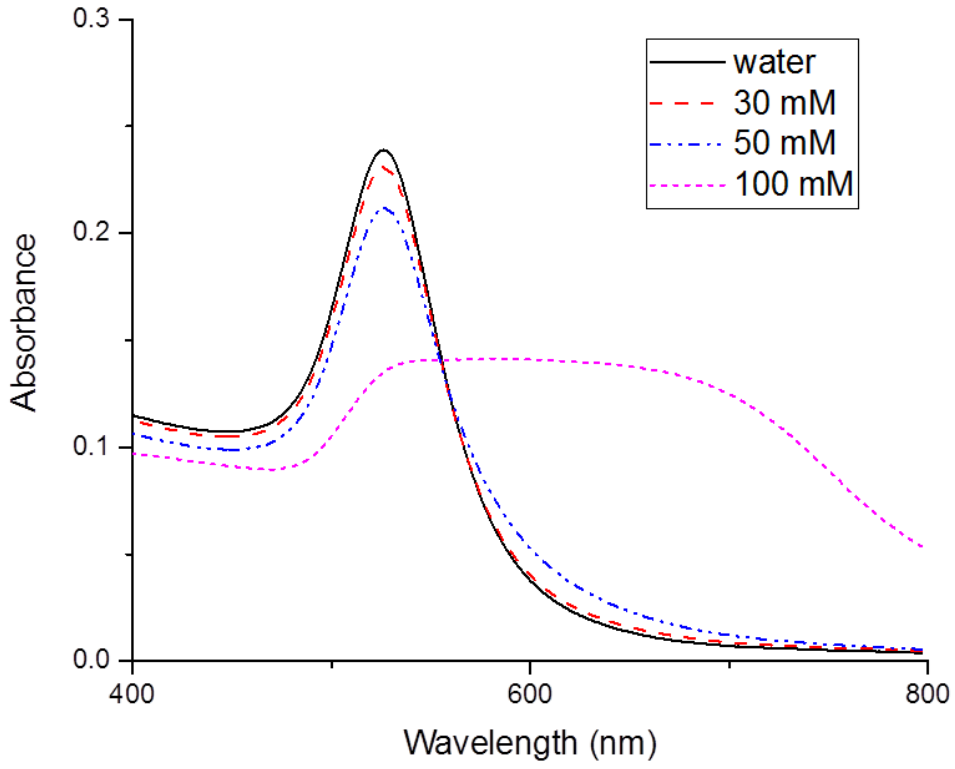

Figure 14: Absorption spectra of 50 nm gold nanoparticles (concentration 5 x 10^8 particles ml^{-1}) dispersed in NaCl solutions ranging from 0 to 100 mM.

This result is in-line with others reported in the literature for the same nanoparticles and salt species [76]. Moreover, the tracking method based on caustics can distinguish between single particles and clusters, allowing the tracking of only monodispersed particles in solution [36]. The values for the diffusion coefficient of 50 nm gold nanoparticles dispersed in NaCl solutions ranging from 0 to 50 mM are shown in Figure 15a.

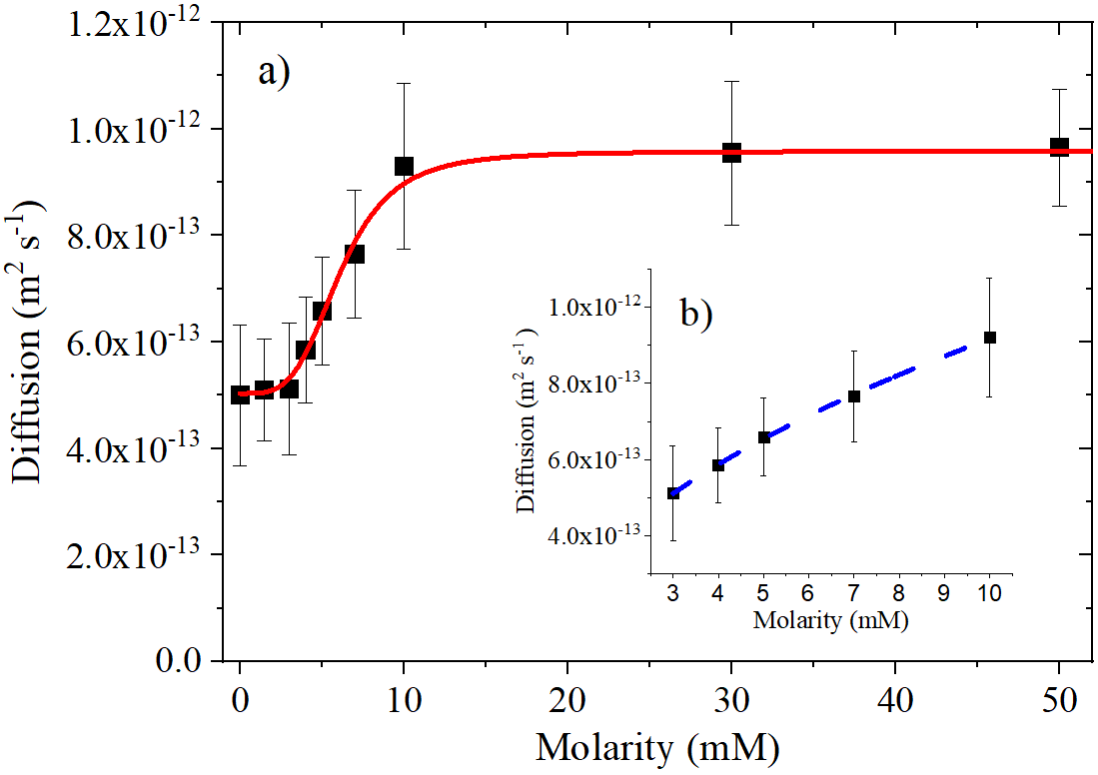

Figure 15: (a) Experimental diffusion coefficients for 50 nm diameter gold nanoparticles as a function of NaCl solution molarity fitted by Hill function (red continuous line); (b) Detail of the diffusion coefficient for 50 nm gold nanoparticle dispersed in solutions ranging from 3 mM to 10 mM of NaCl fitted by a square root function (blue dotted line).

There are no significant differences in the value of diffusion coefficient up to a salt concentration of 3 mM, suggesting that the ionic strength of the solution and the number of ions electrically bound to the nanoparticles' surface are not enough to influence the particle dynamics. The diffusion values exhibited by these solutions (approximately $5x10^{-13}$ m^2 s^{-1}) are in good agreement with the values found by Coglitore et al. for the diffusion of gold nanoparticles in deionised water [5]. At higher levels of NaCl concentrations there is an increase in the particle diffusion, which tends to the saturation value of 10^{-12} m^2 s^{-1}. The overall

trend of the diffusion coefficient as a function of the molarity of the solution can be effectively described by fitting the experimental data obtained with the Hill function, which has been widely used to describe experimental phenomena when the relationship between two sets of variables seems saturable and nonlinear [77]. In the experimental scenario, this dependence of the diffusion dynamics of the nanoparticles on the ionic content of the solution can be explained by considering the interaction between the surface of the nanoparticle and the free ions in solution. NaCl molecules dissociate in water into its respective cations and anions:

$$NaCl \longrightarrow Na^{+} + Cl^{-}$$

When the negatively charged nanoparticles are dispersed in the NaCl solution, Na^{+} ions start to surround the spherical surface of the particles, and the number of ions electrically bound to the surface will increase as a function of the molarity of the solution. The density of ions surrounding each particle controls directly the magnitude of the electrostatic interactions through variations in the Debye length, which is a measure of the electrical double layer thickness [78]. According to the DLVO theory, the dominant forces acting at the nanoscale between particles are the electrostatic forces and the Van der Waals forces [79]. These two forces are independent and opposite in action, i.e. electrostatic forces repel and Van der Waals forces attract particles, therefore they can be superimposed to obtain a good approximation of the net interaction force between two particles [80]. However, as the particle size and the distance between particles decreases, the non-additivity of the forces acting on the nanoparticles emerges. In other words, it becomes impossible to decompose the net interaction of forces acting between particles into separate additive contributions in order to understand the influence of each force independently from the others [81]. Hence, in this study, it was decided to investigate the changes in diffusion observed as a result of the action of Van der Walls and electrostatic forces together. At a low ionic strength, the Debye length is large because of the small concentration of counter ions surrounding the particle and the electrostatic

repulsion forces are dominant relative to Van der Waals attraction forces. A higher ionic strength causes a more effective shielding of the original charge of the particle and a reduction of the Debye length, leading to a decrease in the electrostatic repulsion forces. Hence, the net interaction force between particles becomes slightly attractive, because of the constant contribution of the Van der Waals forces which are insensitive to the ionic strength. Moreover, the resultant net attractive force causes the nanoparticles to be closer to each other, leading to an increased magnitude of the Van de Waals forces acting between particles, since they are distance dependent. The results demonstrate that these concurrent effects (reduction of electrostatic repulsion and increase of Van der Waals attraction) contribute actively to the nanoparticle diffusion process before aggregation occurs at higher salt molarity and that there is a direct correlation between the variation of the diffusion coefficient of the gold nanoparticles and the variation of the Debye length. Figure 15b shows the detail of the increase in the diffusion coefficient exhibited by the 50 nm gold nanoparticles dispersed in solutions with concentrations between 3 mM to 10 mM NaCl. It can be seen that the increased rate of the diffusion of the nanoparticles in this molarity range follows a square root trend, which is exactly the inverse of the trend in Debye length as illustrated in figure 16.

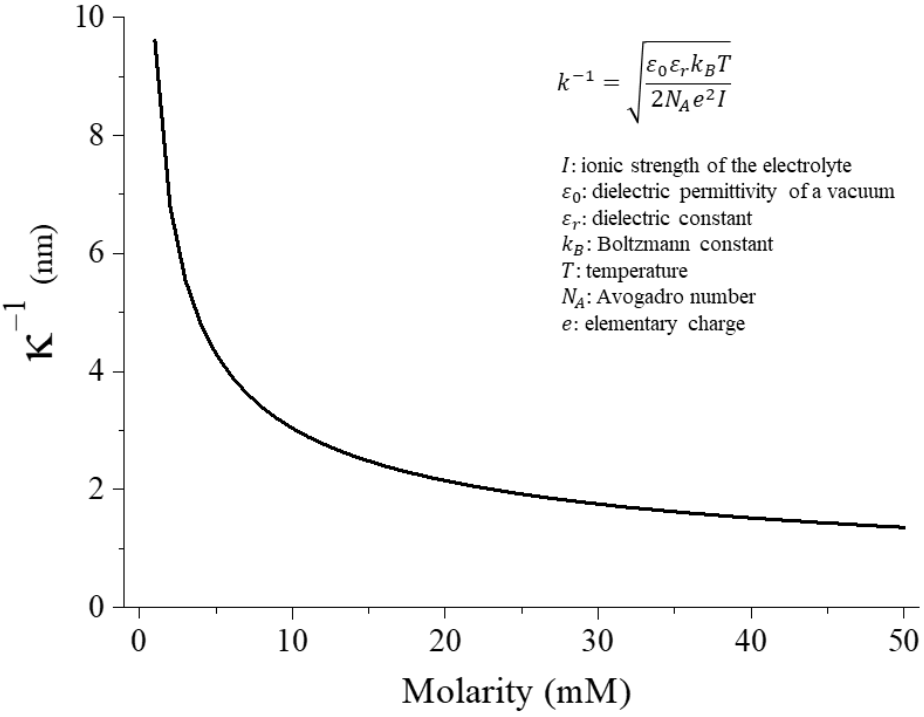

Figure 16: Debye length trend as a function of NaCl solution molarity calculated from its theoretical equation [75].

For concentrations between 0 and 10 mM NaCl, there is a significant reduction in the Debye length and hence electrostatic repulsion, leading to a noticeable increase in their diffusion through the medium. A further increase in the salt concentration (10 mM to 50 mM NaCl) causes an increasingly smaller reduction in the Debye length and the electrostatic repulsion forces, therefore the diffusion of the nanoparticles saturates and tends to a maximum value of approximately 10^{-12} m^2 s^{-1}.

The diffusion dynamics of 20 nm and 80 nm diameter gold nanoparticles dispersed in NaCl solutions was also evaluated and compared with the diffusion behaviour exhibited by the 50 nm diameter gold nanoparticles in figure 17.

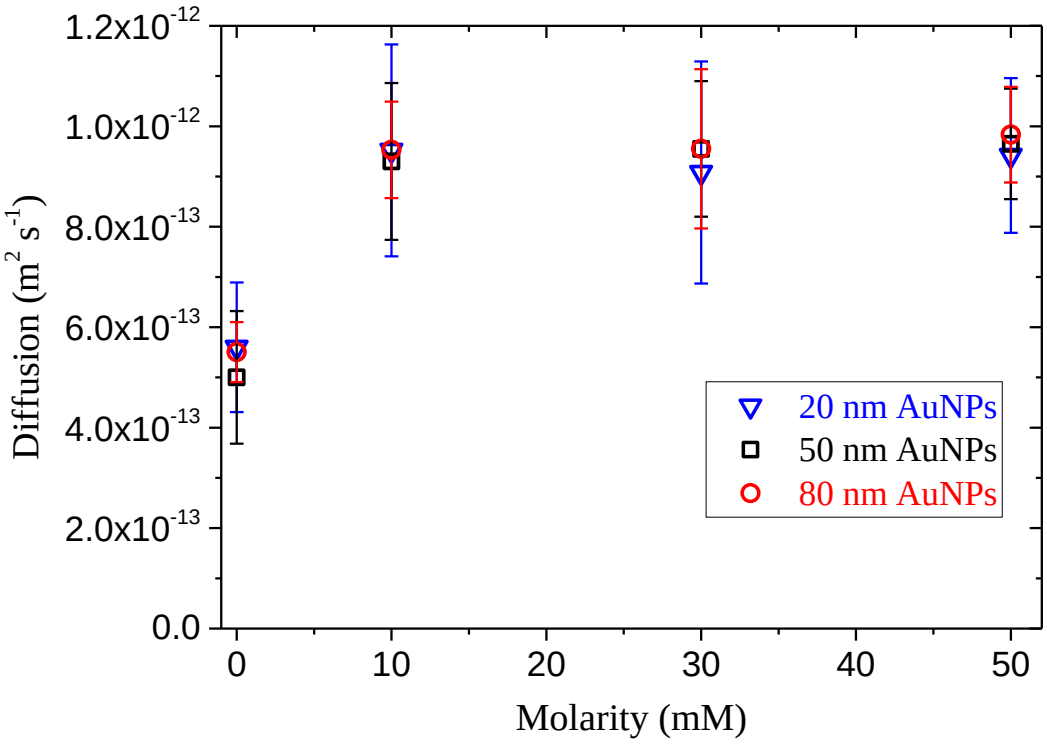

Figure 17: Experimental diffusion coefficients for 20 nm, 50 nm and 80 nm diameter gold nanoparticles as function of NaCl solution molarity.

Both the 20 nm, 50 nm and 80 nm diameter nanoparticles exhibit comparable initial (between 0 and 3 mM of NaCl) and final (between 10 and 50 mM of NaCl) diffusion coefficients, demonstrating that, under these test conditions, the diffusion of the nanoparticles was found to be independent of particle size. This result is consistent with the experiments performed by Coglitore et al. on gold and polystyrene nanoparticles at low concentrations in a simple fluid [5]. Moreover, this size-independence can be also related to the nature of the forces acting on the nanoparticles. Van der Waals and electrostatic forces both scale linearly with the particle radius, suggesting that an increase or decrease of particle size causes a comparable change to both these competing forces [82].

4.3. Settling dynamics of nanoparticles in simple and biological fluids

4.3.1. Effect of size on the settling dynamics of nanoparticles

The analysis of the dynamics of nanoparticles in solution was moved to the three-dimensional domain by investigating the settling dynamics of gold nanoparticles in solution. Figure 18 shows the effect of nanoparticle size on the concentration of nanoparticles settled and the relative time needed to reach equilibrium between the sedimentation and diffusion processes.

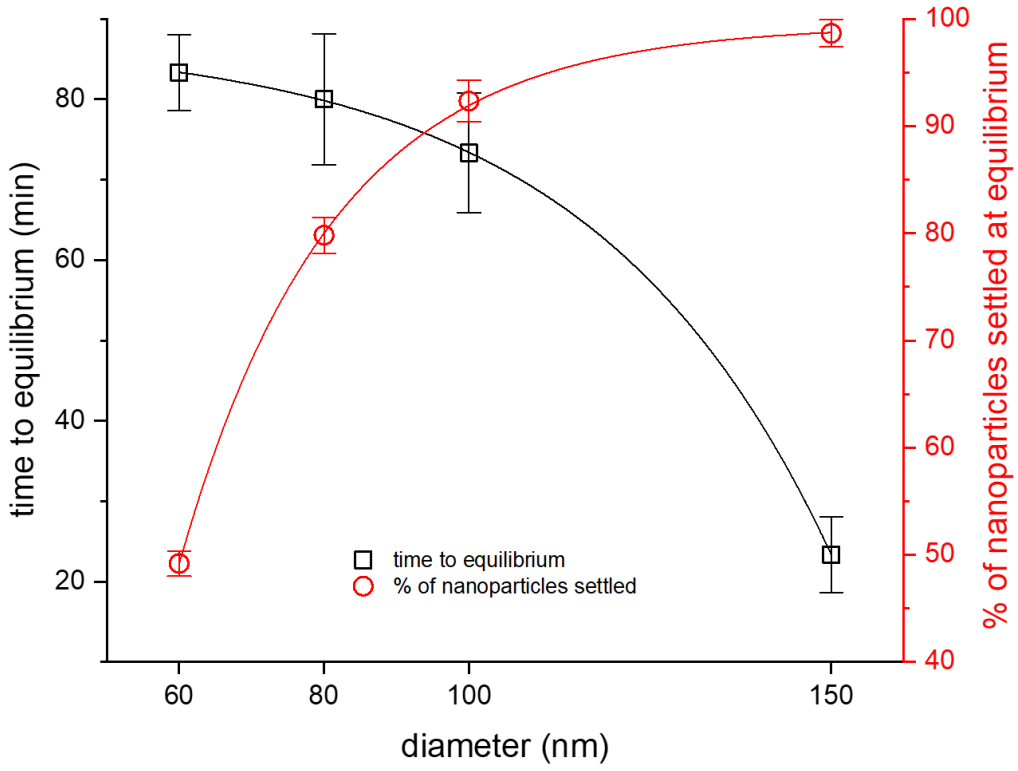

Figure 18: Experimental settling time (black squares and left axis) and percentage of nanoparticles settled at the equilibrium (red circles and right axis) as a function of nanoparticle diameter.

Larger particles tend to reach the equilibrium faster with a higher concentration of particles transported to the bottom of the solution, but all the particles tested exhibited a non-negligible deviation between the administered dose and the target dose at the equilibrium. Consider, for example, the smallest size tested, approximately 50% of the 60 nm nanoparticles in solution settled and migrated towards the bottom of the solution, meaning that the target dose was at

least 1.5x the initial administered dose. The reliability of the classical Mason–Weaver equation in describing the concentration profile of the nanoparticles in solution over time was assessed by plotting the concentration of not-settled nanoparticles together with the Mason-Weaver predictions (Fig. 19).

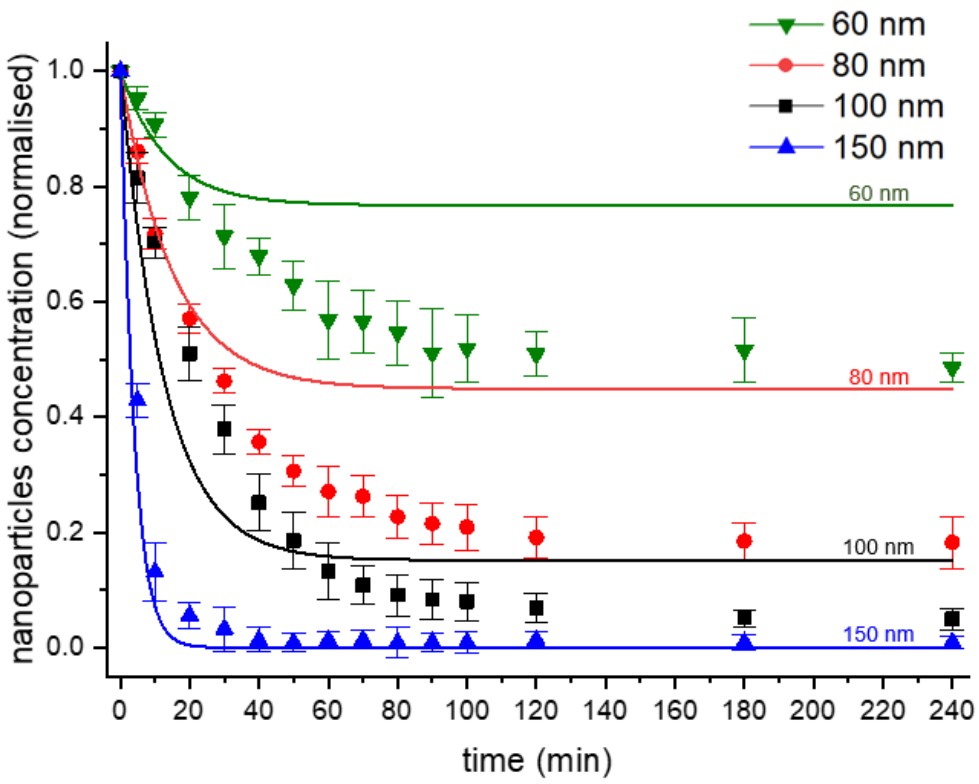

Figure 19: Measured concentration (symbols) of not-settled negatively-charged gold nanoparticles as a function of time in water at 23°C together with predictions (lines) from the Mason–Weaver model.

As expected, the Mason–Weaver equation, with the Stokes-Einstein diffusion coefficient and Stokes sedimentation velocity, is not able to accurately predict the experimental results. The theoretical upward diffusion flux, which opposes the downward sedimentation flux of nanoparticles, is higher than the experimental one, leading to an overestimation of the concentration of the nanoparticles not settled once equilibrium is attained. The main factor affecting the diffusion flux in the Mason–Weaver equation is the diffusion coefficient evaluated using the Stokes – Einstein equation, already proven to overestimate the diffusion coefficient for nanoparticles in simple fluid at our experimental concentration [5]. Another

limitation of the model is the assumption that the sedimentation velocity and diffusion coefficient exhibited by the particles in solution is constant with time, without taking into account that the concentration gradient formed once equilibrium is achieved can directly affect the sedimentation and diffusion behaviour of the nanoparticles. Ganguly and Chakraborty [83] demonstrated that the sedimentation velocity decreases as a function of the concentration because of the increased magnitude of the hydrodynamic interactions between particles. Kourki and Famili [84] observed the same decreasing trend of sedimentation velocity when investigating the sedimentation of silica nanoparticles. Coglitore et al. [5] explained the low values of diffusion coefficient obtained from experiments by considering that, at low concentrations, nanoparticle motion is almost entirely controlled by the diffusive regime of the fluid molecules and the particle-particle interaction can be neglected. An extensive number of studies have demonstrated that the diffusion of fluid molecules, such as water, does not satisfy the assumptions underlying the Stokes – Einstein relationship and is better described by a fractional relationship [15, 85]. On the other hand, Koening et al. [86] reported a higher diffusion coefficient (of the same order of magnitude as the Stokes – Einstein prediction) using the same nanoparticles and solution but with a higher particle concentration. Holmberg et al. found using a dynamic light scattering technique that the diffusion coefficient of titanium dioxide nanoparticles is dependent on the mass concentration of particles in solution [6]. Considering this evidence, it is reasonable to conclude that the concentration of nanoparticles directly affects their diffusion and sedimentation behaviour through particle-particle interactions. In this test scenario, at the beginning of the experiment, nanoparticles are homogeneously monodispersed at low concentrations, so that particle-particle interactions are negligible and do not affect the sedimentation velocity while the diffusion coefficient is smaller than the theoretical one and mainly regulated by the fluid molecules. Once a concentration gradient forms in the solution, particle interactions start to influence the dynamics of the

nanoparticles above the settling zone, leading to a decrease in sedimentation velocity and an increase in the diffusion coefficient. Another factor to take into account is the viscosity of the medium which can potentially influence both the diffusion and sedimentation behaviour of nanoparticles. However, experimental and theoretical observations have demonstrated that the presence of nanoparticles at low concentrations does not significantly affect the viscosity of the fluid [5].

A modified Mason–Weaver theoretical model has been developed to overcome the limitations of the classical Mason–Weaver equation, taking into account the experimental evidence and physical hypotheses discussed above. The distinctive feature of the model proposed in this study is the dependence of the diffusion coefficient on the local concentration of the nanoparticles:

$$\frac{\partial n(z,t)}{\partial t} = \frac{\partial}{\partial z}\left(D(n(z,t))\frac{\partial n(z,t)}{\partial z}\right) - V\frac{\partial n(z,t)}{\partial z} \tag{10}$$

where $D(n)$ is the diffusion coefficient as a function of the normalised local concentration of the nanoparticles n:

$$D(n) = D_{exp} + \frac{\left(D_{StEin} - D_{exp}\right)n^k}{n_{50}^k + n^k} \tag{11}$$

where D_{exp} = 5 x 10^{-13} m^2 s^{-1} is the experimental value of the diffusion coefficient measured at a low concentration of nanoparticles in solution at 23°C and D_{StEin} is the diffusion coefficient according to Stokes – Einstein equation [12]. The transition between the diffusion coefficient at low concentrations and the value from the Stokes – Einstein relationship is regulated by the experimental fitting parameters n_{50} = 1.5 and k = 30, representing the normalised nanoparticle relative concentration at which the transition happens and the slope of the transition respectively. The modified version of the Mason – Weaver equation is used in this thesis to theoretically predict only the settling dynamics of nanoparticles in solutions at 23°C because

of the lack of data concerning the experimental diffusion coefficient exhibited by nanoparticles in solution at higher temperatures.

The appendix contains all the details about the derivation of equation 10 from equation 7 assuming the diffusion coefficient is a function of the local concentration of the particles.

The modified version of the model is able to predict the experimental data more accurately than the classical Mason–Weaver model and can be used to simulate the settling dynamics and estimate the nanoparticle concentration over time (Fig. 20).

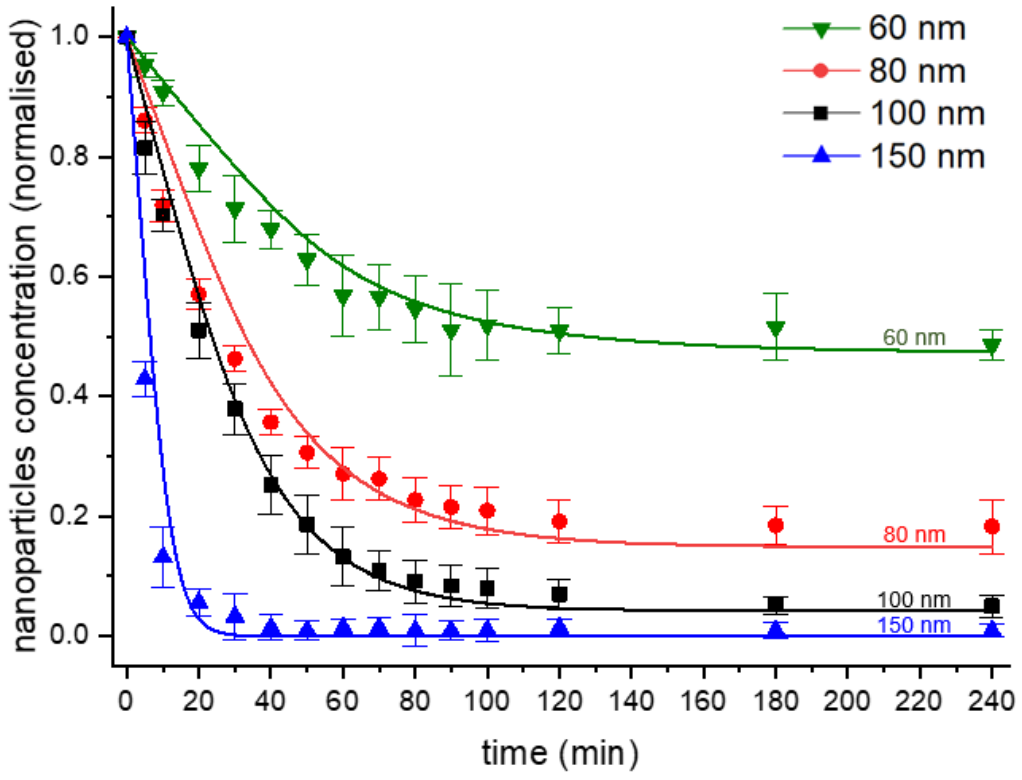

Figure 20: Measured concentration (symbols) of not-settled negatively-charged gold nanoparticles as a function of time in water at 23°C together with predictions (lines) from the proposed modified Mason–Weaver model.

The comparison between the accuracy of the classical and modified Mason-Weaver model demonstrates that the ability of the two models in predicting experimental data diverges as the size of the particles decreases (Fig. 21).

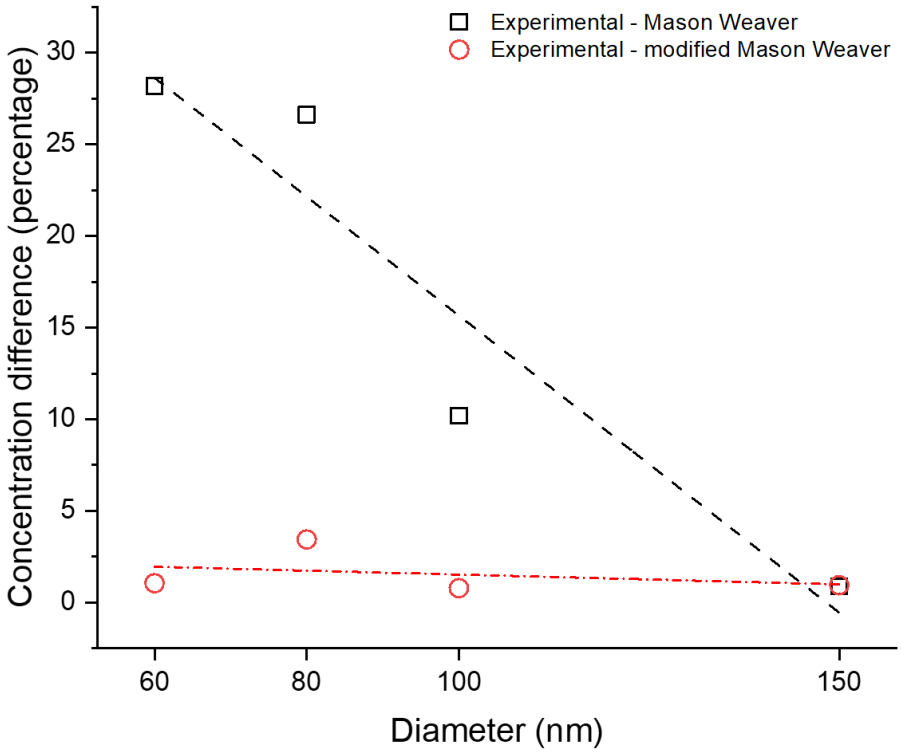

Figure 21: Difference between the concentration of not-settled nanoparticles at equilibrium as measured experimentally and calculated with the original and modified version of the Mason – Weaver equation.

For the 60 nm nanoparticles, the Mason – Weaver classical model overestimates the concentration of the nanoparticles not settled by about 30% with respect to the experimental data, while the modified version of the model has an error of less than 5% in predicting the same quantity. On the other hand, at the maximum particle size tested, the performance of the two models is comparable. This evidence further supports the hypothesis about the role of the diffusion of nanoparticles in driving their settling dynamics. As the size of nanoparticles increases, the experimental diffusion coefficient has been found to be progressively better approximated by the Stokes-Einstein equation even at low concentrations [5]. Moreover, as the size of the nanoparticles increases, the sedimentation dynamics becomes the dominant factor regulating the overall dynamics, making the contribution from diffusion negligible.

4.3.2. The role of colloidal stability on the settling dynamics of nanoparticles

The effect of temperature on the settling dynamics was evaluated by testing 100 nm diameter negatively-charged gold nanoparticles in water at 23 °C and at the biologically-relevant temperature of 37 °C (Fig. 22a).

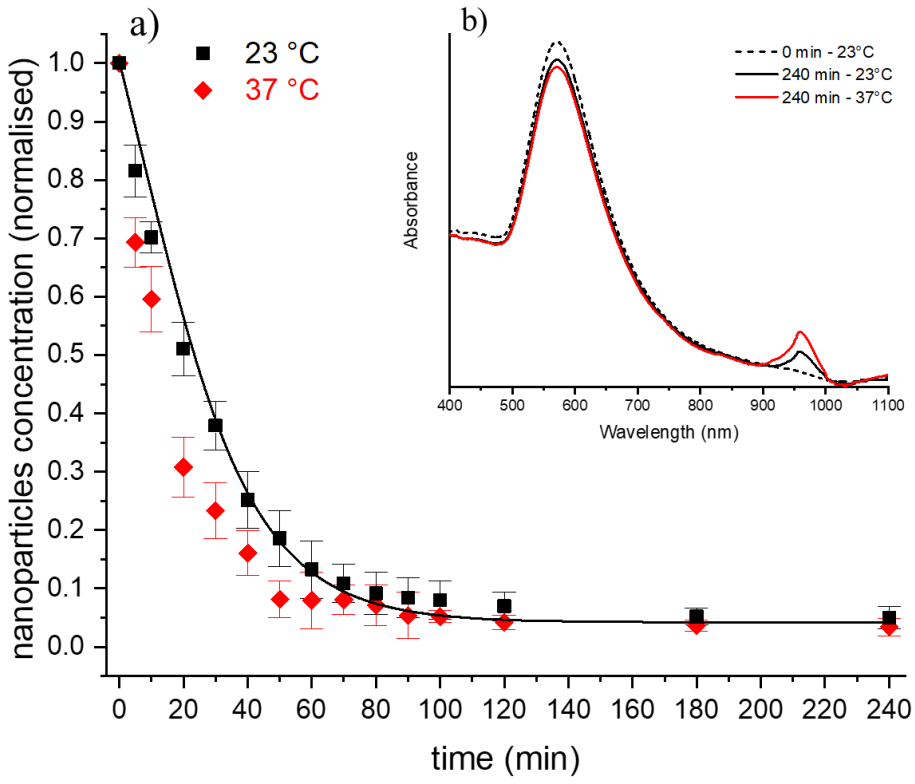

Figure 22: (a) Concentration of not-settled negatively-charged 100 nm diameter gold nanoparticles in water at 23°C (black squares) and 37°C (red rhombus) over time together with predictions (lines) from the proposed modified Mason–Weaver model, and inset (b) UV-Visible absorption spectra of nanoparticle solutions at the beginning of the experiment (blue line) and after 240 minutes for solutions kept at 23°C (black line) and at 37°C (red line).

The results obtained demonstrate that at 37 °C the sedimentation velocity increased and that the solution reached the sedimentation–diffusion equilibrium 30 minutes before the same solution at 23°C. The higher temperature directly influences the aggregation kinetics of gold nanoparticles, enhancing their aggregation rate in solution [87]. Colloidal stability has been reported as one of the primary factors affecting the sedimentation–diffusion equilibrium of the

nanoparticles [88]. The UV-Visible spectra of the solutions kept at constant temperatures of 23°C and 37°C confirmed the increase in the aggregation and sedimentation rate of nanoparticles in solution with temperature (Fig. 22b). At higher temperatures aggregates of particles form at an increased rate and sediment faster than monodispersed nanoparticles in solution due to their larger mass. The nanoparticle solution kept at 37 °C exhibited a more evident depletion of the primary absorbance peak and a higher secondary absorbance peak when compared with the same solution kept at 23°C. The depletion of the primary absorbance peak has been extensively reported as an indication of the reduced number of monodispersed nanoparticles in solution [89-90]. The depletion is caused by the particles and agglomerates precipitating to the bottom of the solution, outside of the scanning range of the spectrophotometer laser. The secondary absorption peak is likely to have been generated by clusters of nanoparticles formed in the solution and not yet part of the sediment. At the early stage of the aggregation process, nanoparticles have been reported to aggregate and assemble into specific structures, like dimers, trimers tetramers, etc. [87]. Hence, these early-stage aggregation structures are likely to scatter light at longer wavelengths until they become part of the sediment at the bottom of the solution. Gold nanoparticles with ill-defined spherical geometry (like rods and stars) have been reported to exhibit their main absorption peak at wavelengths comparable with the wavelengths of our secondary absorption peak [91-92].

The comparison between the sedimentation–diffusion behaviour of oppositely charged 100 nm gold nanoparticles in water at 23°C is shown in figure 23.

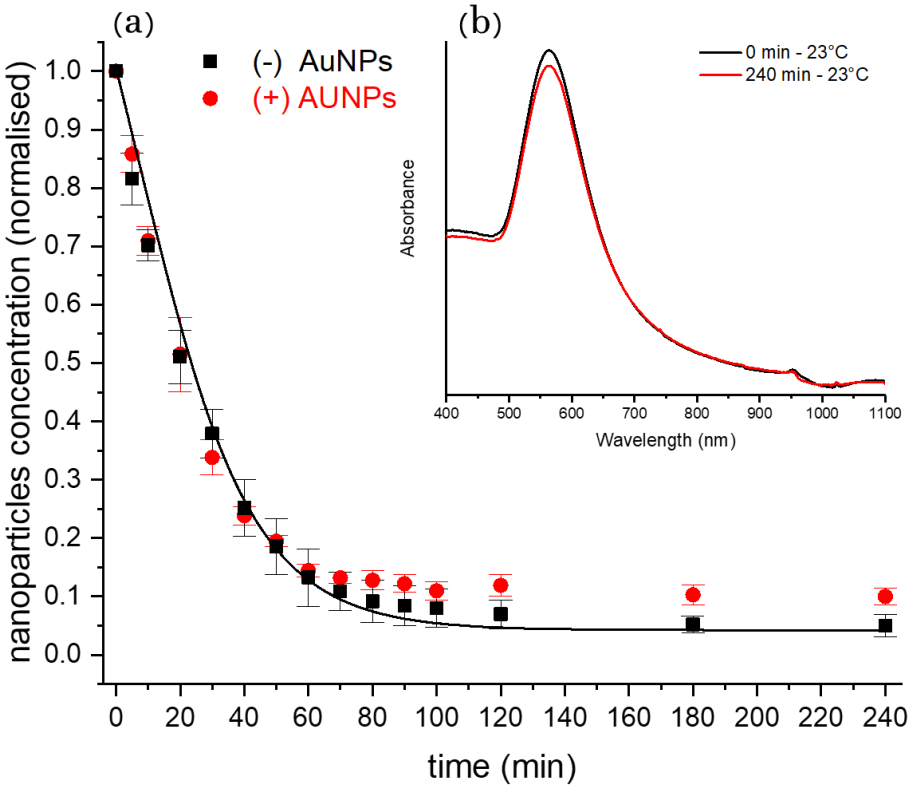

Figure 23: (a) Concentration of not-settled negatively charged (black squares) and positively-charged (red circles) 100 nm diameter gold nanoparticles in water at 23°C together with predictions (lines) from the proposed modified Mason–Weaver model, and inset (b) UV-Visible absorption spectra of positively-charged nanoparticle solutions at the beginning of the experiment (black line) and after 240 minutes for solutions kept at 23°C (red line).

There is no apparent difference between the sedimentation rate exhibited by these two types of nanoparticles; but positively charged nanoparticles exhibit a higher concentration of not settled particles with respect to their negatively charged counterparts at equilibrium. This behaviour can be explained by considering the colloidal stability of the positively charged nanoparticles solution used in this investigation. The UV-Visible analysis (Fig. 23b) confirmed the presence of fewer aggregates in solution at 23°C after 4h when compared to the solution of negatively charged nanoparticles kept at the same temperature for the same time (i.e. no secondary absorption peak at longer wavelengths). Hence, more monodispersed particles are free to diffuse back into the solution from the sediment leading to a higher concentration of not settled nanoparticles at equilibrium.

4.3.3. The settling dynamics of nanoparticles in biological solution

To characterise nanoparticle behaviour in biologically-relevant solutions, the dynamics of sedimentation–diffusion equilibrium has been investigated by dispersing 100 nm diameter negatively-charged gold nanoparticles in Dulbecco's Modified Eagle Medium (DMEM) with 10% Fetal Bovine Serum (FBS). This solution was chosen because it is commonly used to support the growth of a range of mammalian cells and to understand the concentration of nanoparticles delivered at the cellular level.

Figure 24 shows the absence of significant deviations between the settling dynamics of nanoparticles in DMEM with 10%FBS and in water at 23°C and 37°C. This outcome can be explained considering the main factors affecting the settling behaviour of nanoparticles, namely the inter-particle interactions, the colloidal stability, and the viscosity. A protein corona formed on the surface of the particles dispersed in the biological medium prevented nanoparticle aggregation that would otherwise be induced by the high content of salts in solution and the temperature [76]. The zeta potentials of the particles in the two solutions are similar [93-94], meaning that the electrostatic interactions have comparable magnitudes and result in no observable differences in the sedimentation profile. Finally, the dynamic viscosity of DMEM with 10%FBS has been reported to be only 5% higher than the dynamic viscosity of pure water [95], which is not enough to have a significant impact on nanoparticle kinetics [5].

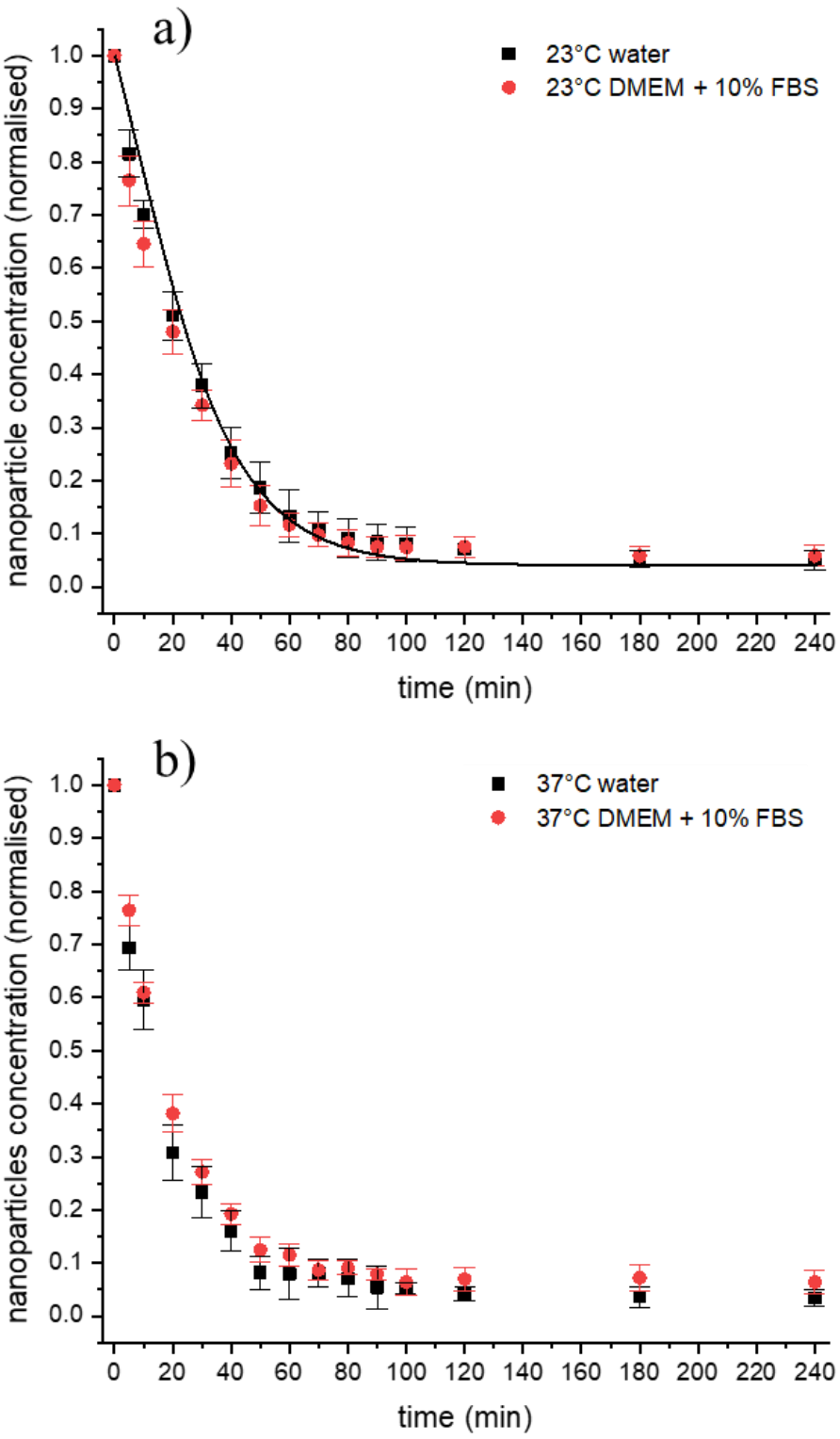

Figure 24: (a) Concentration of not-settled negatively-charged 100 nm diameter gold nanoparticles in water (black squares) and in DMEM+10%FBS (red circle) as functions of time at 23°C together with predictions (lines) from the proposed modified Mason–Weaver model and (b) concentration of the same nanoparticles dispersed in the same solutions at 37°C.

4.4. Limitations of nanoparticles size characterization by Asymmetric Flow Field-Flow Fractionation coupled with online Dynamic Light Scattering

The dependence of the diffusion process on the local concentration of the particles in solution has a direct implication when exploring the limitations of the Asymmetric flow field-flow fractionation technique coupled with online UV-visible spectrophotometer (UV-Vis) and dynamic light scattering (DLS) for characterising gold nanoparticles of a known size of 40 nm at a different initial working concentration. The DLS size measurements of the solution of nanoparticles eluted by the AF4 as a function of the elution time along with the relative coefficients of variation at the various stages of the elution process are shown in figure 25. At the higher initial concentration of 10^{11} particles ml^{-1}, the AF4-DLS-UV system provides an accurate sizing of the nanoparticles in suspension returning an average diameter close to the nominal one with low coefficients of variation throughout all the zones identified in the absorbance distribution curves. The apparent size increase at the beginning and at the end of the absorbance curve start to appear for an initial working concentration of 10^{10} particles ml^{-1} and becomes progressively more evident as the initial working concentration of the particles in suspension is decreased. At the lowest concentration tested of 10^{9} particles ml^{-1}, the DLS returns a noticeable U-shaped distribution for the diameters as a function of the elution time and detects an increase in the size of the particles of at least 50% with respect with to the nominal size of the particles, even in the region associated with the maximum concentration of particles passing through the size detector, i.e. zone 2.

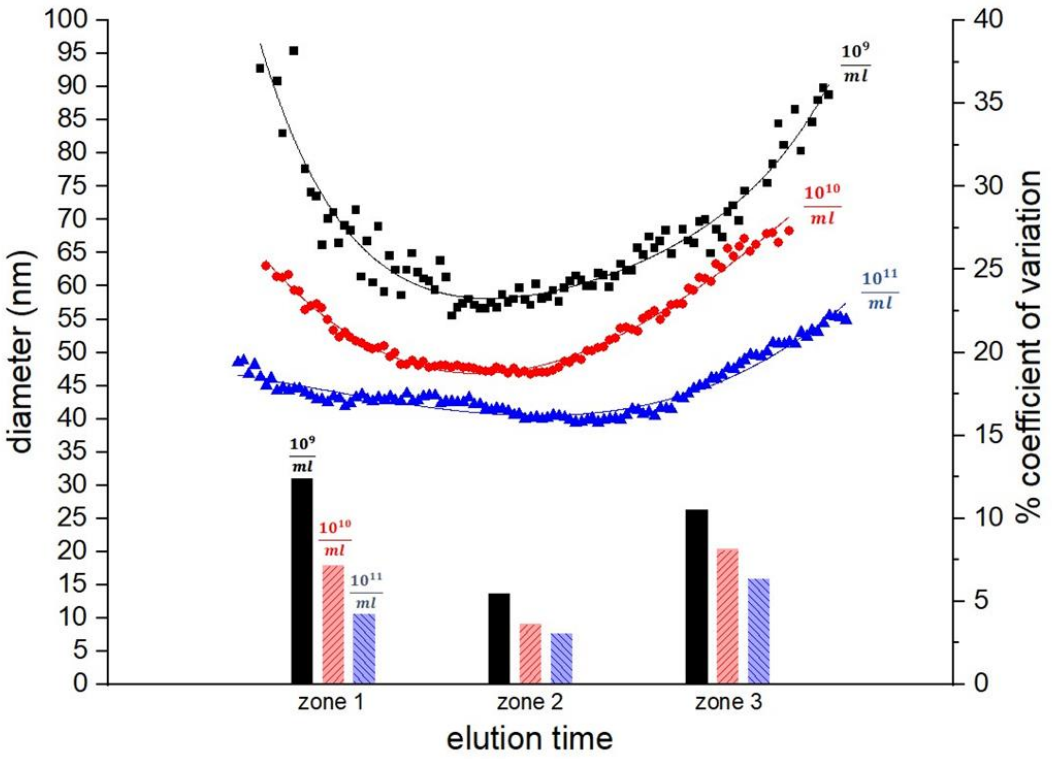

Figure 25: Detected diameters of 40 nm gold nanoparticles (data points and left axis) in suspension at different concentrations as a function of the elution time and coefficient of variation (columns and right axis) for the three absorbance zones identified based on results from AF4-DLS-UV system.

The dependence of the coefficient of variation on the concentration of particles provides further confirmation of the sizing inaccuracy of the AF4-DLS-UV system, both for suspensions at low initial concentrations and for suspensions at the beginning and end of the elution process. The coefficient of variation quantifies the variability of a set of data by evaluating the level of dispersion of a given set of measurements around the mean. A high coefficient of variation indicates low reliability and stability of the measurements [96]. In this test scenario, the high coefficients of variation exhibited particularly at the beginning and end of the elution process by suspensions with particle concentrations up to 10^{10} particles ml^{-1} provides evidence of the failure of the AF4-DLS-UV system to yield an accurate size characterisation for the population of particles in suspension. Similar results can be observed analysing the measurements provided by the AF4-DLS-UV system for the suspensions of 60 nm gold nanoparticles investigated (Fig. 26). Again, the suspension at the lowest initial concentration of 10^9 particles

ml $^{-1}$ exhibits a more obvious U-shaped distribution for the diameters and the highest coefficient of variation in all the regions of absorbance. For suspensions in this concentration range, the average diameter detected by the DLS is at least 35% higher than the nominal diameter of nanoparticles in suspension.

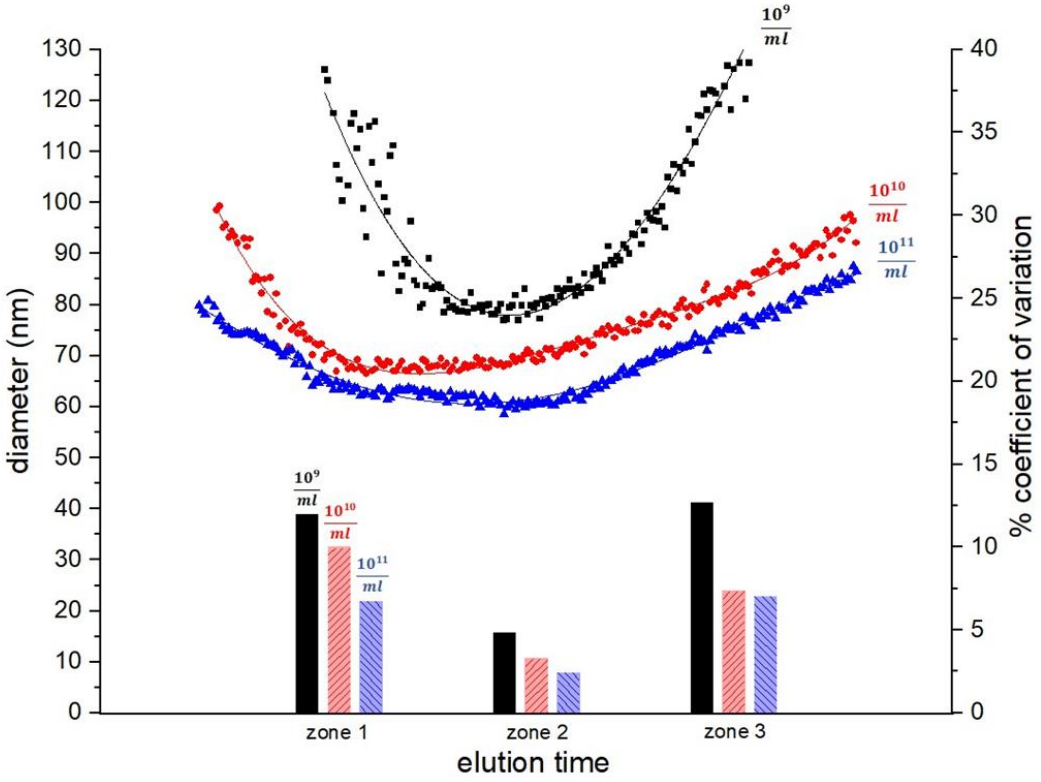

Figure 26: Detected diameters of 60 nm gold nanoparticles (data points and left axis) in suspension at different concentrations as a function of the elution time and coefficient of variation (columns and right axis) for the three absorbance zones identified based on results from AF4-DLS-UV system.

The concentration–dependence of the sizing ability of the AF4-DLS-UV system demonstrated in this study provides further support to the diffusion dynamics-concentration relationship found in these investigations and by others in the literature [5-6]. At the beginning and at the end of the elution process, the concentration of particles in suspension was progressively lower, thus the nanoparticles were likely to exhibit a progressively slower diffusion behaviour transitioning from the Stokes - Einstein diffusion regime to the experimental slow diffusion regime exhibited by nanoparticles at low concentration [5]. The DLS (being based on the

Stokes-Einstein equation) misinterprets the progressive decrease of the diffusion coefficient as a result of a progressive increase in the size of nanoparticles in suspension, returning a U-shaped curve for the diameter as a function of the concentration of particles. The phenomenon is further promoted by decreasing the initial concentration of the nanoparticles injected into the system. This hypothesis has been confirmed by the Disk Centrifugal Liquid Sedimentation (disk-CLS) analysis performed on the same suspension of nanoparticles. In a disk-CLS analysis, the diffusion behaviour of nanoparticles is not taken into account and the Stokes diameter of particles in suspension is derived from the Stokes sedimentation law. In brief, the disc-CLS consists of a rotating disc filled with a liquid density gradient. The gradient typically consists of a water–sucrose solution of varying sucrose concentrations. The suspension of particles is injected in the centre of the disc. If the density of the particles exceeds the density of the gradient, then the rotational motion of the disk causes the particles to move through the liquid density gradient toward the edge of the disc, where their transit is detected by a photodetector. Depending on their size and density, particles reach the detector at different times. The relationship between the particle's Stokes diameter and the time for the particle to reach the detector is given by the Stokes equation [97].

Figure 27 shows that this analysis provided more consistent results between suspensions at different concentrations of particles, demonstrating the negligible influence of the concentration of particles on the sizing ability of the disk-CLS both for 40 nm and 60 nm suspensions, thus demonstrating the theoretical limitations of a DLS-based analysis.

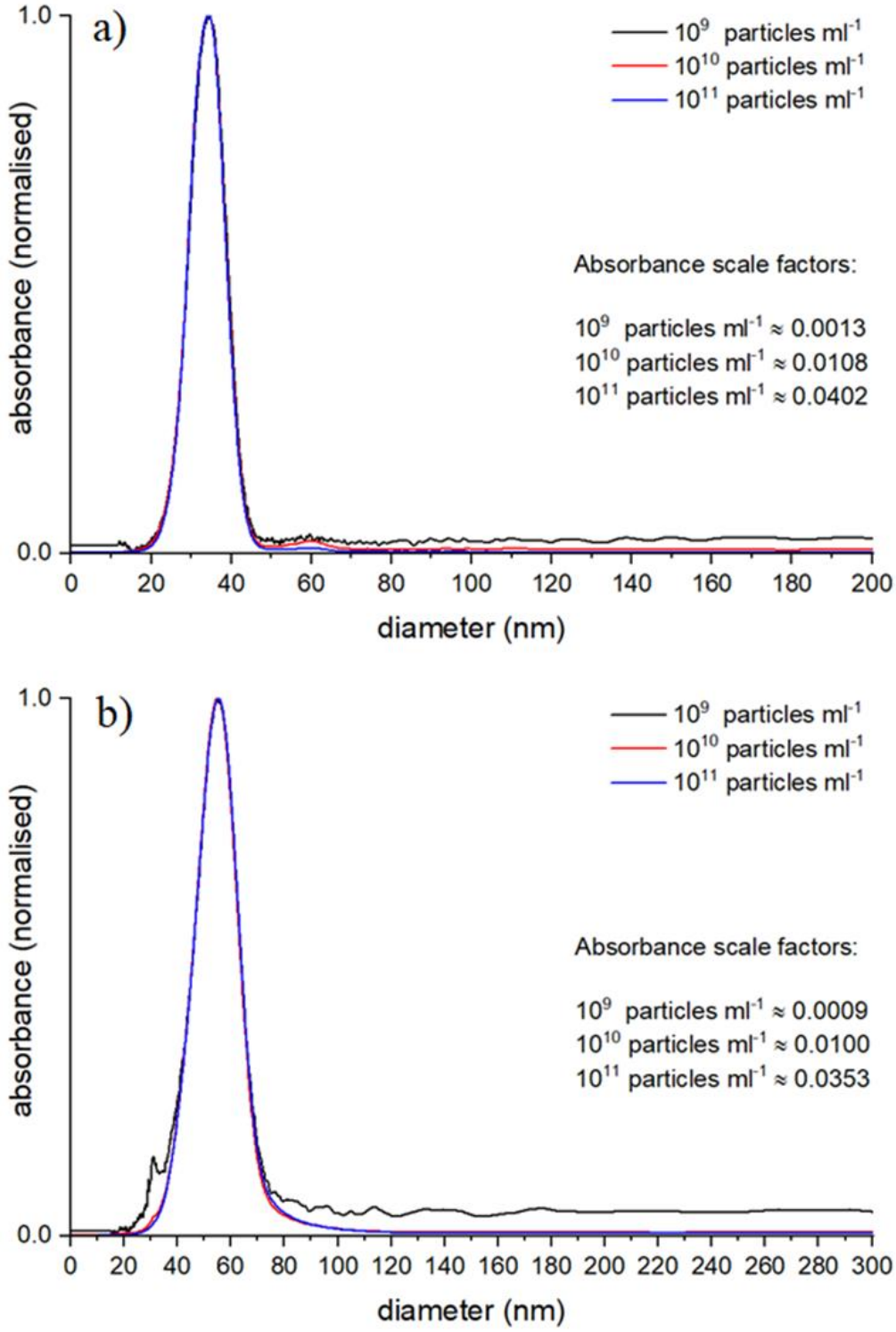

Figure 27: Disk-CLS particle size distributions for the (a) 40 nm and (b) 60 nm suspensions of gold nanoparticles at different concentrations. The absorbance values have been normalised dividing the original values by the relative scale factors shown inset.

4.5. Bacteria dynamics and interactions with surfaces

The mechanisms of bacterial adhesion and biofilm formation have been investigated by characterising the dynamics of bacteria interacting with a surface. Standard glass controls and proven anti-microbial benzalkonium chloride (BKC) surfaces were used to investigate the range of bacteria-surface interactions. Once a bacterium approaches a surface, the preliminary interaction is mainly regulated by electrostatic and hydrodynamic interactions. In this experimental scenario, both the bacteria and glass carry a negative surface charge. The outer membrane of *Escherichia coli* is negatively charged due to the dissociation of carboxyl and phosphate groups in the peptidoglycan and lipopolysaccharides of cell walls [98], while glass is known to acquire a negative charge in contact with aqueous solutions, mainly because of the dissociation of the silanol groups [99]:

$$SiOH \longrightarrow SIO^{-} + H^{+}$$

The resultant repulsive electrostatic force generated by the interaction between the bacteria and the surface contrasts with the initial attachment and compels the bacteria to randomly diffuse above the surface (Fig. 28a). However, because of the other forces involved (such as Van der Waals attractive forces and gravitational forces), bacteria can overcome the electrostatic repulsion and attach to the surface. Depending on the surface area of the membrane attached to the surface and the resulting dynamics of the bacteria, it is possible to distinguish two types of attachment: rotary attachment, when just one extremity of the bacterium adheres to the surface and the bacterium exhibits a rotatory motion around the attached pole (Fig. 28b); and lateral attachment, when the bacterium adheres to the surface for a portion of its length and the bacterium exhibits a translation or sliding (Fig. 28c).

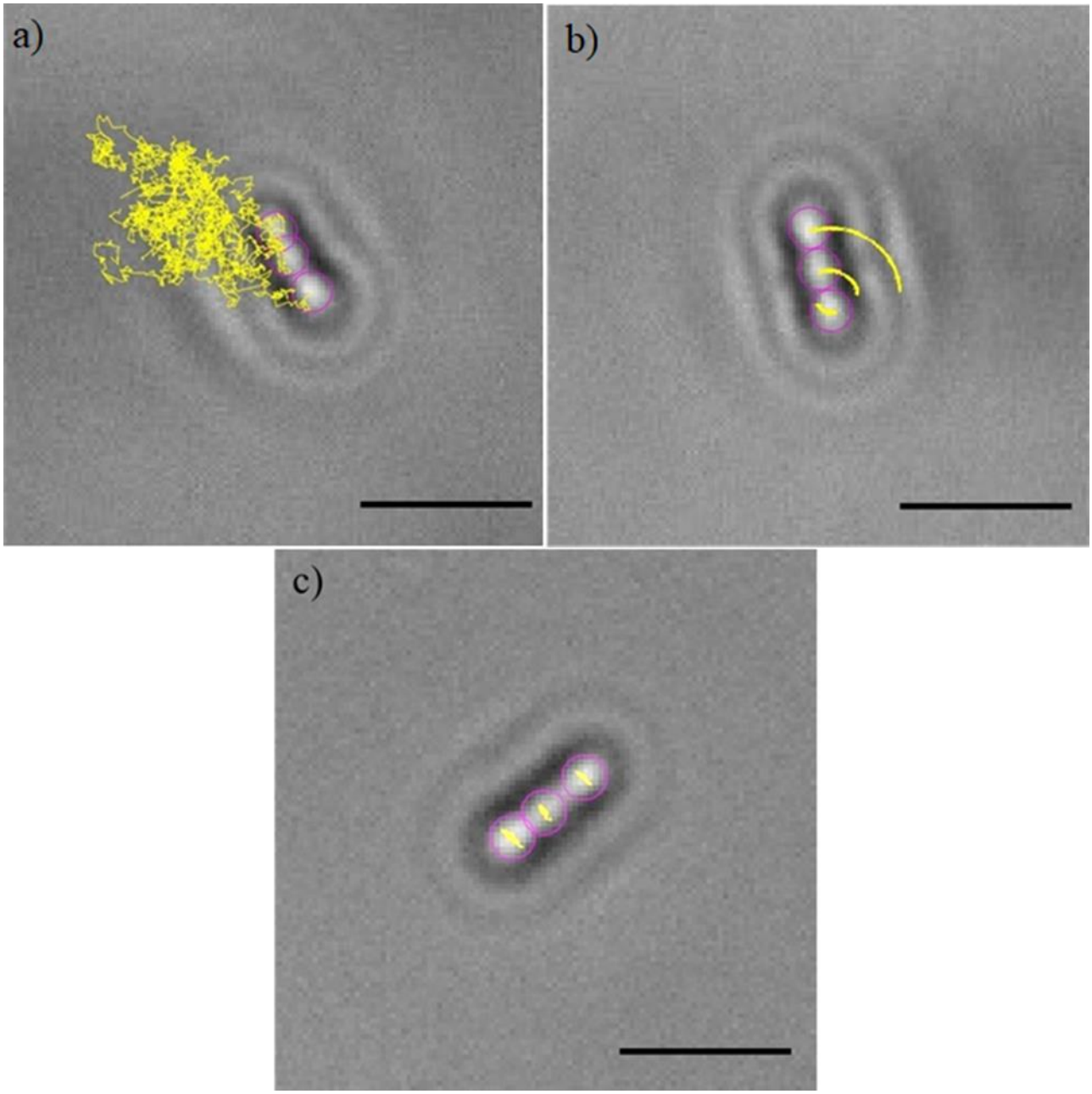

Figure 28: Tracks (yellow lines) of the three sections (purple circles) of bacteria experiencing: a) random diffusion above the surface; b) rotary attachment; c) lateral attachment. The dynamics of the three bacteria has been monitored for approximately 20s. The length of the scale bars is 5 μm.

The same interaction dynamics was observed in bacteria dispersed both in LB and PBS (Fig. S1-S4 in the electronic supplementary material). These types of attachment have been recently investigated experimentally using brightfield microscopy by Agladze et al, in an effort to characterise the reversible and irreversible attachment of *Escherichia coli* bacteria. The authors concluded that lateral attachment is irreversible and that bacteria experiencing this specific

adhesion do not exhibit any movement [100]. However, the results demonstrate that the initial attachment is reversible even when it is lateral. Depending on the forces acting on the bacteria, the type of attachment can change from rotary to lateral and vice versa (Fig. S5-S10 in the electronic supplementary material). Hence, because of the variety of forces and interactions involved, the distinction between irreversible and reversible attachment should be made not on the basis of the surface area adhered but by considering the timescale of the interaction [101]. In this study, it was observed that even bacteria laterally attached to the surface were not stationary and were not simply adhered statically to the surface but exhibited a sliding movement along the surface. At this stage, bacteria are reported to start secreting extracellular polymeric substances (EPS) [47]. The EPS layer, along with the attractive Van der Waal forces and membrane pili, strengthened the adhesion and expanded the surface around a bacterium which was influenced by its presence, and acted as a nutrient trap facilitating the attachment of other bacteria. After as little as 2 hours, two or more bacteria aligned and interacted with each other, marking the starting point of the formation of a two-dimensional colony or the first stage of a biofilm. Bacteria aligned in a semi-ordered way, trying to minimise the space separating them and increasing the contact surface between them (Fig. 29).

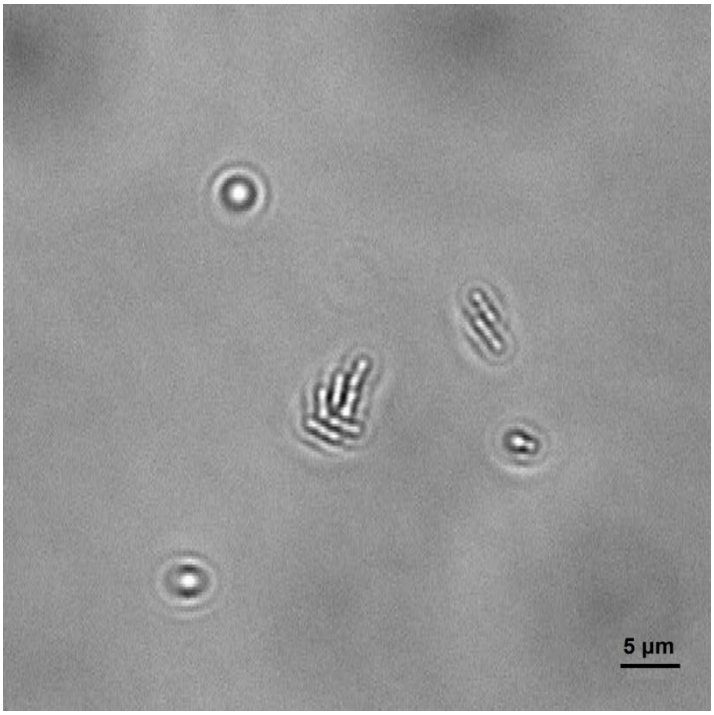

Figure 29: Escherichia coli bacteria gathering together to start biofilms.

After 24h, the concentration of bacteria and the size of the biofilm colonies increased proportionally to the amount of nutrients in solution (Fig. 30).

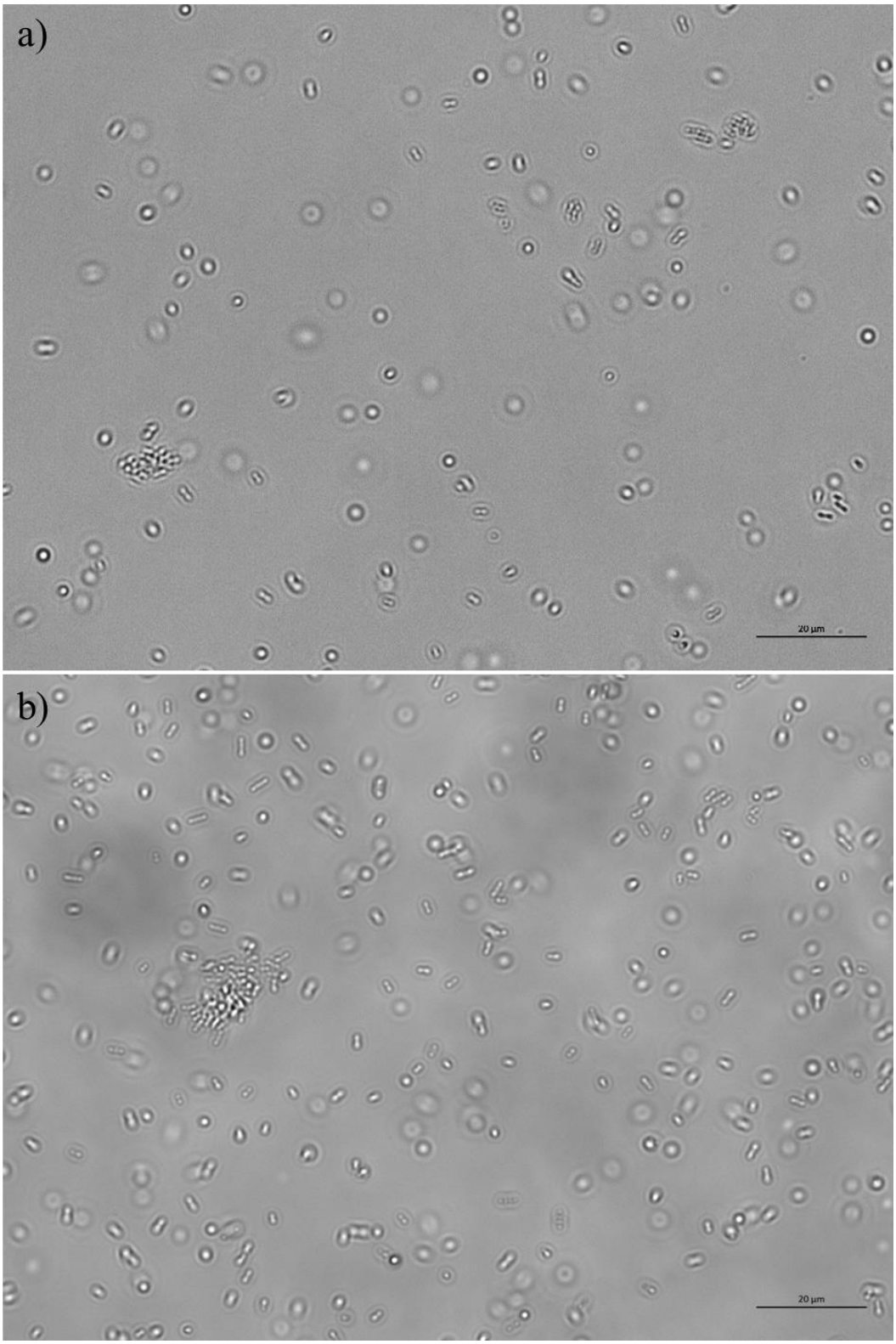

Figure 30: Population of Escherichia coli bacteria dispersed in a) PBS and b) 10% LB in PBS exposed to a glass surface for 24h.

was noticeable that even when a three-dimensional colony developed, it was still possible to recognise the dynamics of the system (Fig. S11-13 in the electronic supplementary material).

In fact, even at this stage of the formation of the biofilm, the bacteria were not static but continued to dynamically interact with the surface and each other. In contrast, bacteria entering into contact with the glass surface coated with BKC just adhered statically to the surface, resulting in the absence of any noticeable dynamics over time. (Fig. 31).

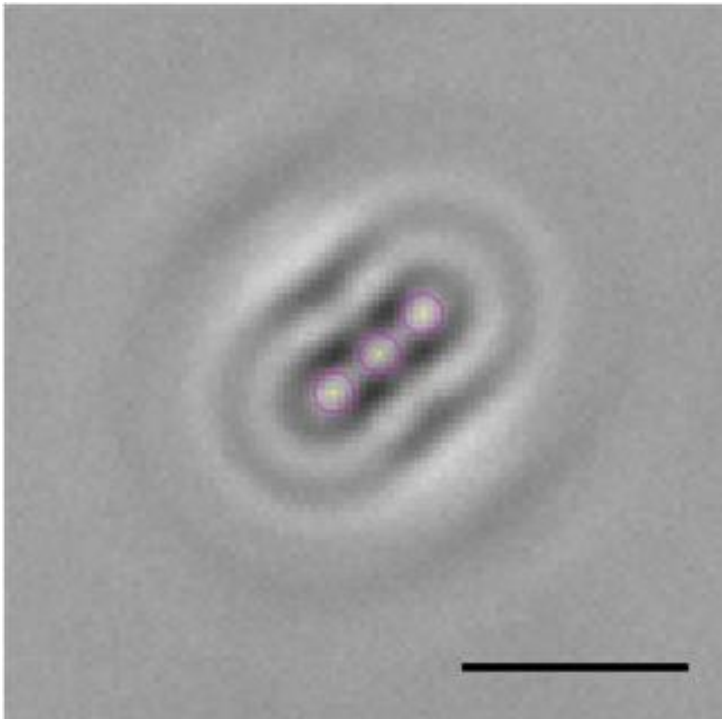

Figure 31: Tracks (yellow lines) of the three sections (purple circles) of a bacterium statically attached to the BKC surface. The dynamics of the bacterium has been monitored for approximately 20s. The length of the scale bars is 5 µm.

BKC is a cationic surfactant well-known for its antimicrobial properties [102]. Once deposited, it confers a positive net charge to the surface, attracting the negative charge of bacteria and causing them to suddenly become statically adhered once delivered to the surface (Fig S14-S16 in the electronic supplementary material). Moreover, BKC is able to denature proteins and disrupt the cytoplasmic membrane of bacteria, causing their death [103]. The disruption of the membrane was demonstrated by the fluorescence analysis conducted staining bacteria with Trypan blue, a dye able to penetrate cells with disrupted membranes [104]. As shown in Figure 32, bacteria exposed to BKC surface are permeable to trypan blue, meaning that their membrane integrity is compromised as a result of the exposure to the antimicrobial agent.

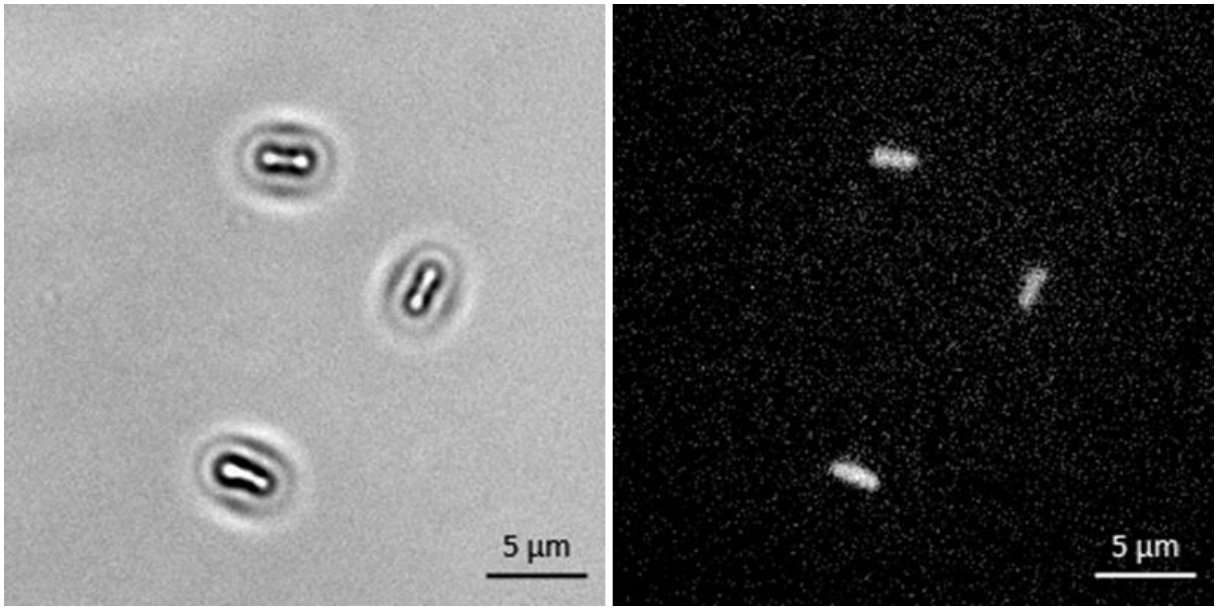

Figure 32: Bacteria stained with trypan blue and statically attached to a BKC surface imaged with an inverted optical microscope in caustics mode (top) and fluorescence mode (bottom).

Moreover, the optical signatures generated by several non-viable bacteria were different from the ones produced by healthy bacteria adhered to the surface and were not aligned with the surface, probably as a result of the degradation of the membrane (Fig. 33).

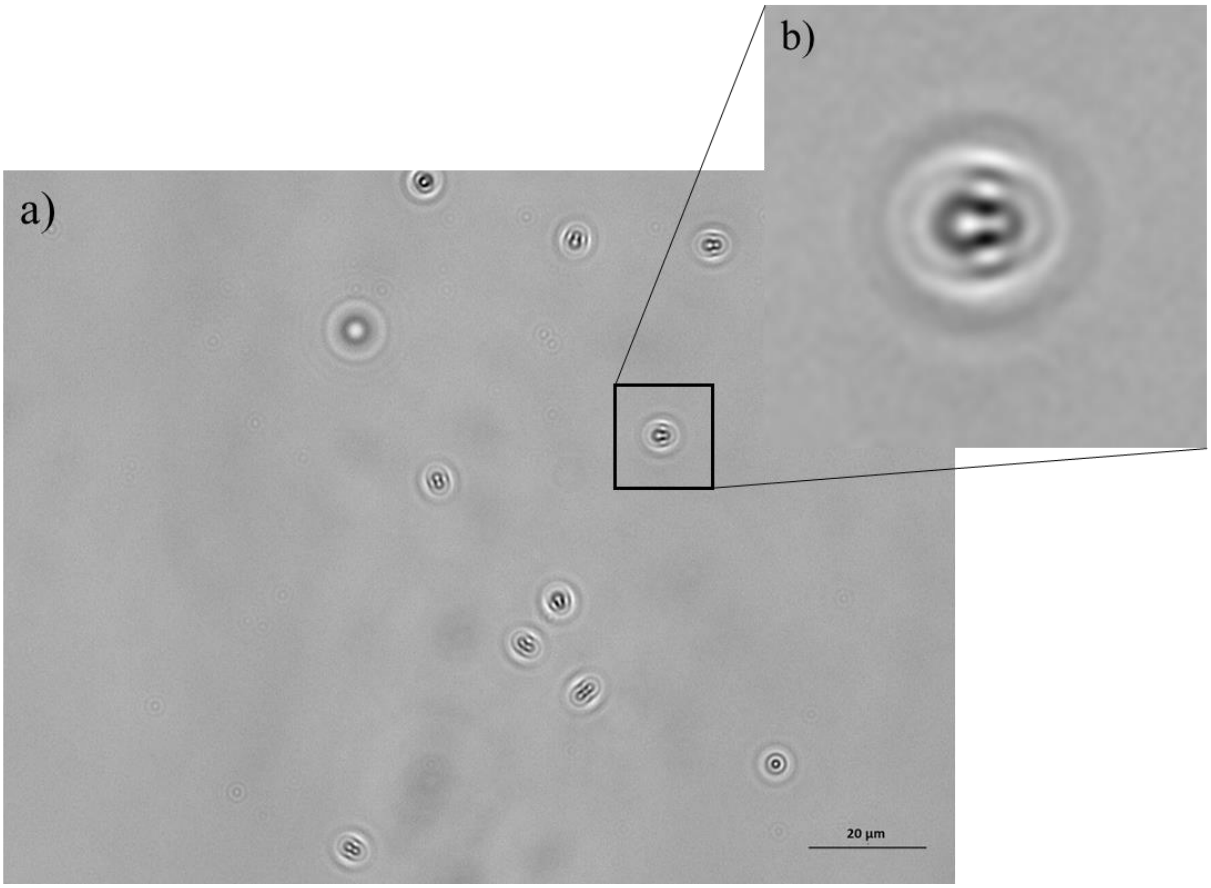

Figure 33: a) Population of dead Escherichia coli bacteria dispersed in PBS and exposed to a glass surface treated with BKC for 1h and b) detail of one bacterium not aligned with the surface.

Even in this case, no noticeable differences can be seen between the behaviour of bacteria in PBS and LB. However, BKC is particularly efficient at degrading the type of nutrients in the specific LB formulation used in this study, which increased the noise in the images (Fig. 34).

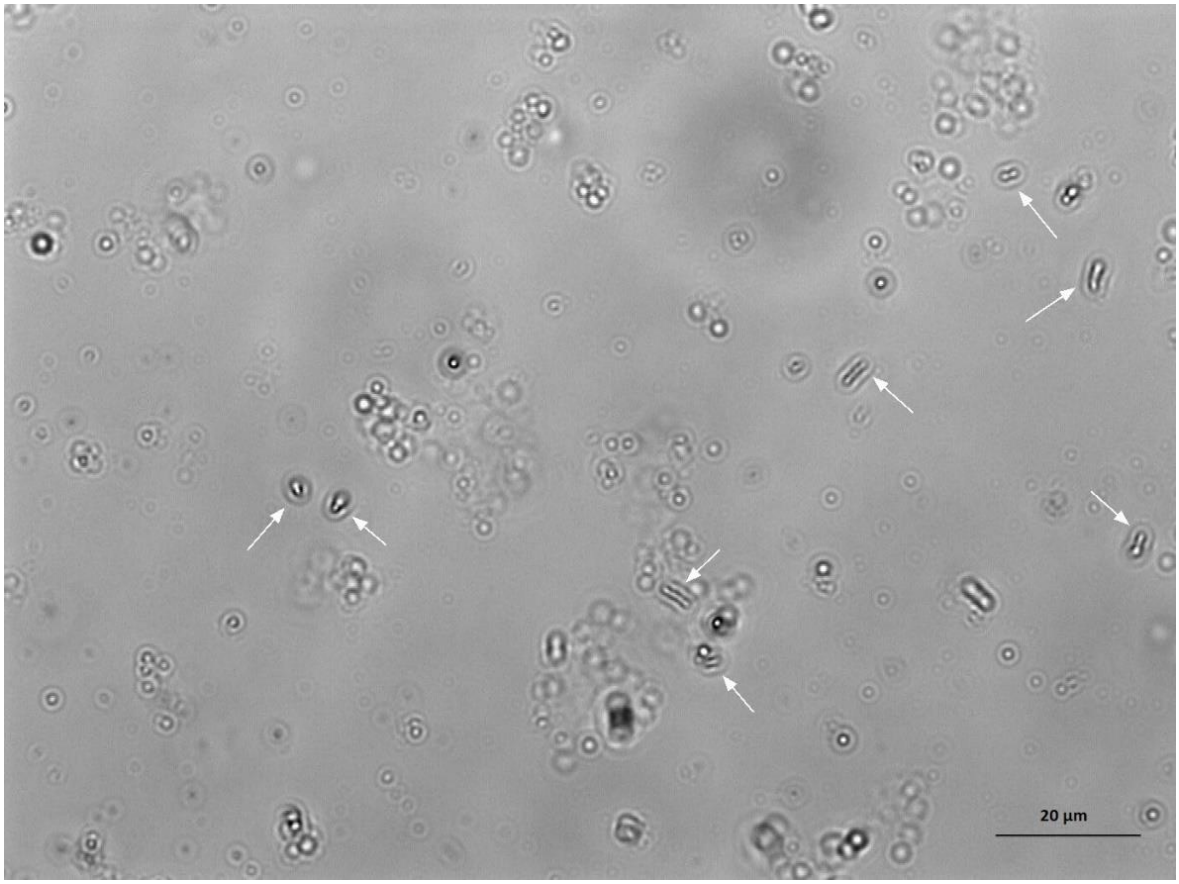

Figure 34: Population of dead Escherichia coli bacteria dispersed in a solution of 10% LB in PBS and exposed to a glass surface treated with BKC for 1h. BKC degrades the nutrients in solution, increasing the noise in the image. However, it is still possible to recognise dead bacteria statically adhered to the surface (highlighted by white arrows).

The images acquired after 24h of bacteria exposure to surface treated with BKC further demonstrated the effectiveness of the antimicrobial compound at killing the bacteria on contact. Figure 35 shows no growth of the population of bacteria dispersed in PBS and exposed to surface treated with BKC and an absence of the formation of a biofilm.

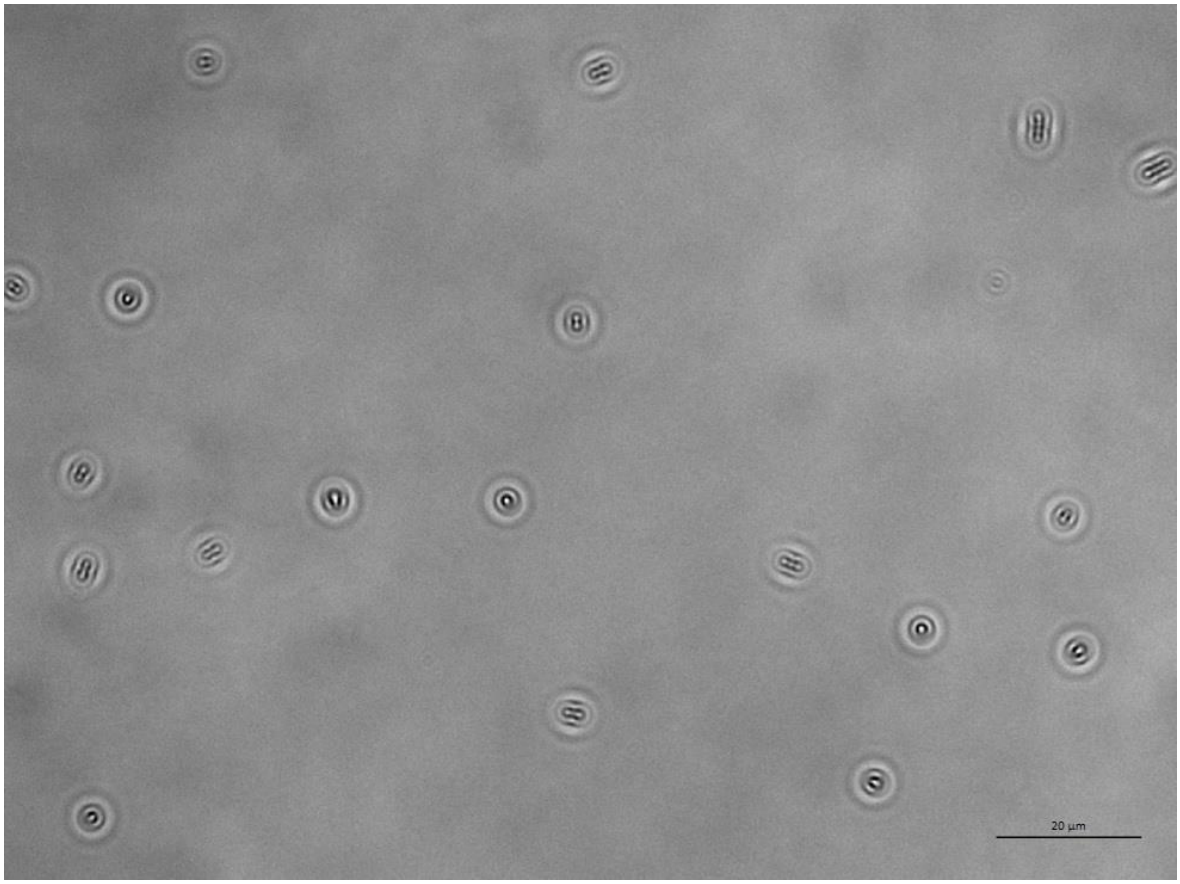

Figure 35: Population of dead Escherichia coli bacteria dispersed in a PBS and exposed to a glass surface treated with BKC for 24h.

4.6. Intracellular organelles dynamics and re-arrangement

The ability of the imaging techniques based on caustics coupled with DIC analysis to characterise the dynamics of the optical pattern generated by intracellular organelles was tested by recording video of the area surrounding the nucleus of human mesenchymal stem cells over a period of approximately 5 min. During the recording, the state of the cells was perturbed by the introduction of ethanol into the cell solution. Figures 36 and 37 show the displacement map obtained by tracking the facets over time and the relative velocity vector map respectively.

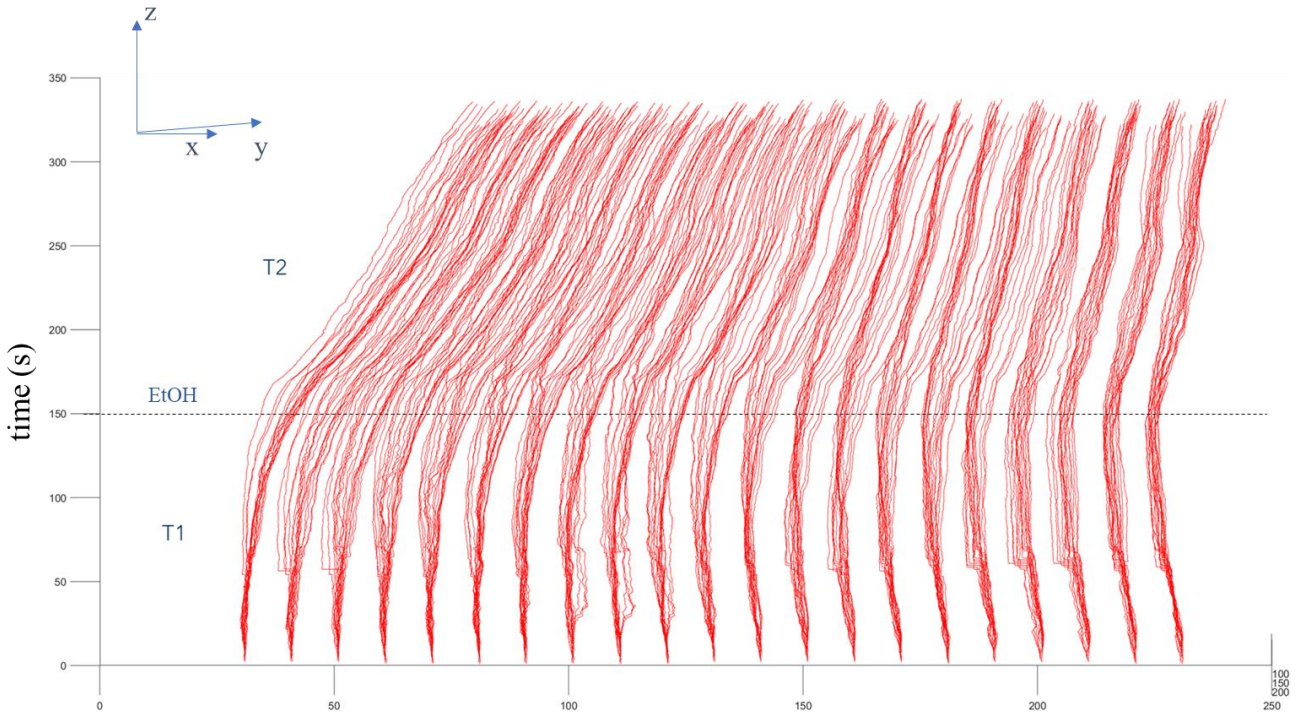

Figure 36: Displacement map of the facets associated with the intracellular organelles of a cell before (t = T1) and after (t = T2) the injection of ethanol in solution.

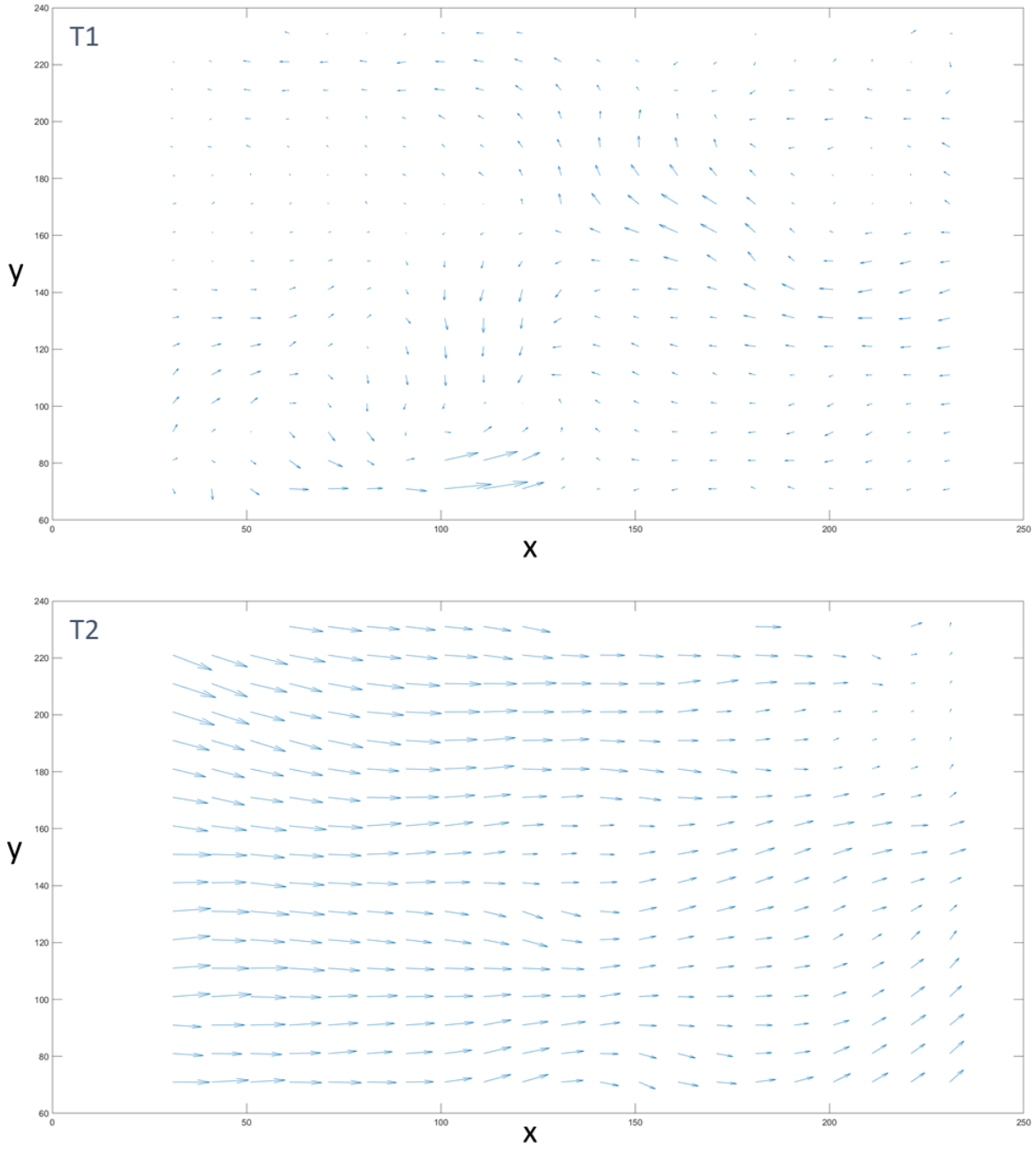

Figure 37: Velocity map of the facets associated with the intracellular organelles of a cell before (t = T1) and after (t = T2) the injection of ethanol in solution.

During the first phase of the recording (t = T1), i.e. when cells were not subjected to any external stress, the cytoplasmatic dynamics exhibited an overall random pattern. However, after the ethanol injection in the solution (t = T2), the overall dynamics of the cytoplasm transitioned from random to oriented (from left to right for the specific cell monitored). Intracellular organelles dispersed in the cytoplasmatic fluid have been reported to experience

random motion [10, 105-106], and these random fluctuations contribute to the spatial distribution of key cellular components, such as ribosomes and proteasomes, to facilitate the efficient translation and degradation of proteins and the removal of enzyme products from their site of synthesis in metabolic reactions (avoiding local concentration effects). The random motion internal to the cytoplasm is believed to be caused primarily by a passive thermally-induced diffusive Brownian process, but a recent work proposed by Guo et al. provided evidence that it is a result of active ATP-dependent processes, thus arising from the overall cellular activity [54]. ATP-dependent random fluctuating motion has also been observed in prokaryotic cells and yeast [107-108]. These results support this speculation, because the presence of ethanol in solution caused a noticeable change in the cytoplasmatic dynamics from random to directed towards a specific direction. Ethanol has been extensively reported to be toxic to cells [109-110] and has been proven to affect cellular processes even at low concentration [111-112]. Moreover, ethanol has been reported to trigger apoptotic cell death [113-114]. Cells exposed to ethanol exhibited the classical features of apoptosis process, namely the change of morphology, the decrease in volume and eventually the detachment from the surface (data not shown) [115]. Hence, it is reasonable to assume that the ensemble forces from overall cellular activity are likely to influence the overall motion within the cytoplasm and that a clear characterisation of intracellular dynamics could thus be a critical readout of the state of the cell. This preliminary finding demonstrates the potential of the optical and tracking methods used in this study to quantify cytoplasmatic dynamics in real-time and non-invasively, paving the way for future investigations of the relationship between the dynamics of intracellular organelles and cellular activity.

4.7. Discussion

The dynamics of metallic and organic particles at the nanoscale is typically investigated either with fluorescence microscopy or with indirect measurements (e.g. with dynamic light scattering analysis), because of the limited spatial resolution achievable by common light microscopy systems. However, the techniques currently in use are not suitable to perform real-time, non-invasive and direct analyses for an extended timescale. Because of these limitations, the dynamics of particles at the nanoscale is still poorly characterised experimentally and predicted theoretically with mathematical models developed for particles bigger in size dispersed in simple fluids. The optical set-up used in this research project is not subjected to the limitations of conventional light and fluorescence microscopy, allowing for the non-invasive monitoring and quantification of the dynamics of particles at the nanoscale in real-time for an extended timescale.

The investigations conducted on the dynamics of nanoparticles aimed to provide a clearer characterisation of the two and three – dimensional motion and transport of nanoparticles in solution and the forces influencing such dynamics. Concerning the 2-dimensional diffusion process of nanoparticles, the contribution of electrochemical interaction forces is typically not taken into account when considering the dynamics of nanoparticles in solution, despite this kind of interactions have been reported to be dominant at the nanoscale and to regulate a range of processes including surface adhesion, friction, and colloid stability [19-20]. The analysis of the diffusion process of gold nanoparticles dispersed in solutions with different ionic contents confirmed the influence of interaction forces on the dynamics of nanoparticles. All the particles tested exhibited an increase in the experimental diffusion coefficient as a function of the molarity of the solution, transitioning from the slow diffusion regime for nanoparticles in a simple fluid at low concentration (already reported in the literature [5]), to a faster diffusion regime of the order of magnitude of the one predicted by the Stokes-Einstein equation.

In the same way, the three-dimensional dynamics of nanoparticles and the associated settling dynamics is usually neglected, despite knowing the concentration profile of nanoparticles is a critical parameter in pharmacological and toxicological applications, when investigating the interaction of particles and cells. A decade ago, Wittmaack highlighted that the main shortcoming of contemporary nanotoxicological studies is the assumption that nanoparticle toxicity can be investigated by applying techniques developed for the risk assessment of hazardous chemical substances, dissolved or dispersed in molecular form. However, insoluble nanoparticles suspended in liquid media are subjected to gravitational and diffusion forces and cannot be assumed to be uniformly distributed in the suspension [116]. Few years later, Krug re-interpreted this concept by evidencing the need for the precise quantification of an appropriate dose and concentration of nanomaterials interacting with cells [23]. However, the majority of the in-vitro nanotoxicological and nano pharmacological investigations are still conducted assuming the paradigm of the uniform distribution of the nanoparticles in solution. The three-dimensional dynamics of nanoparticles was found to contrast with the current assumption of negligibility of the settling dynamics of nanoparticles when subjected to Brownian as well as gravitational forces. In fact, the settling analysis performed on gold nanoparticles demonstrated that for particles with a diameter bigger than 60 nm, the assumption that the initial administered concentration equals the target concentration is misleading and can result in a potential under-overestimation of the results obtained. All the particles tested below 100 nm in diameter reached the sedimentation-diffusion equilibrium in as little as 1 h, with the concentration of particles sedimented down at least 1.5x the initial administered concentration. The settling dynamics was found to be dependent on the size, colloidal stability, and local concentration of particles, thus further confirming the role of interaction forces acting between particles to regulate their dynamics.

The asymmetric flow field-flow fractionation coupled with online dynamic light scattering analysis further supported the dependence of the diffusion dynamics of nanoparticles on their concentration in solution. The U-shaped distribution for the diameters detected by the DLS as a function of the elution time and of the concentration of particles in suspension is a phenomenon that can be found in a significant number of studies in the literature describing the application of asymmetric flow field flow fractionation to separate and characterise particles of various sizes and materials [64-68]; however, a clear understanding of the factors regulating its appearance is still missing. The results obtained demonstrate that this phenomenon is enhanced for solution of particles at low concentration, as a consequence of the unexpected slow diffusion dynamics exhibited by nanoparticles at low concentration. Dynamic light scattering does not consider possible deviation from the classical Stokes-Einstein diffusive regime [64], thus it misinterprets the slower diffusion behaviour of nanoparticles as a result of the presence of bigger particles in solution, detecting a size increase of at least the 50% with respect to the nominal diameter in solutions of 40 nm diameter nanoparticles at concentration of 10^9 particles ml^{-1}.

The ability of the optical set-up based on caustics to perform real-time, non-invasive, and long-term imaging investigations also provided the potential for the quantitative analysis of the mechanism of attachment of bacteria on surfaces and the subsequent formation of a biofilm. Typically, investigations of bacteria biofilms and their viability are conducted using fluorescence microscopy, so they are subjected to the same limitations discussed for metallic nanoparticles. Moreover, little is known about the dynamics of the initial attachment of a bacterium to a surface and its ability to form biofilms. Several techniques are available and routinely used to evaluate the presence of already formed and developed biofilms, but little is known about the preliminary stage of biofilm formation [117]. The imaging analysis of *Escherichia coli* aimed to characterise the mechanism of attachment of bacteria to control and

antimicrobial surfaces, to evaluate the efficiency of antimicrobial surfaces on killing bacteria and preventing biofilms formation. The results obtained provide evidence for the relationship between the dynamics of the bacteria when interacting with a surface and their viability or ability to form a biofilm. Once in contact with the antimicrobial surface, the bacteria died as a result of the exposure to the antimicrobial agent and statically adhere to the surface. On the other hand, bacteria adhered to control surfaces exhibited rotary or laterally dynamics, and probably started to secret EPS to favour other bacteria attachment to form a biofilm as described in the literature [47]. The 24h analysis confirmed the presence of biofilm communities in the bacteria population not exposed to BKC, consisting of a layer of bacteria attached to the surface and aligned in a semi-ordered way.

The capability of the imaging technique used in this study was further investigated for eukaryotic cells, aiming to understand the potential of the optical set-up based on caustics coupled with digital image correlation on characterising the dynamics internal to the cytoplasm. As for bacteria and metallic nanoparticles, there is a lack of non-invasive techniques enabling the real-time monitoring of the dynamics of cellular organelles and components. Given the crowded nature of the intracellular environment, the targeted tracking of specific components or organisms tracking is impractical, unless using fluorescence microscopy [52]. Moreover, the dynamic organization of the organelle networks mediates the direct material exchange between different compartments and enables them to adapt to internal and external stimuli in serving critical cellular functions [118]. Hence analysing the motion and re-arrangement of the entire intracellular environment can potentially provide information about the cellular activity. Coupling the optical set-up based on caustics with digital image correlation analysis allowed the characterisation of the motion of the entire optical pattern generated by intracellular organelles of human mesenchymal stem cells over time without the need for fluorescence labelling. The digital image correlation analysis was proven to be able to detect the transition

from Brownian to oriented motion of the optical signature generated by intracellular organelles when exposed to ethanol. The Brownian motion of intracellular organelles has already been described in the literature, but the transition to an oriented motion as a result of a chemical stimulus external to the cell could potentially reveal the role of the dynamics of intracellular organelles as an indicator of cellular processes.

4.8. Future works

4.8.1. Nanoparticles interaction with cells

Conventional drug delivery systems present a number of critical issues associated with the sensitive toxicity, poor specificity, and drug resistance induction, which decrease the therapeutic efficiency of the drug systems. Nanocarrier-based delivery platforms typically consist of colloidal nanoparticles conjugated with therapeutic active drugs. These nanostructured prototypes have enabled effective delivery of active drugs to diseased tissues. The use of nanocarriers in drug delivery applications aims to treat a disease effectively minimising side effects. However, a clear characterisation and quantification of the interaction of nanoparticles with cells in real-time is needed to optimise nanoparticle delivery mechanisms to cells and support the translation of such applications to in-vivo environments. The optical set-up based on caustics represents a promising technique to perform real-time and non-invasive monitoring of the nanoparticles - cells interactions over time. A preliminary investigation conducted during this PhD demonstrated the possibility to distinguish between various cell types and the nanoparticles in solution due to the different optical signatures generated, allowing for the direct monitoring and potentially the characterisation of such interactions (Fig. 37).

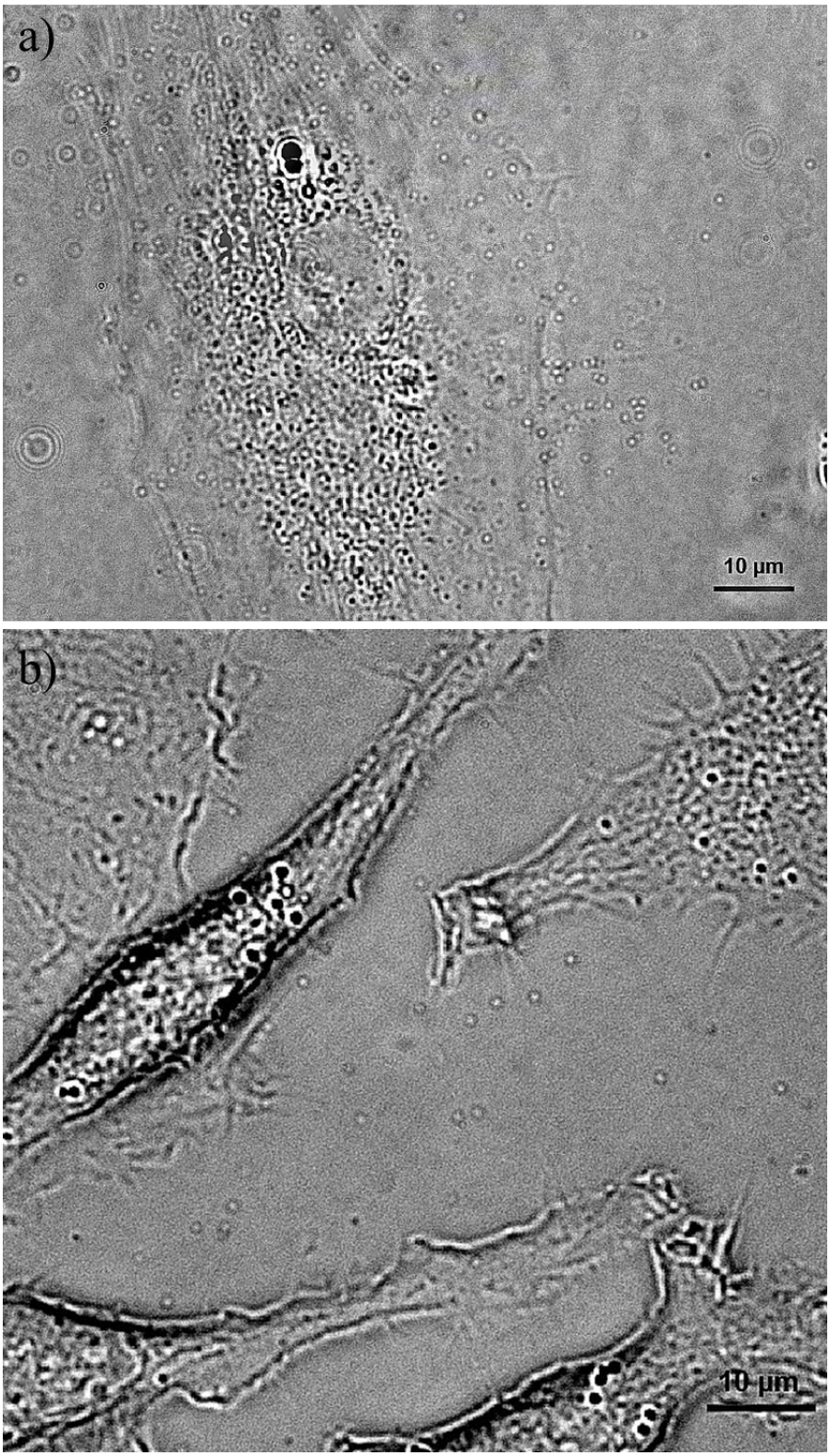

Figure 38: 100 nm gold nanoparticles interacting with: (a) stem cell; (b) fibroblasts. Cells are out of focus to allow the correct formation of the caustics of the particles.

4.8.2. Bacteria and Virus tracking

The successful monitoring and characterisation of *Escherichia coli* bacteria interaction with surfaces paves the way for a number of investigations involving others strains of bacteria and different antimicrobial surfaces. In this study, the attention was focused on *Escherichia coli* bacteria because they are typically used as a reference strain to model bacteria behaviour. Preliminary investigations conducted with the optical set-up used in this thesis on *Pseudomonas aeruginosa* bacteria suggested that even this kind of bacteria exhibit a dynamics similar to *Escherichia coli* when interacting with surfaces (Fig. 38).

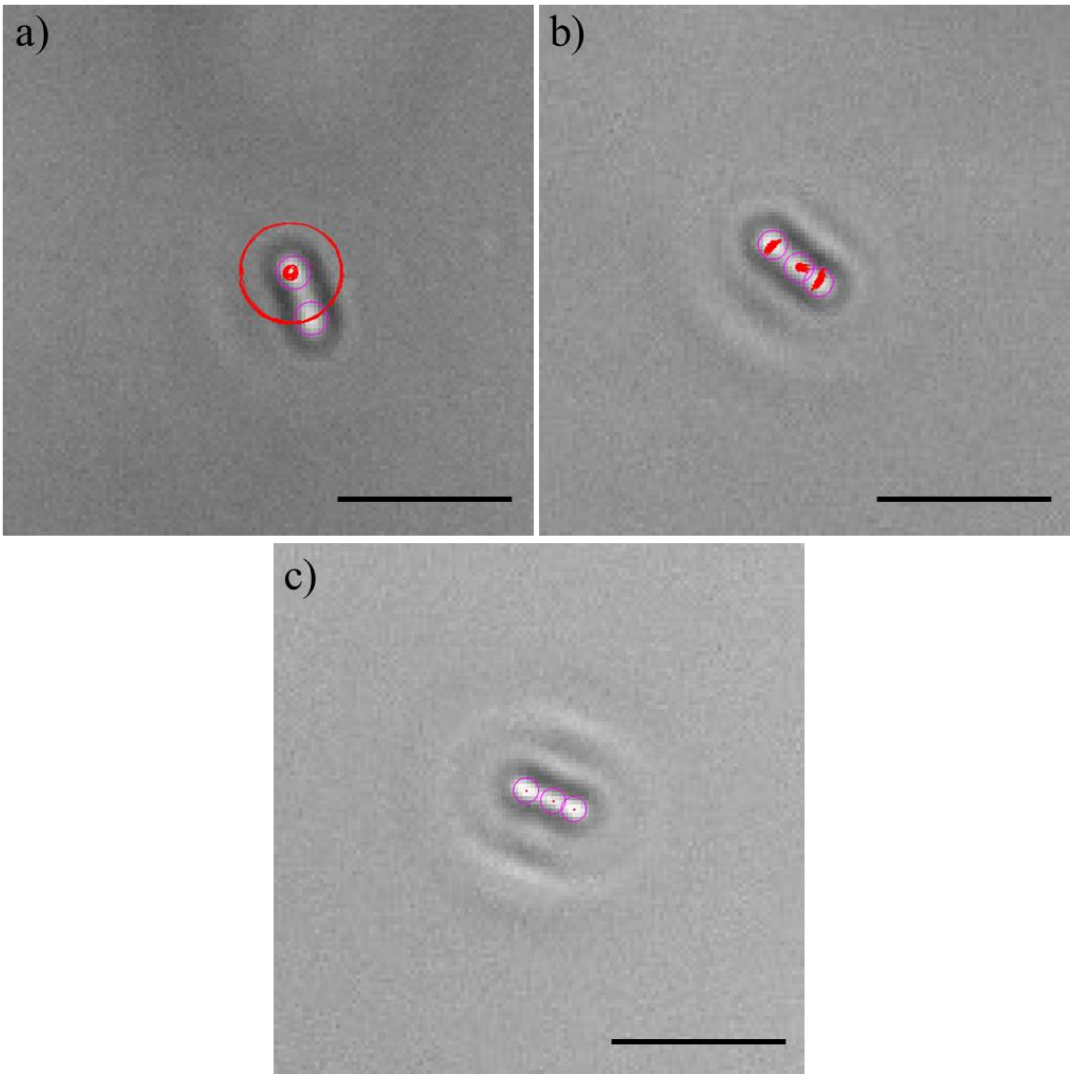

Figure 39: Tracks (red lines) of the three sections (purple circles) of P. aeruginosa bacteria experiencing: a) rotary attachment; b) lateral attachment; c) dead. The dynamics of the three bacteria has been monitored for approximately 20s. The length of the scale bars is 5 μm.

Pseudomonas aeruginosa is a Gram-negative, rod-shaped, asporogenous, and monoflagellated bacterium, known for causing serious infections in immunocompromised patients with cancer and patients suffering from severe burns and cystic fibrosis [119]. However, *Escherichia coli* and *Pseudomonas aeruginosa* cells have similar morphology, and thus are likely to exhibit a similar dynamics when interacting with surfaces. An extension of the findings reported in this thesis would be the characterisation of the dynamics of bacteria with different morphologies, for instance cocci (spherical geometry) or spirochaete (spiral geometry). Moreover, given the ability of the optical set-up used to visualise particles at the nanoscale, a potential future investigation could involve the monitoring and the characterisation of the dynamics of virus particles. Viruses are parasites consisting of genetic material encapsulated in a protein membrane with a size typically in the range of 20–200 nm in diameter [120]. Viruses are commonly imaged with fluorescence microscopy, but preliminary imaging tests conducted on T4 and MS2 bacteriophages demonstrated the possibility to generate optical signatures detectable with the optical set-up based on caustics (Fig. 39). This ability allows the label-free monitoring of the motion of viruses and their interaction with cells, potentially providing information to model their transport in biological systems and to enhance the understanding of the penetration mechanism into bacteria and human cells.

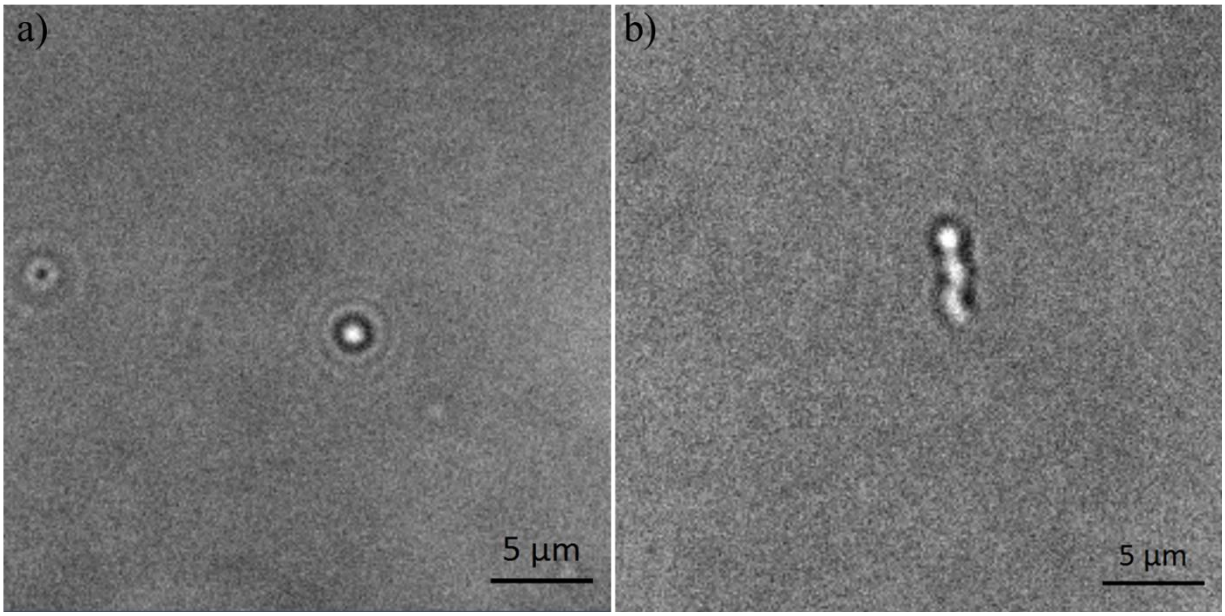

Figure 40: Photograph of the caustics generated by a) MS2 phage and b) T4 phage.

4.8.3. Characterisation of the intracellular organelles dynamics

The analysis on the dynamics of intracellular organelles demonstrated the possibility to characterise the motion internal to the cytoplasm of human cells. It has been speculated that the cytoplasmatic dynamics could be linked with cellular processes, hence a detailed characterisation of the factors influencing such dynamics could potentially be used as an early indicator of the state of a cell when subjected to external stimuli (e.g. during the mechanotransduction process) or when undergoing specific internal processes (e.g. during cellular differentiation or duplication).

CHAPTER 5

5. Conclusion

In this thesis the dynamics of nanoparticles and biological organisms at the micro and nano scale have been characterised in a common inverted optical microscope exploiting the optical phenomenon of caustics. This research has addressed the need for a real-time, non-invasive direct observation and quantification of the dynamics of particles as well as biological organisms at the micro and nano scale. The dynamics of nanoparticles in solution has already been demonstrated to be one of the primary factors influencing a range of phenomena, such as cellular uptake and toxicity, but an empirical characterisation of the mechanisms regulating their motion and transport through liquid had not been presented. The two-dimensional investigation of the diffusion dynamics of gold nanoparticles in salt solutions provides evidence of the influence of electrostatic and Van der Waals forces on the diffusion of gold nanoparticles. The effect of these two forces was found to be dominant with respect to other factors, such as particle size, which was found to be negligible within the tested range and concentration of nanoparticles. These findings highlight the complexity of the diffusion process and have potential implications, for example, for understanding and predicting the behaviour of nanoparticles dispersed in biological media which typically contain NaCl in solution. On the other hand, the three-dimensional investigation of the settling dynamics of nanoparticles demonstrated the factors influencing the concentration profile of nanoparticles in solution at the sedimentation-diffusion equilibrium and the limitations of the current theoretical model. The experimental results demonstrated that nanoparticle size, colloidal stability and solution temperature drive the sedimentation-diffusion equilibrium of nanoparticles in solution and that, for particles larger than 60 nm in diameter, the target dose differs significantly from the administered dose in both water and cell culture medium. This evidence should be taken into account when performing in vitro studies using adherent 2D cultures, where the actual

concentration of nanoparticles interacting with cells is needed to characterise and evaluate the cellular response. Moreover, the classical Mason – Weaver model was modified following the speculation about the dependence of the diffusion coefficient on the local concentration of nanoparticle in solution. The new version of the model shows good agreement with experimental data and is able to accurately describe the settling dynamics and concentration profile of nanoparticles in solution, making it a promising tool for the design of in vitro experiments and the study of concentration-response relationships.

The ability of our optical setup to generate optical signatures from protein particles, allowed also for the design of imaging experiments on organisms. The mechanisms of attachment of *Escherichia coli* bacteria have been investigated against control glass surfaces and glass with an antimicrobial coating. The results demonstrated that the viability of bacteria and their ability to start biofilms can be investigated by evaluating their dynamics and their interactions with the surface. Healthy bacteria adhered to the glass control surface and exhibited a detectable lateral or rotary motion. Hence, observation of these behaviours allows for the early recognition of the occurrence of a potential biofilm. On the other hand, dead bacteria adhered statically to the surfaces treated with BKC, as a result of the attractive electrostatic force and of the degradation of their external membrane. These findings not only provide new empirical insights into bacteria-surface interactions in real-time, but also have potential implications in investigations of the early formation of a biofilm or of the efficiency of an antimicrobial coating.

Finally, the imaging analysis performed on human mesenchymal stem cells demonstrated the potential of our optical technique to generate image data containing information about the dynamics internal to the cytoplasm. The data acquired was analysed with digital image correlation and demonstrated a detectable change in the dynamics of intracellular organelles

from random to oriented when the cells were exposed to ethanol. The dynamics of intracellular organelles has been suggested to be directly linked with the cellular process and thus monitoring and quantifying intracellular interactions and re-arrangement could be critical to evaluate cellular physiology and functions. Hence, the caustics optical technique coupled with digital image correlation represents a promising tool for future investigations exploring the dynamics internal to the cells.

6. APPENDIX

6.1. Derivation of the modified Stokes-Einstein equation

Following the assumption that the diffusion coefficient, *D* is not constant but depends on the local concentration of the nanoparticles and thus also on the position *z* and time *t*, the Mason-Weaver convection-diffusion differential equation in the form of (7) is not correct and needs to be derived supposing a function of the form *D(n(z,t))*. We can start with Fick's second law:

$$\frac{\partial n(z,t)}{\partial t} = -\frac{\partial J(z,t)}{\partial z} \tag{12}$$

where $J(z,t)$ is the flux of nanoparticles. In our scenario:

$$J(z,t) = J_D(z,t) + J_S(z,t) \tag{13}$$

where $J_D(z,t)$ is the diffusion flux defined by Fick's first law:

$$J_D(z,t) = -D\big(n(z,t)\big)\frac{\partial n(z,t)}{\partial z} \tag{14}$$

and $J_S(z,t)$ is the sedimentation flux expressed as:

$$J_S(z,t) = Vn(z,t) \tag{15}$$

Combining (12) to (15) we get the Mason-Weaver equation with a non-constant diffusion coefficient, *D:*

$$\frac{\partial n(z,t)}{\partial t} = \frac{\partial}{\partial z}\left(D(n(z,t))\frac{\partial n(z,t)}{\partial z}\right) - V\frac{\partial n(z,t)}{\partial z} \tag{16}$$

To solve it, the *z* coordinate was first transformed to a non-dimensional form:

$$z' = \frac{z}{L} \tag{17}$$

Then equation (16) was solved using the Euler explicit method where the derivatives were approximated by finite differences. The space and time domains were uniformly partitioned in a mesh. The space step was *L*/100 so the non-dimensional $\Delta z = 0.01$ and the time step $\Delta t = 0.4$s

was chosen to maintain a stable solution of the equation over time.

The points $n(z_j', t_u) = n_j^u$ represent the numerical approximation of the concentration at the space point z_j' and time point t_u. The equation (16) after the approximation by finite differences becomes:

$$\frac{n_j^{u+1} - n_j^u}{\Delta t} = \frac{D(n_{j+1}^u)(n_{j+1}^u - n_j^u) - D(n_j^u)(n_j^u - n_{j-1}^u)}{L^2 \Delta z^2} - \frac{V(n_{j+1}^u - n_j^u)}{L \Delta z} \quad (18)$$

Using this relation and knowing the values of the concentration at time *u*, we can obtain the concentration at time *u+1* (computational stencil shown in Fig. 40a):

$$n_j^{u+1} = n_j^u + \Delta t \left(\frac{D(n_{j+1}^u)(n_{j+1}^u - n_j^u) - D(n_j^u)(n_j^u - n_{j-1}^u)}{L^2 \Delta z^2} - \frac{V(n_{j+1}^u - n_j^u)}{L \Delta z} \right) \quad (19)$$

To calculate the nanoparticle concentration at the boundaries, we apply the boundary condition that there is no particle flux across the top and the bottom of the solution. By combining equations (12) and (13) the Mason-Weaver equation is obtained as function of the nanoparticle fluxes:

$$\frac{\partial n(z,t)}{\partial t} = -\frac{\partial}{\partial z}(J_D(z,t) + J_S(z,t)) \quad (20)$$

The derivatives in this equation (20) can be approximated by finite differences:

$$\frac{n_j^{u+1} - n_j^u}{\Delta t} = -\frac{1}{L}\frac{J_D'' - J_D'}{\Delta z} - \frac{1}{L}\frac{J_S'' - J_S'}{\Delta z} \quad (21)$$

where J_D'' and J_S'' are the diffusion and sedimentation fluxes between n_j^u and n_{j+1}^u, and J_D' and J_S' are the diffusion and sedimentation fluxes between n_{j-1}^u and n_j^u.

At the top boundary, z = *L* (*j* = 100), these four fluxes, depicted also in the computational stencil (Fig. 40b), are as follows:

$$J_D^{''} = 0, \qquad J_D^{'} = -\frac{D(n_{100}^u)}{L}\frac{(n_{100}^u - n_{99}^u)}{\Delta z}$$

$$J_S^{\prime\prime} = 0, \qquad J_S^{\prime} = Vn_{100}^u$$

Consequently, the equation (11) at the top boundary takes the form:

$$n_{100}^{u+1} = n_{100}^u + \Delta t\left(-\frac{D(n_{100}^u)}{L^2}\frac{(n_{100}^u - n_{99}^u)}{\Delta z^2} + \frac{V}{L}\frac{n_{100}^u}{\Delta z}\right) \tag{22}$$

Similarly, at the bottom boundary, z = 0 (j = 0), and the four fluxes J_D'', J_S'', J_D', and J_S' (Fig. 40c) are as follows:

$$J_D^{\prime\prime} = -\frac{D(n_1^u)}{L}\frac{(n_1^u - n_0^u)}{\Delta z}, \qquad J_D^{\prime} = 0$$

$$J_S^{\prime\prime} = Vn_1^u, \qquad J_S^{\prime} = 0$$

Consequently, the equation (11) at the bottom boundary becomes:

$$n_0^{u+1} = n_0^u + \Delta t\left(\frac{D(n_1^u)}{L^2}\frac{(n_1^u - n_0^u)}{\Delta z^2} - \frac{V}{L}\frac{n_1^u}{\Delta z}\right) \tag{23}$$

The diffusion coefficient $D(n)$ as a function of the normalised local concentration of the nanoparticles n can be expressed as:

$$D(n) = D_{exp} + \frac{\left(D_{StEin} - D_{exp}\right)n^k}{n_{50}^k + n^k} \tag{24}$$

The modified version of the Mason – Weaver equation is used in this paper to theoretically predict only the settling dynamics of nanoparticles in solutions at 23°C because of the lack of data concerning the experimental diffusion coefficient exhibited by nanoparticles in solution at higher temperatures.

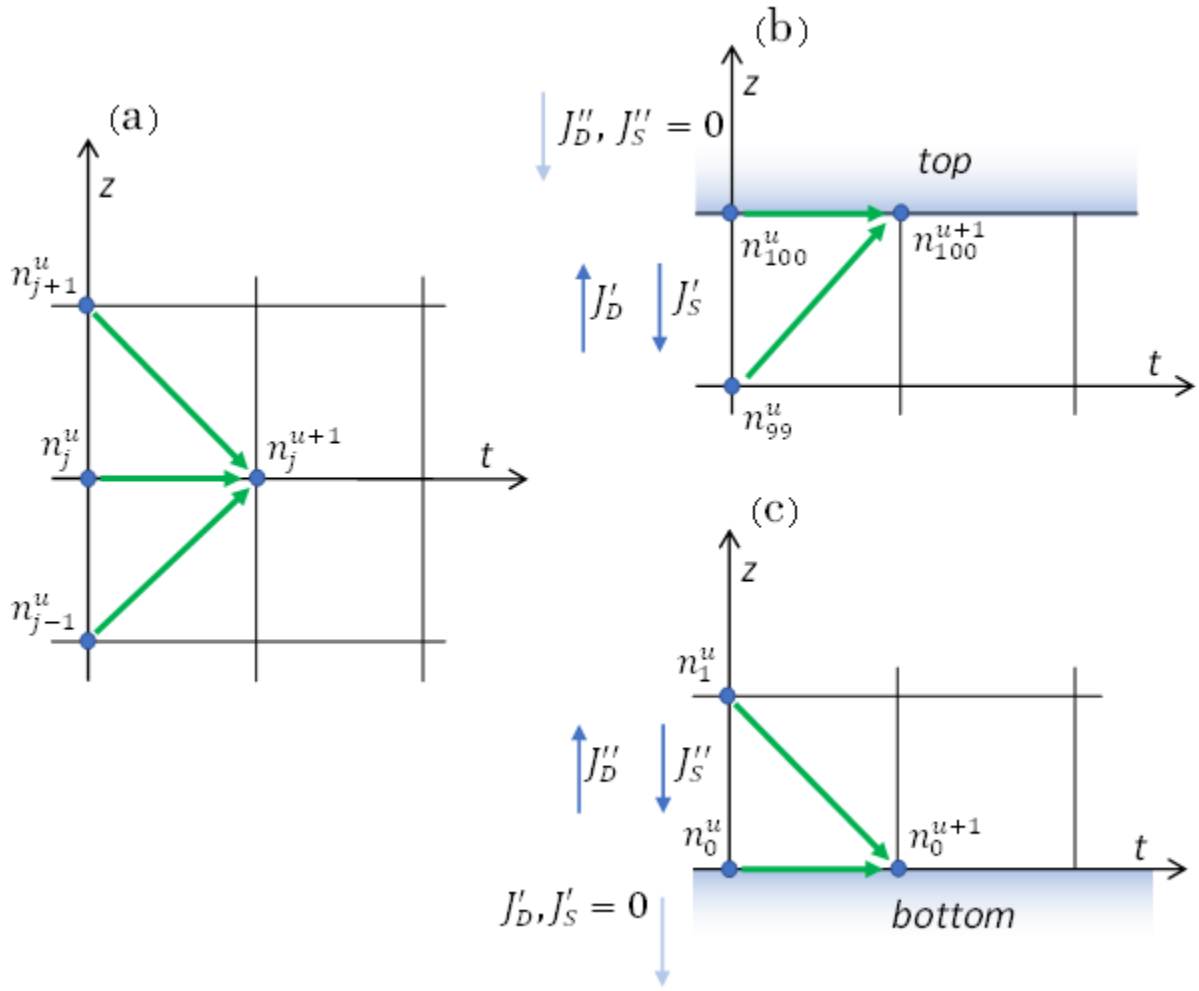

Figure 41: Computational stencils of the explicit Euler forward method (a) at the top (b) and at the bottom (c) with depicted fluxes.

7. REFERENCES

[1] Elahi N, Kamali M, Baghersad MH. Recent biomedical applications of gold nanoparticles: A review. Talanta 2018;184:537-556.

[2] Bleeker EAJ, de Jong WH, Geertsma RE, Groenewold M, Heugens EHW, Koers-Jacquemijns M, van de Meent D, Popma JR, Rietveld AG, Wijnhoven SWP, Cassee FR, Oomen AG. Considerations on the EU definition of a nanomaterial: Science to support policy making. Regul Toxicol Pharmacol 2013;65(1):119-125.

[3] Cho EC, Zhang Q, Xia Y. The effect of sedimentation and diffusion on cellular uptake of gold nanoparticles. Nat Nanotechnol 2011;6(6):385-391.

[4] Cohen JM, Deloid GM, Demokritou P. A critical review of in vitro dosimetry for engineered nanomaterials. Nanomedicine 2015;10(19):3015-3032.

[5] Coglitore D, Edwardson SP, Macko P, Patterson EA, Whelan M. Transition from fractional to classical Stokes-Einstein behaviour in simple fluids. R Soc Open Sci 2017;4(12).

[6] Perez Holmberg J, Abbas Z, Ahlberg E, Hassellöv M, Bergenholtz J. Nonlinear concentration dependence of the collective diffusion coefficient of TiO2 nanoparticle dispersions. J Phys Chem C 2011;115(28):13609-13616.

[7] Gineste J, Macko P, Patterson EA, Whelan MP. Three-dimensional automated nanoparticle tracking using Mie scattering in an optical microscope. J Microsc 2011;243(2):172-178.

[8] Li G, Tam L-, Tang JX. Amplified effect of Brownian motion in bacterial near-surface swimming. Proc Natl Acad Sci USA 2008;105(47):18355-18359.

[9] Hassan PA, Rana S, Verma G. Making sense of Brownian motion: Colloid characterization by dynamic light scattering. Langmuir 2015;31(1):3-12.

[10] Norregaard K, Metzler R, Ritter CM, Berg-Sørensen K, Oddershede LB. Manipulation and Motion of Organelles and Single Molecules in Living Cells. Chem Rev 2017;117(5):4342-4375.

[11] Brown R. A brief account of microscopical observations made in the months of June, July and August 1827, on the particles contained in the pollen of plants; and on the general existence of active molecules in organic and inorganic bodies. Philos Mag Ser 1828; 4(21): 161–173.

[12] Einstein A. On the movement of small particles suspended in stationary liquids required by the molecular-kinetic theory of heat. Annalen der Physik 1905; 322: 549–560.

[13] Michalet X. Mean square displacement analysis of single-particle trajectories with localization error: Brownian motion in an isotropic medium. Phys Rev E Stat Nonlinear Soft Matter Phys 2010;82(4).

[14] Qian H, Sheetz MP, Elson EL. Single particle tracking. Analysis of diffusion and flow in two-dimensional systems. Biophysic J 1991;60(4): 910-921,

[15] Xu L, Mallamace F, Yan Z, Starr FW, Buldyrev SV, Eugene Stanley H. Appearance of a fractional stokes-einstein relation in water and a structural interpretation ofits onset. Nat Phys 2009;5(8):565-569.

[16] Li Z. Critical particle size where the Stokes-Einstein relation breaks down. Phys Rev E Stat Nonlinear Soft Matter Phys 2009;80(6).

[17] Hinderliter PM, Minard KR, Orr G, Chrisler WB, Thrall BD, Pounds JG, Teeguarden JG. ISDD: A computational model of particle sedimentation, diffusion and target cell dosimetry for in vitro toxicity studies. Part Fibre Toxicol 2010;7.

[18] Stokes GG. On the Effect of the Internal Friction of Fluids on the Motion of Pendulums. Trans Cambridge Philos Soc 1850; 9(2):8-106.

[19] Ishida N, Craig VSJ. Direct measurement of interaction forces between surfaces in liquids using atomic force microscopy. KONA Powder Part J 2019; 36:187-200.

[20] Leite FL, Bueno CC, Da Róz AL, Ziemath EC, Oliveira Jr. ON. Theoretical models for surface forces and adhesion and their measurement using atomic force microscopy. Int J Mol Sci 2012;13(10):12773-12856.

[21] Mason M, Weaver W. The Settling of Small Particles in a Fluid. Phys Rev 1923; 23(3): 412–426.

[22] Midelet J, El-Sagheer AH, Brown T, Kanaras AG, Werts MHV. The Sedimentation of Colloidal Nanoparticles in Solution and Its Study Using Quantitative Digital Photography. Part Part Syst Charact 2017;34(10).

[23] Krug HF. Nanosafety research-are we on the right track? Angew Chem Int Ed 2014;53(46):12304-12319.

[24] Alkilany AM, Murphy CJ. Toxicity and cellular uptake of gold nanoparticles: What we have learned so far? J Nanopart Res 2010;12(7):2313-2333.

[25] Adewale OB, Davids H, Cairncross L, Roux S. Toxicological Behavior of Gold Nanoparticles on Various Models: Influence of Physicochemical Properties and Other Factors. Int J Toxicol 2019;38(5):357-384.

[26] Dukhin SA and Goetz PJ. Fundamentals of Interface and Colloid Science. In: A. S. Dukhin AS and Goetz PJ. Characterization of Liquids, Dispersions, Emulsions, and Porous Materials Using Ultrasound, 3rd ed. Elsevier 2017; 19-83.

[27] Langford A, Bruchsaler M, Gupta M. Suspension properties and characterization of aluminum-adjuvanted vaccines. In: Kolhe P and Ohtake S, ed., Practical Aspects of Vaccine Development. Academic Press 2021:225-266.

[28] Shen H, Tauzin LJ, Baiyasi R, Wang W, Moringo N, Shuang B, Landes CF. Single Particle Tracking: From Theory to Biophysical Applications. Chem Rev 2017;117(11):7331-7376.

[29] Resch-Genger U, Grabolle M, Cavaliere-Jaricot S, Nitschke R, Nann T. Quantum dots versus organic dyes as fluorescent labels. Nat Methods 2008;5(9):763-775.

[30] Wolfbeis OS. An overview of nanoparticles commonly used in fluorescent bioimaging. Chem Soc Rev 2015;44(14):4743-4768.

[31] Thorley JA, Pike J, Rappoport JZ. Super-resolution Microscopy: A Comparison of Commercially Available Options. Fluorescence Microscopy: Super-Resolution and other Novel Techniques; 2014. p. 199-212.

[32] Jensen EC. Use of Fluorescent Probes: Their Effect on Cell Biology and Limitations. Anat Rec 2012;295(12):2031-2036.

[33] Montecinos-Franjola F, Bauer BL, Mears JA, Ramachandran R. GFP fluorescence tagging alters dynamin-related protein 1 oligomerization dynamics and creates disassembly-refractory puncta to mediate mitochondrial fission. Sci Rep 2020;10(1).

[34] Verpillat F, Joud F, Desbiolles P, Gross M. Dark-field digital holographic microscopy for 3D-tracking of gold nanoparticles. Opt Express 2011;19(27):26044-26055.

[35] Leahy B, Alexander R, Martin C, Barkley S, Manoharan VN. Large depth-of-field tracking of colloidal spheres in holographic microscopy by modeling the objective lens. Opt Express 2020;28(2):1061-1075.

[36] Patterson EA, Whelan MP. Tracking nanoparticles in an optical microscope using caustics. Nanotech 2008;19(10).

[37] Hamilton WR. Theory of systems of rays Trans. R. Irish Acad 1828; 15:69–174.

[38] Rosakis A, Krishnaswamy S, Tippur H. On the application of the optical method of caustics to the investigation of transient elastodynamic crack problems: Limitations of the classical interpretation. Opt Lasers Eng 1920; 13(3-4):183-210.

[39] Carazo-Alvarez JD, Patterson EA. General method for automated analysis of caustics. Opt Lasers Eng 1999; 32:95–110.

[40] Wallhead IR, Gungor S, Edwards L. Optimisation of the optical method of caustics for the determination of stress intensity factors. Opt Lasers Eng 1994, 20:109-133.

[41] Patterson EA, Whelan MP. Optical signatures of small nanoparticles in a conventional microscope. Small 2008;4(10):1703-1706.

[42] Milton R, Kwang-Shin K. Structure. In: S. Baron, ed., Medical Microbiology, 4th ed, 1996.

[43] Xiao J, Goley E. Redefining the roles of the FtsZ-ring in bacterial cytokinesis. Curr Opin Microbiol 2016; 34:90-96.

[44] Wilson M. Bacterial biofilms and human disease. Sci Prog 2001;84(3):235-254.

[45] Donlan RM. Biofilms: Microbial life on surfaces. Emerg Infect Dis 2002;8(9):881-890.

[46] Kostakioti M, Hadjifrangiskou M, Hultgren SJ. Bacterial biofilms: Development, dispersal, and therapeutic strategies in the dawn of the postantibiotic era. Cold Spring Harbor Perspect Med 2013;3(4).

[47] Garrett TR, Bhakoo M, Zhang Z. Bacterial adhesion and biofilms on surfaces. Prog Nat Sci 2008;18(9):1049-1056.

[48] Høiby N, Bjarnsholt T, Givskov M, Molin S, Ciofu O. Antibiotic resistance of bacterial biofilms. Int J Antimicrob Agents 2010;35(4):322-332.

[49] Zhang K, Li X, Yu C, Wang Y. Promising Therapeutic Strategies Against Microbial Biofilm Challenges. Front Cell Infect Microbiol 2020;10.

[50] Nadimpalli ML, Chan CW, Doron S. Antibiotic resistance: a call to action to prevent the next epidemic of inequality. Nat Med 2021;27(2):187-188.

[51] Alberts B. Molecular biology of the cell. Garland Science 2008.

[52] Guo Y, Li D, Zhang S, Yang Y, Liu J, Wang X, Liu C, Milkie DE, Moore RP, Tulu US, Kiehart DP, Hu J, Lippincott-Schwartz J, Betzig E, Li D. Visualizing Intracellular Organelle and Cytoskeletal Interactions at Nanoscale Resolution on Millisecond Timescales. Cell 2018;175(5):1430-1442.

[53] Zheng X, Zhu W, Ni F, Ai H, Gong S, Zhou X, Sessler JL, Yang C. Simultaneous dual-colour tracking lipid droplets and lysosomes dynamics using a fluorescent probe. Chem Sci 2019;10(8):2342-2348.

[54] Starling GP, Yip YY, Sanger A, Morton PE, Eden ER, Dodding MP. Folliculin directs the formation of a Rab34-RILP complex to control the nutrient-dependent dynamic distribution of lysosomes. EMBO Rep 2016;17(6):823-841.

[55] Tanaka H, Okazaki T, Aoyama S, Yokota M, Koike M, Okada Y, Fujiki Y, Gotoh Y. Peroxisomes control mitochondrial dynamics and the mitochondrion-dependent apoptosis pathway. J Cell Sci 2019;132(11).

[56] Elbaz-Alon Y, Guo Y, Segev N, Harel M, Quinnell DE, Geiger T, Avinoam O, Li D, Nunnari J. PDZD8 interacts with Protrudin and Rab7 at ER-late endosome membrane contact sites associated with mitochondria. Nat Commun 2020;11(1).

[57] Guo M, Ehrlicher AJ, Jensen MH, Renz M, Moore JR, Goldman RD, Lippincott-Schwartz J, Mackintosh FC, Weitz DA. Probing the stochastic, motor-driven properties of the cytoplasm using force spectrum microscopy. Cell 2014;158(4):822-832.

[58] Jun JY, Nguyen HH, Paik S, Chun HS, Kang B, Ko S. Preparation of size-controlled bovine serum albumin (BSA) nanoparticles by a modified desolvation method. Food Chem 2011;127(4):1892-1898.

[59] Tinevez J, Perry N, Schindelin J, Hoopes GM, Reynolds GD, Laplantine E, Bednarekc SY, Kevin SL, Eliceiri W. TrackMate: An open and extensible platform for single-particle tracking. Methods 2017; 115:80-90.

[60] Messaud FA, Sanderson RD, Runyon JR, Otte T, Pasch H, Williams SKR. An overview on field-flow fractionation techniques and their applications in the separation and characterization of polymers. Prog in Polym Sci 2009; 34(4): 351-368

[61] Eskelin K, Lampi M, Meier F, Moldenhauer E, Bamford DH, Oksanen HM. Asymmetric flow field flow fractionation methods for virus purification. J of Chromatogr A. 2016; 1469:108-119.

[62] Gigault J, Mignard E, Hadri HE, Grassl B. Measurement Bias on Nanoparticle Size Characterization by Asymmetric Flow Field-Flow Fractionation Using Dynamic Light-Scattering Detection. Chromatogr 2017; 80(2): 287-294

[63] Wolfgang H, Nguyen TKT, Jenny A, David GF. Determination of Size and Concentration of Gold Nanoparticles from UV−Vis Spectra. Anal Chem 2007; 79 (11); 4215-4221.

[64] Cho TJ, Hackley VA. Fractionation and characterization of gold nanoparticles in aqueous solution: Asymmetric-flow field flow fractionation with MALS, DLS, and UV-Vis detection. Anal Bioanal Chem 2010; 398(5): 2003-2018.

[65] Jang M, Lee S, Hwang YS. Characterization of silver nanoparticles under environmentally relevant conditions using asymmetrical flow field-flow fractionation (AF4). PLoS ONE. 2015;10(11).

[66] Tuoriniemi J, Johnsson AJH, Holmberg JP, Gustafsson S, Gallego-Urrea JA, Olsson E, Pettersson JBC, Hassellöv, M. Intermethod comparison of the particle size distributions of colloidal silica nanoparticles. Sci and Tech of Ad Mat 2014;15(3).

[67] António DC, Cascio C, Gilliland D, Nogueira AJ, Rossi F, Calzolai L. Characterization of silver nanoparticles-alginate complexes by combined size separation and size measurement techniques. Biointerph 2016; 11(4).

[68] Palais C, Chichester JA, Manceva S, Yusibov V, Arvinte T. Influence of Protein Formulation and Carrier Solution on Asymmetrical Flow Field-Flow Fractionation: A Case Study of the Plant-Produced Recombinant Anthrax Protective Antigen pp-PA83. J of Pharma Sci 2015; 104(2): 612-617.

[69] Braun A, Couteau O, Franks K, Kestens V, Roebben G, Lamberty A, Linsinger TPJ. Validation of dynamic light scattering and centrifugal liquid sedimentation methods for nanoparticle characterisation. Advan Pow Tech 2011; 22(6): 766-770.

[70] Humbert C, Pluchery O, Lacaze E, Tadjeddine A, Busson B. Optical spectroscopy of functionalized gold nanoparticles assemblies as a function of the surface coverage. Gold Bulletin 2013; 46(4):299-309.

[71] Berney M, Hammes F, Bosshard F, Weilenmann H, Egli T. Assessment and interpretation of bacterial viability by using the LIVE/DEAD BacLight kit in combination with flow cytometry. Appl Environ Microbiol 2007;73(10):3283-3290.

[72] Amjad K, Christian WJR, Dvurecenska K, Chapman MG, Uchic MD, Przybyla CP, Patterson EA. Computationally efficient method of tracking fibres in composite materials using digital image correlation. Compos Part A Appl Sci Manuf 2020;129.

[73] Yoshida M, Tsuru S, Hirata N, Seno S, Matsuda H, Ying BW, Yomo T. Directed evolution of cell size in Escherichia coli. BMC Evol Biol 2014;14(1).

[74] Gehri N, Mata-Falcón J, Kaufmann W. Automated crack detection and measurement based on digital image correlation. Constr Build Mater 2020;256.

[75] Christau S, Moeller T, Genzer J, Koehler R, Von Klitzing R. Salt-Induced Aggregation of Negatively Charged Gold Nanoparticles Confined in a Polymer Brush Matrix. Macromolecules 2017;50(18):7333-7343.

[76] Pamies R, Cifre JGH, Espín VF, Collado-González M, Baños FGD, De La Torre JG. Aggregation behaviour of gold nanoparticles in saline aqueous media. J Nanopart Res 2014;16(4).

[77] Goutelle S, Maurin M, Rougier F, Barbaut X, Bourguignon L, Ducher M. Maire P. The Hill equation: A review of its capabilities in pharmacological modelling. Fundam Clin Pharmacol 2008; 22(6): 633-648.

[78] Zhang W. Nanoparticle aggregation: Principles and modelling. 2014 Adv Exp Med Biol 2014; 811(20): 20-43.

[79] Dukhin AS, Goetz PJ. Chapter 2 - Fundamentals of Interface and Colloid Science. In: Dukhin AS, Goetz PJ, editors. Characterization of Liquids, Dispersions, Emulsions, and Porous Materials Using Ultrasound (Third Edition): Elsevier; 2017: 19-83.

[80] He Z, Alexandridis P. Nanoparticles in ionic liquids: Interactions and organization. Phys Chem Chem Phys 2015; 17(28): 18238-18261.

[81] Batista CAS, Larson RG, Kotov NA. Non additivity of nanoparticle interactions. Science 2015; 350 (6257).

[82] Hotze EM, Phenrat T, Lowry GV. Nanoparticle aggregation: Challenges to understanding transport and reactivity in the environment. J Environ Qual 2010; 39(6): 1909-1924.

[83] Ganguly S, Chakraborty S. Sedimentation of nanoparticles in nanoscale colloidal suspensions. Phys Lett Sect A Gen At Solid State Phys 2011; 375(24): 2394-2399.

[84] Kourki H, Famili MHN. Particle sedimentation: Effect of polymer concentration on particle-particle interaction. Powder Technol 2012; 221: 137-143.

[85] Tsimpanogiannis IN, Jamali SH, Economou IG, Vlugt TJH, Moultos OA. On the validity of the Stokes–Einstein relation for various water force fields. Mol Phys 2020;118(9-10).

[86] Koenig G, Ong R., Cortes A, Moreno-Razo J, De Pablo J, Abbot N. Single nanoparticle tracking reveals influence of chemical functionality of nanoparticles on local ordering of liquid crystal and nanoparticle diffusion coefficients. Nano Lett 2009; 9: 2794–2801.

[87] Dutta A, Paul A, Chattopadhyay A. The effect of temperature on the aggregation kinetics of partially bare gold nanoparticles. RSC Adv 2016;6(85):82138-82149.

[88] Jiang W, Ding G, Peng H, Hu H. Modeling of nanoparticles' aggregation and sedimentation in nanofluid. Current Applied Physics 2010;10(3):934-941.

[89] Mehrdel B, Abdul Aziz A, Yoon TL, Lee SC. Effect of chemical interface damping and aggregation size of bare gold nanoparticles in NaCl on the plasmon resonance damping. Opt Mater Express 2017; 7: 955-966.

[90] Giorgi-Coll S, Marín MJ, Sule O, Hutchinson PJ, Carpenter KLH. Aptamer-modified gold nanoparticles for rapid aggregation-based detection of inflammation: an optical assay for interleukin-6. Microchim Acta 2020;187(1).

[91] Fathi F, Rashidi M-, Omidi Y. Ultra-sensitive detection by metal nanoparticles-mediated enhanced SPR biosensors. Talanta 2019; 192:118-127.

[92] Kumar R, Binetti L, Nguyen TH, Alwis LSM, Agrawal A, Sun T, Grattan KTV. Determination of the Aspect-ratio Distribution of Gold Nanorods in a Colloidal Solution using UV-visible absorption spectroscopy. Sci Rep 2019;9(1).

[93] Piella J, Bastús NG, Puntes V. Size-dependent protein-nanoparticle interactions in citrate-stabilized gold nanoparticles: The emergence of the protein corona. Bioconjugate Chem 2017;28(1):88-97.

[94] Ehrenberg MS, Friedman AE, Finkelstein JN, Oberdörster G, McGrath JL. The influence of protein adsorption on nanoparticle association with cultured endothelial cells. Biomaterials 2009;30(4):603-610.

[95] Fröhlich E, Bonstingl G, Höfler A, Meindl C, Leitinger G, Pieber TR, Roblegg E. Comparison of two in vitro systems to assess cellular effects of nanoparticles-containing aerosols. Toxicol., In Vitro 2013; 27(1): 409-41.

[96] Shechtman O. The Coefficient of Variation as an Index of Measurement Reliability. In: Doi S, Williams G. Methods of Clinical Epidemiology. Springer Series on Epidemiology and Public Health. Springer, Berlin. 2013; 39-49.

[97] Kestens V, Coleman VA, De Temmerman P-, Minelli C, Woehlecke H, Roebben G. Improved Metrological Traceability of Particle Size Values Measured with Line-Start Incremental Centrifugal Liquid Sedimentation. Langmuir 2017;33(33):8213-8224.

[98] Goulter RM., Gentle IR., Dykes GA. Issues in determining factors influencing bacterial attachment: a review using the attachment of Escherichia coli to abiotic surfaces as an example. Lett. Appl Microbiol 2009; 4, 1-7.

[99] Behrens SH, Grier DG. The charge of glass and silica surfaces. J Chem Phys 2001;115(14):6716-6721.

[100] Agladze K, Wang X, Romeo T. Spatial periodicity of Eschenchia coli K-12 biofilm microstructure initiates during a reversible, polar attachment phase of development and requires the polysaccharide adhesin PGA. J Bacteriol 2005;187(24):8237-8246.

[101] Tuson HH, Weibel DB. Bacteria-surface interactions. Soft Matter 2013;9(17):4368-4380.

[102] Fazlara A, Ekhtelat M. The disinfectant effects of Benzalkonium Chloride on some important foodborne pathogens. Am Eurasian J Agric Environ Sci 2012;12(1):23-29.

[103] Aodah AH, Bakr AA, Booq RY, Rahman MJ, Alzahrani DA, Alsulami KA, Alshaya HA, Alsuabeyl MS, Alyamani EJ, Tawfik EA. Preparation and evaluation of benzalkonium chloride hand sanitizer as a potential alternative for alcohol-based hand gels. Saudi Pharm J 2021;29(8):807-814

[104] Fang I, Trewyn BG. Chapter three - Application of Mesoporous Silica Nanoparticles in Intracellular Delivery of Molecules and Proteins. Meth Enzymol 2012;508:41-59.

[105] Stam S, Gardel ML. Cutting through the noise: The mechanics of intracellular transport. Dev Cell 2014;30(4):365-366.

[106] Wu P, Hale CM, Chen W, Lee JSH, Tseng Y, Wirtz D. High-throughput ballistic injection nanorheology to measure cell mechanics. Nat Protoc 2012;7(1):155-170.

[107] Parry BR, Surovtsev IV, Cabeen MT, O'Hern CS, Dufresne ER, Jacobs-Wagner C. The bacterial cytoplasm has glass-like properties and is fluidized by metabolic activity. Cell 2014;156(1-2):183-194.

[108] Weber SC, Spakowitz AJ, Theriot JA. Nonthermal ATP-dependent fluctuations contribute to the in vivo motion of chromosomal loci. Proc Natl Acad Sci U S A 2012;109(19):7338-7343.

[109] Tapani E, Taavitsainen M, Lindros K, Vehmas T, Lehtonen E. Toxicity of ethanol in low concentrations: Experimental evaluation in cell culture. Acta Radiol 1996;37(6):923-926.

[110] Castañeda F, Kinne RKH. Cytotoxicity of millimolar concentrations of ethanol on HepG2 human tumor cell line compared to normal rat hepatocytes in vitro. J Cancer Res Clin Oncol 2000;126(9):503-510.

[111] Das SK, Vasudevan DM. Alcohol-induced oxidative stress. Life Sci 2007;81(3):177-187.

[112] Casañas-Sánchez V, Pérez JA, Quinto-Alemany D, Díaz M. Sub-toxic ethanol exposure modulates gene expression and enzyme activity of antioxidant systems to provide neuroprotection in hippocampal HT22 cells. Front Physiol 2016;7.

[113] Kapasi AA, Patel G, Goenka A, Nahar N, Modi N, Bhaskaran M, Reddy K, Franki N, Patel J, Singhal PC. Ethanol promotes T cell apoptosis through the mitochondrial pathway. Immunology 2003 ;108(3): 313-320.

[114] Moon Y, Kwon Y, Yu S. How does ethanol induce apoptotic cell death of SK-N-SH neuroblastoma cells. Neural Regen Res 2013;8(20):1853-1862.

[115] Bortner CD, Cidlowski,JA. Uncoupling cell shrinkage from apoptosis reveals that na+ influx is required for volume loss during programmed cell death. J Biol Chem 2003;278(40): 39176-39184.

[116] Wittmaack K. Excessive Delivery of Nanostructured Matter to Submersed Cells Caused by Rapid Gravitational Settling. ACS Nano 2011;5(5):3766-3778.

[117] Wilson C, Lukowicz R, Merchant S, Valquier-Flynn H, Caballero J, Sandoval J, Okuom M, Huber C, Brooks TD, Wilson E, Clement B, Wentworth CD, Holmes AE. Quantitative and Qualitative Assessment Methods for Biofilm Growth: A Mini-review. Res Rev J Eng Technol. 2017;6(4).

[118] Li W, Zhang S, Yang G. Dynamic organization of intracellular organelle networks. Wiley Interdiscip Rev Syst Biol Med 2020; 13(2):e1505.

[119] Wu W, Jin Y, Bai F, Jin S. Chapter 41 - Pseudomonas aeruginosa. In: Tang Y, Sussman M, Liu D, Poxton I, Schwartzman J. Molecular Medical Microbiology (Second Edition) Boston: Academic Press; 2015: 753-767.

[120] Louten J. Virus Structure and Classification. In: Louten J. Essential Human Virology. Boston: Academic Press; 2016: 19-29.